MULTI-FIDELITY INFORMATION FUSION FOR STRUCTURAL DYNAMICS MODEL CALIBRATION

By

Ghina Nakad Absi

Dissertation
Submitted to the Faculty of the
Graduate School of Vanderbilt University
in partial fulfillment of the requirements
for the degree of

DOCTOR OF PHILOSOPHY

in

Civil Engineering

May 10, 2019

Nashville, Tennessee

Approved:
Sankaran Mahadevan, Ph.D.
Prodyot Basu, Ph.D.
Douglas Adams, Ph.D.
Hiba Baroud, Ph.D.
Mark McDonald, Ph.D.

To my girls...

It’s all for you, it’s all because of you…

To my loving husband, for not letting me give up…

To my wonderful parents… for making me who I am…

Acknowledgments

Words cannot express my gratitude and appreciation for all the help that my advisor and mentor, Prof. Sankaran Mahadevan has given me. The patience, dedication and kindness throughout these years have allowed me to get to where I am today. Many people would have given up, but you never did. You challenged me, listened to me, and guided me in such an exemplary way that I can truly say: not only am I am a better researcher today, but I am also better person because of you. For that and more, I thank you.

To my committee members, Dr. Prodyot Basu, Dr. Douglas Adams, Dr. Hiba Baroud and Dr. Mark McDonald, thank you for all your comments and feedback that allowed this research (and the researcher!) to reach its potential.

This research was partly supported by funds from the Air Force Office of Scientific Research (Project Manager: Dr. Fariba Fahroo) through subcontract to Vextec Corporation (Investigators: Dr. Robert Tryon, Dr. Animesh Dey). Valuable discussions with Dr. Joseph Hoelkampf at the Air Force Research Laboratory (Wright Patterson Air Force Base) are also recognized. In addition, I would like to acknowledge the CEE department for the support though many teacher assistantships during my years at Vanderbilt.

Vanderbilt University is a wonderful place to study. Our research group under Prof. Mahadevan is a big and diverse body, and I owe many of the past and present students so much gratitude for their help and friendship, notably Dr. Bin Liang, Dr. Shankar Sankararaman, Dr. You Ling, Dr. Chenzhao Li, Dr. Josh Mullins, Dr. Chen Liang, Dr. Erin DeCarlo. Thank you for sharing your codes, for helping me debug mine, for your ideas and your discussions.

Along with the research colleagues, I was fortunate to have made durable friendships. Dr. Lesa Brown and Dr. Nikolas Nordendale, I would not be here without your support. The things that you have taught

me both personally and professionally are priceless. Thank you for being who you are…

To my husband, Tarek Absi, thank you. You have allowed this research to thrive. Your support on all levels is invaluable. To my mom and dad, for giving me all the tools to break all barriers, I can't thank you enough. To my brother, for your love and your craziness. And finally, to the three little girls that all this is for: Elsa, Sarah and Celine. I love you.

Table of Contents

List of Tables

List of Figures

Chapter 1

Introduction

1.1 Overview

With the continuous development of faster and more efficient computational capabilities, higher fidelity computer simulations are increasingly being used to try to predict the behavior of engineering systems. Specifically, in dynamics problems, being able to forecast the response of a structure over time is an important need.

In order to obtain a model that is structurally equivalent to an experimental setup, one necessary step is model calibration: quantifying the errors and adjusting the unknown model parameters to minimize the difference between the model output and the experimental data. Errors arise in the numerical methods used to solve the problem, but also in the limitations of the available experimental data.

Uncertainty in simulations arises from multiple sources:

(1) Natural variability (aleatoric uncertainty) which is not reducible, but generally modeled by assigning probability distributions to the variables.

(2) Statistical uncertainty (reducible, epistemic uncertainty). It arises from sparse and/or imprecise data.

(3) Model uncertainty (reducible, epistemic uncertainty), which is due to uncertainty in model parameters, model form error, and solution approximations [1]. The solution approximation errors arise due to reduced-order models, surrogate models, discretization errors, truncation and round off.

Three types of modeling approaches have been pursued in structural dynamics for complicated mechanical systems: (1) finite element models, (2) reduced-order models and (3) surrogate models.

Finite element analysis (FEA) is commonly used in the dynamics modeling of engineering structures with complicated geometry and under complex loading conditions. Construction of the FEA model incorporates many assumptions by the analyst about the system properties and excitation. Two principal qualities are desired in a functional finite element model of structural dynamics [2]: (1) physical significance, i.e., the model should properly represent how the mass, stiffness and damping are distributed, and (2) correctness, i.e., the observations from dynamics experiments are accurately predicted by the model. High-fidelity dynamic finite element analysis of complex mechanical systems is quite expensive, and considerable research has been done to construct cheaper and simpler surrogate models, equivalent static models, or reduced-order models, especially when many runs of the dynamics model are necessary. However, the errors and uncertainties in calibration and prediction increase with the reduction in model fidelity. Computationally efficient models have to be cheap enough to allow multiple repetitions of the simulations, but also retain precious information available from rigorous but more expensive models.

In order to improve the performance of simulation models, model calibration, commonly known as model updating in dynamics literature, has been extensively investigated. Bayesian calibration is able to combine both prior (subjective) information and experimental data and also quantify the epistemic uncertainty in the calibration result. Bayesian model calibration in practice often uses Markov Chain Monte Carlo (MCMC) sampling which requires thousands of samples. The expense is further increased if the number of parameters is high, or the model output is far from the experimental data; therefore, the original simulation model may be replaced by an inexpensive surrogate model to reduce the computational cost. However, building a surrogate model also requires training points, which are generated by running the original model at a certain number of input conditions. Obviously, the larger the number of training points, the more accurate is the surrogate model. If the original high-fidelity physics model is expensive, this may limit the number of training points. On the other hand, if a lower

fidelity model is available, this may help to generate a large number of training points, but the accuracy of the resulting surrogate model would be questionable. Such a scenario motivates the need for a methodology that can efficiently combine physics models of lower and higher fidelity to balance accuracy vs. computational effort in the Bayesian calibration of system model parameters.

The aim of this dissertation is to develop a novel optimized approach for fusing information from models of different levels of fidelity in the Bayesian calibration of the model parameters. In order to balance computational effort and accuracy, the proposed method uses a corrected low-fidelity surrogate model. First, it takes advantage of the information available in high-fidelity simulation to improve the low-fidelity surrogate model, and then uses the improved low-fidelity surrogate model for calibration. Use of the low-fidelity surrogate model facilitates computational efficiency. Furthermore, the improvement with high-fidelity results before calibration with experimental data provides stronger, physics-informed priors for the calibration quantities. This is particularly useful when limited experimental data are available, and a reliable, nevertheless fast model is needed for calibration. The multi-fidelity calibration method is also extended to calibration of input-dependent system parameters, where the hyper-parameters of the functional relationship between the input and the parameters are updated. This extension also takes into consideration the effect of the input on the uncertainty in the experimental data. Finally, the multi-fidelity approach is optimized to maximize the information gain in correcting the low-fidelity model (simulation optimization) as well as in the experimental sensor configuration (i.e., number and locations of the sensors).

1.2 Research Objectives

The research objectives are summarized as follows:

(1) Multi-Fidelity Information Fusion Approach for Dynamics Model Calibration

(2) Input-Dependence Effects in Multi-Fidelity Dynamics Model Calibration

(3) Multi-Fidelity Simulation Optimization

(4) Multi-Fidelity Sensor Optimization

The first objective focuses on the information fusion method, in which a corrected low-fidelity surrogate model is used for the calibration of system parameters. It takes advantage of the information available in high-fidelity simulation to first improve the low-fidelity surrogate model, and then uses the improved low-fidelity surrogate model for calibration. As a result, information is gained from both low and high-fidelity simulations.

The novel two-step calibration approach is then extended in the second objective to the Bayesian calibration of input-dependent system parameters in multi-physics problems. A parametric relationship between the input and the system parameters is assumed, and the parameters of this relationship are calibrated along with other calibration quantities using the experimental data. The effects of multiple inputs on the parameters as well as on the physics of the problem (for example, thermal loading effect on modal analysis) are investigated.

In the above two objectives, inexpensive surrogate models need to be developed for the system to make the Bayesian calibration affordable. Therefore, in the third objective, the emphasis is on optimal selection of high-fidelity simulations to develop an accurate surrogate model. A subset of high-fidelity simulation data is first used to correct the low fidelity surrogate model. Synthetic high-fidelity data are then generated within an optimization framework to identify those high-fidelity runs that maximize the information gain in the correction step. This novel inverse problem approach also yields faster convergence in the calibration parameters.

The fourth and last objective focuses on optimizing the sensor layout (number and locations of sensors) to maximize the information gain from the calibration data.

1.3 Dissertation Organization

This dissertation is organized to address the objectives listed in Section 1.2 . Chapter 2 is an overview of background information providing detailed fundamentals of Bayesian model calibration, surrogate models, uncertainty quantification, and methodology evaluation. Chapter 3 proposes a multi-fidelity approach to fuse the information from physics models of different fidelity for the calibration of system parameters. Chapter 4 extends the multi-fidelity calibration approach to problems with input-dependent system parameters and errors. Chapter 5 focuses on minimizing the simulation effort by selecting those expensive high-fidelity simulations that maximize the information gain in the multi-fidelity model development step. Chapter 6 optimizes the number and locations of the sensors for experimental data collection such that the information gain in the calibration step is maximized. 0 concludes the dissertation and offers ideas for future work

Chapter 2

Background

This chapter provides some of the fundamental background information on uncertainty quantification (UQ) in multi-fidelity calibration. The approach developed in this dissertation for combining models of multiple fidelity for parameter calibration is quite general and is applicable to a wide variety of physics models. However, this research focuses on structural dynamics problems to develop this approach, in particular the calibration of damping parameters.

2.1 Calibration of Damping

Consider the structural dynamics model:

$$[\boldsymbol{M}]\{\ddot{x}(t)\}+[\boldsymbol{C}]\{\dot{x}(t)\}+[\boldsymbol{K}]\{x(t)\}=\{f(t)\} \tag{1}$$

where [**M**] is the mass matrix, [**K**] is the stiffness matrix and [**C**] is the damping matrix. The mass matrix could be calculated based on measurements of smaller components of the structure or based on information about material density and component and system geometry. Similarly, the stiffness matrix could be calculated based on known or measured mechanical properties (e.g., Young's modulus) and the geometry of the components and system. However, damping cannot be directly calculated or measured; it must be inferred from the dynamic response of the structure under some excitation.

By definition, damping is the dissipation of energy from a vibrating structure and is dependent on the active physical mechanisms in the structure. These mechanisms are very complicated, and not precisely understood. The types of damping present depend on which mechanism dominates in a given structural

configuration [3]. For example, structural (or hysteretic) damping is a property that is intrinsic to the material. Coulomb damping (also known as frictional damping) is used to represent dry friction in sliding surfaces, such as structure joints. Non-viscous damping models are such that the damping forces depend on the structural response history. In multiple degree-of-freedom systems, the most popular approach is to assume viscous damping, which is a special case of the general linear damping model that has no memory.

Often, viscous damping has been assumed and derived from the shape of the frequency response curve in several ways [4]. One way is by using the half-power bandwidth method (Fig. 1), in which the viscous damping ratio (ζ) is determined from the frequencies for which the power input is half the input at resonance using $\frac{\omega_2 - \omega_1}{\omega_0} = 2\zeta = \frac{1}{Q}$, where ω_0 is the frequency at the maximum amplitude $x_{\max}$, ω_1 and ω_2 are the frequencies at $\frac{x_{\max}}{\sqrt{2}}$, and Q is the amplification factor.

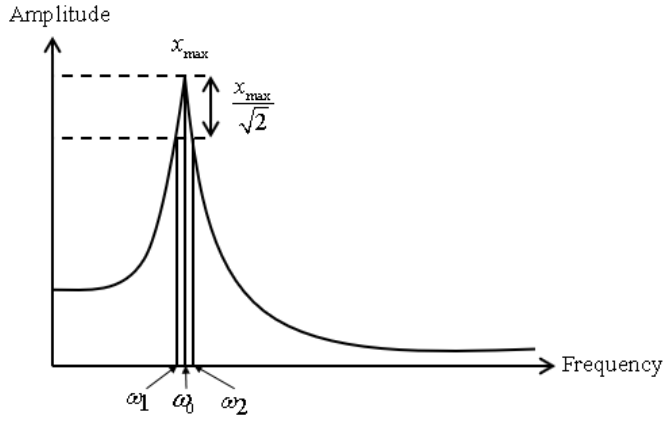

Fig. 1: Half-power bandwidth method

Another method is by conducting experiments at resonance to measure the phase relationship between

the input force and the resulting displacements, without having to construct the frequency response curve. The applied load is exactly balanced by the damping force when resonance is established by adjusting the input frequency until the response is 90^o out of phase with the load. For one given loading cycle, the damping force displacement diagram can be plotted (Fig. 2Fig. 2), and the damping coefficient determined directly as the ratio of the maximum damping force ($f_{D,\max}$) to the maximum velocity ($\dot{v}_{\max}$). Linear damping results in an elliptic shape (dashed line), and the damping coefficient (ζ) is directly derived as shown in Fig. 2. If the damping is nonlinear (solid line), an ellipse with radiuses p_0 and ρ having the same area as the original shape is constructed, and an equivalent viscous damping is then defined as that causing the same energy loss per cycle as in the observed force-displacement diagram using $\zeta = \frac{f_{D,\max}}{\dot{v}_{\max}} = \frac{p_0}{\omega\rho}$.

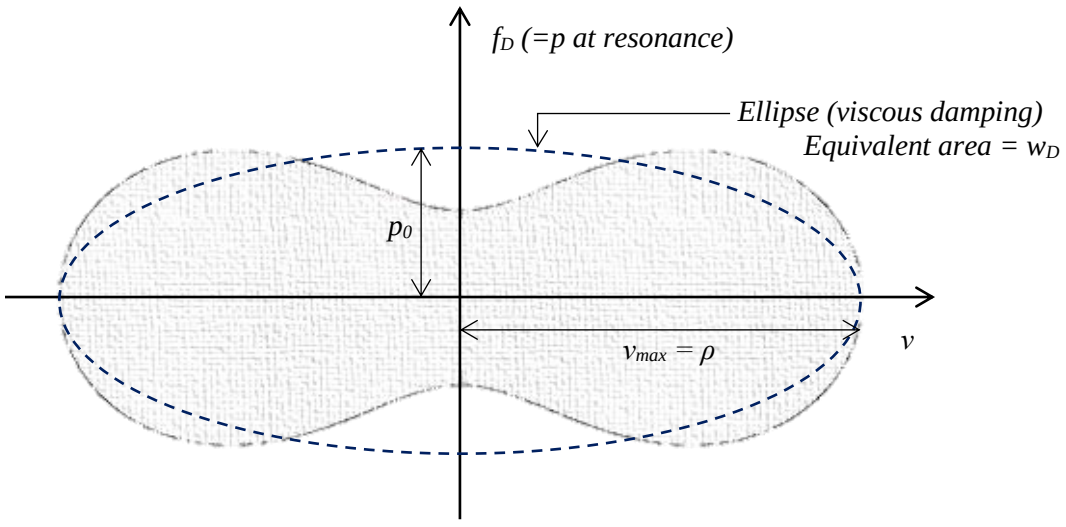

Fig. 2: Actual and equivalent damping energy per cycle

2.2 Bayesian Calibration

System parameters that cannot be calculated or observed directly are usually inferred by observing the output from a certain experimental setup, at a specific set of inputs. Three approaches are commonly available for calibration of model parameters with input-output data: least squares, maximum likelihood, and Bayesian calibration. Bayesian calibration is able to combine both prior (subjective) information and experimental data and is able to quantify the epistemic uncertainty in the calibration result. Kennedy and O'Hagan [5] have developed a Bayesian calibration framework (commonly known as KOH framework), which includes multiple sources of uncertainty, specifically a discrepancy function between the model and the experimental data. Including appropriate model discrepancy functions has been shown to improve calibration of model parameters [6]. Simoen et al. [7] argue that calibration is extremely sensitive to small errors, and that an inadequate quantification of uncertainty may weaken robust inverse methodologies. Further, Goulet [8] shows that when using Bayesian inference, the assumption of independent uncertainties may bias the posterior density function. Bayesian calibration [5] [9] is one approach to infer unmeasured quantities by applying Bayes' theorem, which states that the posterior probability density of unknown quantities are proportional to the product of the likelihood function and the prior density, as shown in Eq. (2). The prior and posterior densities represent the analyst's epistemic uncertainty about the calibration parameter; increased availability of data in general leads to reduction in the variance of the posterior density, thus indicating increasing knowledge or certainty about the calibration parameter.

Bayesian calibration of model parameters may be expressed as

$$f_{\boldsymbol{\Theta}}(\boldsymbol{\Theta} \mid \boldsymbol{Y}_{obs}) \propto f_{\boldsymbol{\Theta}}(\boldsymbol{\Theta}).L(\boldsymbol{\Theta}) \tag{2}$$

where $f_{\Theta}(\boldsymbol{\Theta} \mid \boldsymbol{Y}_{obs})$ is the posterior distribution of the parameter $\boldsymbol{\Theta}$ after calibration using the data $\mathbf{Y}_{\mathbf{obs}}$, $f_{\Theta}(\boldsymbol{\Theta})$ is the prior distribution of $\boldsymbol{\Theta}$ (assumed by the analyst based on available information), and $L(\boldsymbol{\Theta})$ is the likelihood function (i.e., probability of observing the data $\mathbf{Y}_{\mathbf{obs}}$, given a value of the calibration parameter $\boldsymbol{\Theta}$). Samples of the posterior can be constructed using a Markov Chain Monte Carlo (MCMC) algorithm. Several algorithms are available for MCMC sampling: Metropolis [10], Metropolis-Hastings [11], Gibbs sampling [12], slice sampling [13], etc. Slice sampling is used in this dissertation to evaluate Eq. (2). It is based on the observation that to sample a random variable, one can sample uniformly from the area under the PDF. The simplest implementation (for a uni-variate distribution without the need to reject any points) consists of first sampling a random value *y* between zero and the maximum PDF value $y_{\max}$, and then sampling $\boldsymbol{\Theta}$ from the slice under the PDF, as shown in Fig. 3.

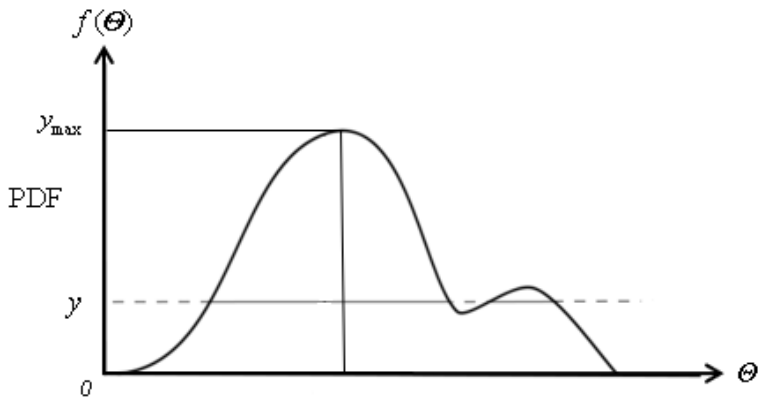

Fig. 3: Simple implementation of slice sampling

Slice sampling requires many simulations of the model being used for calibration. High-fidelity physics models are very expensive to run in calibration; thus, we often replace them with inexpensive

surrogate models.

2.3 Surrogate Model – Polynomial Chaos Expansion

Many surrogate modeling techniques have been developed in the literature, such as linear/quadratic polynomial-based response surfaces [14], artificial neural networks [15], support vector machines (SVM) [16], polynomial chaos expansion (PCE) [17], and Gaussian process (GP) interpolation (or Kriging) [18]. In this dissertation, PCE is used for the sake of illustration to replace the original FEA model for inexpensive sampling during the calibration process. PCE is a regression-based surrogate model that represents the output of a model with a series expansion in terms of standard random variables (SRVs). Consider a model $\boldsymbol{y} = f(\boldsymbol{x})$ where $\boldsymbol{x} = \{x_1, x_2, ..., x_k\}^T$ is a vector of input random variables. We construct a PCE model to replace $f(\boldsymbol{x})$ using h multi-dimensional Hermite polynomials as basis functions:

$$\boldsymbol{y} = \sum_{j=0}^{h} \theta_j \varphi_j(\boldsymbol{\xi}) = \boldsymbol{\theta}^T(\boldsymbol{\xi}) + \boldsymbol{\varepsilon_{surr}} \tag{3}$$

where $\boldsymbol{\xi}$ is a vector of independent standard normal random variables which correspond to the original input $\boldsymbol{x}$ [19]. $\boldsymbol{\varphi}(.) = \{\phi_0(.), \phi_1(.), \ldots, \phi_h(.)\}^T$ are the Hermite polynomial basis functions, and $\boldsymbol{\theta} = \{\theta_0, \theta_1, \ldots, \theta_h\}^T$ are the corresponding coefficients that can be estimated by the least squares method. A collocation point method can be used to efficiently select training points where the original model is evaluated [20]. Suppose that t training points (ξ_i, y_i), i =1, 2, ..., t are available. Under the Gauss-Markov assumption [21], the surrogate model error $\boldsymbol{\varepsilon}_{surr}$ asymptotically follows a normal distribution with zero mean and variance given by

$$Var[\boldsymbol{\varepsilon_{surr}}] \approx s^2 + s^2 \phi(\boldsymbol{\xi})^T (\boldsymbol{\Phi}^T \boldsymbol{\Phi})^{-1} \phi(\boldsymbol{\xi}) \tag{4}$$

where

$$\boldsymbol{\Phi} = \{\phi(\xi_1), \phi(\xi_2), ..., \phi(\xi_t)\}^T \quad \text{and} \quad s^2 = \frac{1}{t-h}\sum_{i=1}^{t}[y_i - \boldsymbol{\theta}^T\phi(\xi_i)]^2$$

In all calibration calculations in this dissertation, the original finite element models are replaced with PCEs; the surrogate model error is calculated and added to the output by randomly sampling a value from its distribution.

2.4 Error Inclusion in Calibration

The experimental observation $\mathbf{Y_{obs}}$ is expressed in terms of the input $\boldsymbol{X}$, parameters $\boldsymbol{\theta}$, the errors and the model output as follows:

$$\mathbf{Y_{obs}} + \boldsymbol{\varepsilon_{obs}} = G\left(\boldsymbol{X} + \boldsymbol{\varepsilon_{in}}, \boldsymbol{\theta}\right) + \boldsymbol{\varepsilon_{surr}} + \boldsymbol{\varepsilon_d} \tag{5}$$

where $\boldsymbol{\varepsilon_{in}}$: vector of input measurement errors, one for each input measured

$\boldsymbol{\varepsilon_{obs}}$: vector of measurement errors for the multiple outputs

$\boldsymbol{\varepsilon_d}$: vector of model discrepancy terms (discrepancy between prediction and observation), one for each output

$\boldsymbol{\varepsilon_{surr}}$: vector of surrogate model errors, one for each output

The system parameters $\boldsymbol{\theta}$ are calibrated using Bayes' theorem as:

$$\pi(\boldsymbol{\theta}, \boldsymbol{\sigma_{obs}}, \boldsymbol{\varepsilon_d} \mid \mathbf{y_D}) = \frac{L(\boldsymbol{\theta}, \boldsymbol{\sigma_{obs}}, \boldsymbol{\varepsilon_d})\ \pi(\boldsymbol{\theta}, \boldsymbol{\sigma_{obs}}, \boldsymbol{\varepsilon_d})}{\int L(\boldsymbol{\theta}, \boldsymbol{\sigma_{obs}}, \boldsymbol{\varepsilon_d})\ \pi(\boldsymbol{\theta}, \boldsymbol{\sigma_{obs}}, \boldsymbol{\varepsilon_d}) d\boldsymbol{\theta}\ d\boldsymbol{\sigma_{obs}}\ d\boldsymbol{\varepsilon_d}} \tag{6}$$

where

$$L(\boldsymbol{\theta},\boldsymbol{\sigma}_{obs},\boldsymbol{\varepsilon}_d) \propto \prod_{i=1}^{m} \pi\left(\mathbf{Y}_{\mathbf{obs}i} = \mathbf{y}_{\mathbf{D}i} \mid \boldsymbol{x}_{Di},\boldsymbol{\theta},\boldsymbol{\sigma}_{obs},\boldsymbol{\varepsilon}_d\right) \tag{7}$$

π(*) denotes the joint probability density function (PDF) of the variables, $\pi(\boldsymbol{\theta},\boldsymbol{\sigma}_{obs},\boldsymbol{\varepsilon}_d)$ is the prior joint PDF of $\boldsymbol{\theta}$, $\boldsymbol{\sigma}_{obs}$ and $\boldsymbol{\varepsilon}_d$; $\pi(\boldsymbol{\theta},\boldsymbol{\sigma}_{obs},\boldsymbol{\varepsilon}_d \mid \mathbf{y}_\mathbf{D})$ is the joint posterior PDF of $\boldsymbol{\theta}$, $\boldsymbol{\sigma}_{obs}$ and $\boldsymbol{\varepsilon}_d$ given $\mathbf{y}_\mathbf{D}$; and $L(\boldsymbol{\theta},\boldsymbol{\sigma}_{obs},\boldsymbol{\varepsilon}_d)$ is the joint likelihood function of $\boldsymbol{\theta}$, $\boldsymbol{\sigma}_{obs}$ and $\boldsymbol{\varepsilon}_d$. $\mathbf{y}_{\mathbf{D}i}$ is the vector of the *n* outputs $\mathbf{Y}_{\mathbf{obs}i}$ for each individual input setting $\boldsymbol{x}_{Di}$, and *i* = 1 to *m*, where *m* is the number of settings for which the outputs are observed. The likelihood function is based on the joint PDF of the observations $\mathbf{y}_{\mathbf{D}i}$, conditioned on $\boldsymbol{\theta}$, $\boldsymbol{\sigma}_{obs}$ and $\boldsymbol{\varepsilon}_d$. This consideration of the likelihood function allows the inclusion of correlated model outputs, correlated model errors, and correlated sensor observations. The formulation in Eq. (6) is general (i.e., it handles correlated as well as independent parameters). If the observed outputs are independent, the likelihood in Eq. (7) is the product of the likelihoods for the individual outputs as well as samples y_{Dij} (*i* = 1 to *m*, *j* = 1 to *n*), as:

$$L(\boldsymbol{\theta},\boldsymbol{\sigma}_{obs},\boldsymbol{\varepsilon}_d) \propto \prod_{i=1}^{m}\prod_{j=1}^{n} \pi\left(y_{Dij} \mid \boldsymbol{x}_{Di},\boldsymbol{\theta},\sigma_{obsj},\varepsilon_{dj}\right) \tag{8}$$

Many sources of modeling errors contribute to the model discrepancy term $\boldsymbol{\varepsilon}_d$ (numerical as well as model form) [22] [23]. In this research, we do not quantify the individual model error sources, but only the overall discrepancy term because the focus is on the calibration of system parameters.

In order to get accurate calibration results, both modeling and experimental errors need to be included in the calibration [32]. Research has been done on identifying the characteristics of the prediction error, using available experimental observations. Christodoulou and Papadimitriou [24] and Zhang et al. [25] include variance parameters of uncorrelated zero-mean Gaussian models of experimental measurement

errors, and correlation parameters like correlation lengths [26, 27]. In the numerical example in this dissertation, the scarcity of experimental data available does not allow further characterization of these errors.

When quantifying the model discrepancy term, capturing missing physics and assuming priors for the discrepancy parameters are two issues that need to be carefully studied. Brynjarsdottir and O'Hagan [6] showed that satisfying calibration results can only be reached if the discrepancy term captures the missing physics in the model; thus, there is need for a rigorous discrepancy model. This requires including additional parameters in the discrepancy term that need to be calibrated. This may lead to: (a) slowing down the convergence (in the best case scenario), (b) increasing the uncertainty of calibration results, or (c) parameter non-identifiability [27]. Different prior assumptions for the model discrepancy term $\boldsymbol{\varepsilon_d}$ have been used in the literature, including constant, random walk [28], physics-based deterministic function [29], Gaussian random variable [30], uncorrelated random vector [31], and Gaussian random process [9]. It is calibrated along with model parameters using experimental data, following Eq.(5). Typically, well-designed high-fidelity models present a smaller $\boldsymbol{\varepsilon_d}$ than lower fidelity models. However, high-fidelity models may be prohibitively expensive to run in some problems.

2.5 Kullback–Leibler divergence

A significant posterior distribution change compared to a prior distribution in a calibration exercise implies the incorporation of new information into the calibration process. The bigger the change, the more is the gain in the information. In order to optimize the high-fidelity run inputs to include the most relevant information into the low-fidelity surrogate model, we pick the high-fidelity locations that yield the largest posterior changes in calibration. The changes can be reflected in a shift of the posteriors (bias

change), a reduction in uncertainty, or both. In order to account for both the bias and uncertainty changes, we use the Kullback-Leibler (KL) [32] divergence calculation.

KL divergence is a non-symmetric measure of the relative entropy between two probability distributions. It has been used as a measure of information lost when a new distribution is trying to approximate an old one or as a measure of information gain when the gain is reflected by a large divergence of the posterior distribution compared to the prior in calibration. The latter measure is of interest in the context of calibration.

Assume $p(x)$ and $q(x)$ are two probability distributions of a random variable x. The KL divergence KLD of $q(x)$ compared to $p(x)$ is defined as:

$$KLD(p(x)||q(x)) = \int_{-\infty}^{\infty} p(x) \ln \frac{p(x)}{q(x)} dx \tag{9}$$

Note that KL divergence is not a distance measure: $KLD(p(x)||q(x)) \neq KLD(q(x)||p(x))$. In addition, $KLD(p(x)||q(x)) \geq 0$ and $KLD(p(x)||q(x)) = 0$ if and only if $p(x) = q(x)$ for all x.

In this dissertation, we compute the KL divergence for the joint posterior distribution compared to the joint prior distribution within the optimization algorithm.

2.6 Methodology Evaluation

Many comparison techniques exist to assess whether the available experimental data (independent from the data used in the calibration process) supports one model over the other. These range from graphical visual comparison, to different types of hypothesis testing. Berger and Pericchi [33] argue that Bayesian methods of model selection and hypothesis testing are needed because measures based on

frequentist computations are vague and can only compare two models at a time. Another noteworthy difference between Bayesian and classical hypothesis testing is that the former picks the model that is most likely to be accepted, whereas the latter rejects the model that does not have enough evidence to support it [34].

Consider two models (M_1 and M_2), with outputs $\mathbf{Y_1}$ and $\mathbf{Y_2}$, and prior probabilities of acceptance $P(\mathbf{Y_1})$ and $P(\mathbf{Y_2})$. The output PDFs are denoted $f_X^1(\boldsymbol{X},\boldsymbol{\Theta})$ and $f_X^2(\boldsymbol{X},\boldsymbol{\Theta})$ respectively, where $\boldsymbol{\Theta}$ includes all the calibration quantities in Eq. (5) ($\boldsymbol{\theta}$, $\boldsymbol{\varepsilon_{obs}}$ and $\boldsymbol{\varepsilon_d}$). The relative posterior probabilities based on observed data can be computed using Bayes' rule [35]:

$$\frac{P(\mathbf{Y_1} \mid \mathbf{Y_{obs}})}{P(\mathbf{Y}_2 \mid \mathbf{Y_{obs}})} = \frac{P(\mathbf{Y_{obs}} \mid \mathbf{Y_1})}{P(\mathbf{Y_{obs}} \mid \mathbf{Y}_2)} \frac{P(\mathbf{Y_1})}{P(\mathbf{Y}_2)} \tag{10}$$

In Eq.(10), the likelihood ratio $B = \frac{P(\mathbf{Y_{obs}} \mid \mathbf{Y_1})}{P(\mathbf{Y_{obs}} \mid \mathbf{Y_2})}$ is referred to as "Bayes factor" [36], and is used as the metric to evaluate the data support to model M_1 relative to model M_2.

If the Bayes factor B is greater than 1.0, then it can be inferred that the model M_1 has greater support from the data. The higher the value of B, the greater the confidence in choosing M_1 over M_2. If the prior probabilities of the two model predictions P($\mathbf{Y_1}$) and P($\mathbf{Y_2}$) are equal, then in fact we can derive [37] $P(\mathbf{Y_1} \mid \mathbf{Y_{obs}}) = \frac{B}{B+1}$ and $P(\mathbf{Y_2} \mid \mathbf{Y_{obs}}) = \frac{1}{B+1}$. This gives a quantitative measure of the confidence in selecting model M_1 vs. M_2.

In order to implement the above Bayesian hypothesis testing, the likelihood functions $P(\mathbf{Y_{obs}} \mid \mathbf{Y_1})$) and $P(\mathbf{Y_{obs}} \mid \mathbf{Y_2})$ need to be calculated. This can be done in two steps. Assuming n data points are

available, we first calculate $P(\mathbf{Y_{obs}} \mid \mathbf{Y_1}, \boldsymbol{\Theta})$

$$P(\mathbf{Y_{obs}} \mid \mathbf{Y_1}, \boldsymbol{\Theta}) \propto L(\mathbf{Y_1}, \boldsymbol{\Theta}) = \prod_{i=1}^{n} f_{\boldsymbol{X}}^{1}(\boldsymbol{x} = \boldsymbol{x}_i \mid \boldsymbol{\Theta}) \tag{11}$$

then integrate it over θ, to obtain

$$L(\mathbf{Y_1}) \propto P(\mathbf{Y_{obs}} \mid \mathbf{Y_1}) = \int P(\mathbf{Y_{obs}} \mid \mathbf{Y_1}, \boldsymbol{\Theta}) f_{\boldsymbol{\Theta}}(\boldsymbol{\Theta}) d\boldsymbol{\Theta} \tag{12}$$

where $f_{\boldsymbol{\Theta}}(\boldsymbol{\Theta})$ denotes the posterior PDF of $\boldsymbol{\Theta}$ after calibration.

The same equations can be written for M_2 and $\mathbf{Y_2}$, and $P(\mathbf{Y_{obs}} \mid \mathbf{Y}_2, \boldsymbol{\Theta})$ can be calculated.

In order to use the Bayes factor to compare different calibrated models, the data used for calculating Bayes factor needs to be independent from the calibration data. This can be achieved in two scenarios: (a) either by using data recorded at different locations than the ones used in calibration, or (b) by using data at the same location as the calibration data but recorded from an independently repeated experimental run. Knowing that the model form and observation errors are location-dependent, if the independent data is at the same location as the calibration data, these calibrated errors may be used in the calculation of the likelihoods in Eq.(12). If the comparison data is available at a different location, these errors should not be included in the likelihood formulation.

2.7 Summary

This chapter reviewed the fundamentals of methods for calibration of dynamics model parameters under uncertainty (Bayesian calibration, damping calibration, surrogate modeling, error quantification and methodology evaluation). Further developments of these methods are described in later chapters of this dissertation, namely the likelihood calculation for input dependent parameters. The proposed

methods in this work use these fundamentals to fuse information from models of different fidelity in inverse problems as shown in Chapter 2Chapter 3, and extended to input-dependent parameters in multi-physics problems in Chapter 4 . The optimization of simulation and data collection efforts in implementing these techniques is developed in Chapters 5 and 6 , focusing on minimizing the number of runs of expensive high fidelity models and finding the best sensor configuration that maximizes the information gain in the calibration parameters.

Chapter 3

Multi-Fidelity Approach to Dynamics Model Calibration

3.1 Introduction

In this chapter, we propose a novel calibration method to fuse information coming from physics models of different fidelity in the calibration of system parameters. A low-fidelity surrogate model is corrected with high-fidelity simulation to construct stronger ***physics-informed priors*** in the calibration with experimental data. The application problem is a curved panel near a hypersonic aircraft engine subjected to high acoustic loading with unknown damping parameters.

Different types of models may be available for the estimation of unmeasured system properties, with different levels of physics fidelity, mesh resolution and boundary condition assumptions. High-fidelity dynamic simulation allows the prediction of performance not only under normal operating conditions but also during startup, shutdown and abnormal conditions, especially when behavior is highly non-linear, and linear low-fidelity models are inaccurate [38]. In hypersonic aircraft simulations for example, Candler et al. [39] [40], Higgins and Schmidt [41], and many others have investigated high-fidelity analyses. Considerable effort has also been reported in developing reduced-order models that are cheaper and faster to run [42] [43] [44]. McEwan et al [45] [46] proposed the Implicit Condensation (IC) method that included the nonlinear terms of the equation of motion, but restricted the nonlinear function to cubic stiffness terms. The IC method can only predict the displacements covered by the bending modes. Other methods explicitly include additional equations to calculate the membrane displacements in the ROM, such as those by Rizzi et al. [47] [48] and Mignolet et al. [49] [50]. These high fidelity simulations, as

well as the reduced-order models, are useful only when they are good representations of the actual structure and the underlying physics that cause the observed behaviors are taken into account [51].

Several studies have replaced the expensive computational model with surrogate models such as Polynomial Chaos Expansion (PCE), Gaussian process models, etc. Dynamic finite element models are particularly expensive to run, and Hemez and al. [52] also used a polynomial surrogate to reduce the computational cost in calibrating the parameters of a transient dynamics problem. Methods for multi-fidelity surrogate modeling have also been proposed, when models of different complexities are available. Haftka [53] and Hutchison et al. [54] calculated a high-to-low fidelity ratio, and applied it as a scaling factor to the low fidelity data to refine the low fidelity surrogate model. Kennedy and O'Hagan [55] developed an autoregressive approach to combine surrogate models of different fidelities. Leary et al. [56] used the difference between the high-fidelity and low-fidelity data at certain locations to train artificial neural networks and kriging interpolation. Forrester et al. [57] considered partially converged simulations from a high-fidelity model as low-fidelity data.

The goal of model calibration is to find the parameter values that minimize the difference between model prediction and experimental observation (using least squares, for example). Direct model updating methods have been proposed by computing closed-form solutions for the global stiffness and mass matrices using the structural equations of motion [58] [59]. The generated matrices are faithful to modal analyses, but do not always maintain structural connectivity, and may not retain physical significance. Other iterative methods study the changes in model parameterization to evaluate the type and the location of the erroneous parameters, and vary these parameters in an effort to minimize the difference between the experimental data and the FE model predictions [60]. Datta et al. [61] used complex mode data to update FEA models with validated models and synthetic data; however performing complex mode

identification tests is difficult. Other studies propose updating different parameters separately, in a two-step method. Arora et al. [62] update mass and stiffness matrices in the first step, and then use the updated results in the second step to update the damping matrix. Yuan and Yu [63] claim that the difference in scale between the parameters (elastic moduli and hysteresis damping in this case) degrades the results if the updating is done in one step. These methods are also only valid if the parameters are not correlated.

For Bayesian model updating of dynamics problems, Beck and Katafygiotis [64] developed a Bayesian probabilistic system identification framework, in which the structural model and the probability models used to quantify the uncertainties are updated using experimental observations, and the output is a combination of the optimum solutions of the individual probability models. Yuen and Katafygiotis [65] then presented a Bayesian time-domain methodology for model calibration of linear MDOF systems that updates the modal parameters using one set of observed data, without the need to calculate multiple optima. It is based on an appropriately selected multi-variate Gaussian distribution for modal parameters. On the other hand, Yuen and Katafygiotis [66] and Au [67] make use of models in the frequency domain, and Au [67] calibrates modal parameters using well separated modes and a more general case of multiple closely spaced modes [68]. These approaches focus on the updating of modal parameters, and the development of analytical solutions for the Bayesian updating, especially the likelihood function. The class of problems of interest in this dissertation is different, i.e., problems with complicated excitation, and non-linear structural behavior (e.g., excitation-dependent damping), that require finite element-based numerical solutions. Furthermore, analytical solutions for Bayesian updating are not available, and numerical approaches such as Markov Chain Monte Carlo sampling need to be pursued instead.

In a general situation where conjugate distributions cannot be assumed, or analytical solutions are not

available, Bayesian model calibration uses Markov Chain Monte Carlo (MCMC) sampling which requires thousands of samples. The expense is further increased if the number of parameters is high, or the model output is far from the experimental data; therefore, the original simulation model may be replaced by an inexpensive surrogate model to reduce the computational cost. However, building a surrogate model also requires training points, which are generated by running the original model at a certain number of input conditions. Since lower fidelity models are usually much cheaper to run than higher fidelity ones, more training points can be generated with low-fidelity simulations, and thus the low fidelity surrogate model errors are smaller than higher fidelity ones. However, given that the surrogate model is trained with low-fidelity physics simulations, the accuracy gain is not clear. On the other hand, the model discrepancy term clearly decreases with higher fidelity models. To illustrate this, let N_1 and N_2 denote the number of simulations available for each original model $G_1(\boldsymbol{X}, \boldsymbol{\theta})$ and $G_2(\boldsymbol{X}, \boldsymbol{\theta})$, uniformly distributed over the problem domain ($G_1(\boldsymbol{X}, \boldsymbol{\theta})$ and $G_2(\boldsymbol{X}, \boldsymbol{\theta})$ refer to lower and higher fidelity models respectively). These realizations are used as training points to build the corresponding surrogate models. Because of time and budget constraints, we assume that the higher the fidelity of the model, the lower the number of simulations available, i.e.: $N_2 < N_1$. This results in a surrogate model error for $G_2(\boldsymbol{X}, \boldsymbol{\theta})$ larger than that for $G_1(\boldsymbol{X}, \boldsymbol{\theta})$. However, since $G_2(\boldsymbol{X}, \boldsymbol{\theta})$ is of a higher fidelity than $G_1(\boldsymbol{X}, \boldsymbol{\theta})$, the model discrepancy term in $G_1(\boldsymbol{X}, \boldsymbol{\theta})$ is larger than that for $G_2(\boldsymbol{X}, \boldsymbol{\theta})$. Fig. 4 shows a notional diagram of how the surrogate model error and the model discrepancy term might vary with the fidelity of the model.

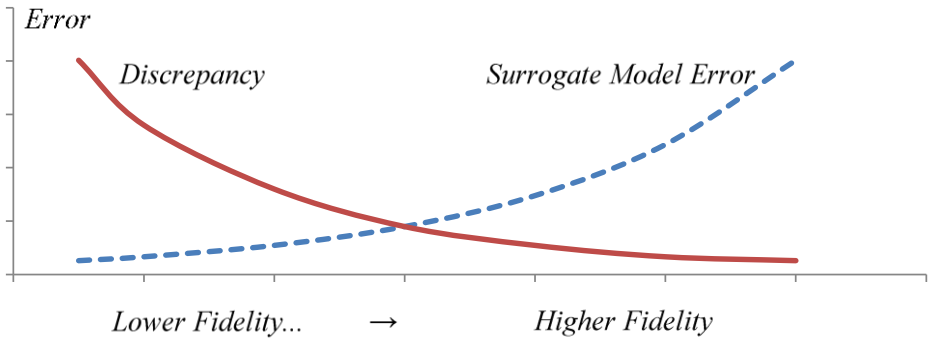

Fig. 4: Variation of surrogate model error and discrepancy with model fidelity

Such a scenario motivates the need for a methodology that can efficiently combine models of lower and higher fidelity to balance accuracy vs. computational effort in the Bayesian calibration of system model parameters.

The aim of this study is to develop a novel approach of fusing information from models of different levels of fidelity in the Bayesian calibration of the model parameters. The proposed approach uses a low-fidelity surrogate model corrected with high-fidelity simulations for calibration of system parameters. The corrected low-fidelity surrogate model is inexpensive to use in calibration, and is more accurate than the uncorrected surrogate since it fuses information from both low and high-fidelity models. The methodology is illustrated for a curved panel located in the vicinity of a hypersonic aircraft engine, subjected to acoustic loading. Two models (a frequency response analysis and a full time history analysis) are combined to calibrate the damping characteristics of the panel.

3.2 Multi-Fidelity Calibration Method

In this section, the concept of calibration is extended from a simple calibration using experimental

data with a single model, to a two-step approach, by combining models of different fidelities. Assume that we have the same two models $G_1(\boldsymbol{X},\boldsymbol{\theta})$ and $G_2(\boldsymbol{X},\boldsymbol{\theta})$. Even $G_1(\boldsymbol{X},\boldsymbol{\theta})$ is expensive to use in Bayesian calibration, which requires thousands of MCMC samples, therefore the low fidelity model is replaced with a fast running surrogate model $S_1(\boldsymbol{X},\boldsymbol{\theta})$ in the proposed methodology. In order to build this surrogate model, the model $G_1(\boldsymbol{X},\boldsymbol{\theta})$ needs to be evaluated multiple times. Model $G_2(\boldsymbol{X},\boldsymbol{\theta})$ is also run a small number of times to get high fidelity data. Assuming higher fidelity models run much slower than lower fidelity ones, time constraints will allow far less high-fidelity simulations. In the proposed methodology, we do not replace $G_2(\boldsymbol{X},\boldsymbol{\theta})$ with a surrogate model. The results of $G_2(\boldsymbol{X},\boldsymbol{\theta})$ runs are only used to correct or adjust the low-fidelity model.

3.2.1 The Bias Correction Method

One option for improving the low fidelity model is by bias correction alone of the low fidelity model, i.e., simply calculating the difference between the low and high-fidelity model outputs for the same input setting and adding that difference to the low fidelity model during the parameter calibration.

A serious challenge for this approach is the low number of high-fidelity simulations available, because of the computational cost. In that case, the low fidelity model would be run at the high-fidelity simulation's input values, and the difference between these outputs will be used to build a surrogate model for the correction term $\boldsymbol{D}_{2,1}$ (the discrepancy between $G_2(\boldsymbol{X},\boldsymbol{\theta})$ and $G_1(\boldsymbol{X},\boldsymbol{\theta})$), in order to calculate the correction term at input conditions not considered in the high-fidelity simulations. As a result, in the same manner as discussed in Section 2.4 with respect to the surrogate of the high-fidelity model, the surrogate model for the correction term will also incur a high error due to the low number of

training points (limited by the number of high-fidelity simulations).

3.2.2 The Pre-Calibration Method

In the pre-calibration method, the high-fidelity results are used to update the distributions of the parameters in the low-fidelity model, and then the updated distributions are used as priors in the second step of calibration with actual experimental data. The assumption is that the high-fidelity model retains physics that might not be present in the low-fidelity model, and that this should influence the values of the parameters as well as the discrepancy, thus providing stronger physics-informed priors for calibration. This is an improvement of the bias-correction method, where the missing physics from the low-fidelity model that are present in the high-fidelity model are lumped into a single correction term, which has significant error due to the low number of training points (see Section 3.2.1).

The proposed multi-fidelity pre-calibration algorithm is as follows:

i. Run the low ($G_1(\boldsymbol{X},\boldsymbol{\theta}_i)$) and high ($G_2(\boldsymbol{X},\boldsymbol{\theta}_i)$) fidelity models to obtain N_1 and N_2 sets of outputs, respectively.

ii. Build $S_1(\boldsymbol{X},\boldsymbol{\theta}_i)$, the surrogate model replacing $G_1(\boldsymbol{X},\boldsymbol{\theta}_i)$. In this step, the variance ε_{surr} of $S_1(\boldsymbol{X},\boldsymbol{\theta}_i)$ is also calculated to account for the surrogate model prediction uncertainty.

iii. Define the priors of the calibration parameters $\boldsymbol{\theta}_i$, and the discrepancy between the models $\boldsymbol{D_{2,1}}$.

iv. Update the parameters of low-fidelity model as well as the discrepancy term with the high-fidelity simulation results, i.e., use the relationship

$$\mathbf{Y_{HF}} = S_1(\boldsymbol{X},\theta_i) + \boldsymbol{\varepsilon_{surr}} + \boldsymbol{D_{2,1}} \tag{13}$$

to compute the posterior distributions of θ_i and $\boldsymbol{D}_{2,1}$, denoted as θ'_i and $\boldsymbol{D}'_{2,1}$ respectively.

v. Define the corrected low-fidelity surrogate model with the updated parameters θ'_i and the updated discrepancy $\boldsymbol{D}'_{2,1}$ as

$$LFcorr = S_1(\boldsymbol{X}, \theta'_i) + \boldsymbol{D'}_{2,1} \tag{14}$$

vi. Assume a prior distribution for the model discrepancy term $\boldsymbol{\varepsilon_d}$ (i.e., the difference between model prediction and experimental observation).

vii. Re-calibrate the dynamics model parameters along with $\boldsymbol{\varepsilon_d}$ using the available experimental data, following the relationship

$$\mathbf{Y_{obs}} = S_1(\boldsymbol{X}, \theta'_i) + \boldsymbol{\varepsilon_{surr}} + \boldsymbol{D'}_{2,1} + \boldsymbol{\varepsilon_d} \tag{15}$$

using the posteriors of the dynamics model parameters from step *iv*. as priors, to compute updated parameters θ''_i and the updated model discrepancy $\boldsymbol{\varepsilon}'_{\boldsymbol{d}}$. (Note that $\boldsymbol{\varepsilon}_{surr}$ and $\boldsymbol{D}'_{2,1}$ are fixed in this step based on the results of step *ii* and step *v* respectively).

The multi-fidelity calibration approach is particularly useful when models of different fidelity retain different physical properties of the system. When calibrating the low-fidelity model using high-fidelity simulations, the parameters to which the high-fidelity model are most sensitive see a substantial shift in their distributions. The more sensitive the high-fidelity model is to the parameters, the less uncertainty the parameter distributions will have in step *v*. Using these distributions as priors in step *vii* ensures the retention of high-fidelity information with respect to the parameter values before calibration with experimental data. This also reduces the computational cost by effectively shrinking the parameter

sampling space in step *vii*. The parameters are only sampled in the posterior region (defined in step *v*), not in the full range covered by the original priors.

Although high-fidelity models may be more exact, the lower fidelity ones usually capture the global behavior of the system, mainly because the high-fidelity simulation cannot be run over the full domain because of limited resources. In dynamical systems, fusion of information from multiple fidelities is valuable because lower fidelity models (e.g., PSD analysis), retain the average energy response, whereas higher fidelity models, (e.g., time history analysis), preserves the peaks in the signals (two very different signals can have the same PSD graph, if their energy peaks at the same frequencies). Also, a PSD analysis output is only derived from forces varying over time. This means initial conditions on the structure are not included in the calculations, which can influence the final result. A full time history analysis is not limited by this condition, and any constant force on the system affects the output. Moreover, typically, PSD analyses combine modal static forces, which can be translated into (stiffness) times (mode shape forces). In a full solution method (time history), inertia, damping and static loads are used to calculate the nodal reaction loads at each time step. This has a direct influence on how stiff the model is, and how the damping effect is expressed. The pre-calibration method allows the transfer of the physics from the HF model to the LF model through the parameters as well as the discrepancy term because of stronger, physics-informed priors of these parameters. These differences influence the sensitivity of these models to various input parameters, and thus the accuracy of the calibration results.

In order to assess the proposed approach, the multi-fidelity calibration results are compared to calibrations done with the single fidelity models (low and high), using Bayesian hypothesis testing, as discussed in Section 2.6 . In this chapter, the following three calibration approaches (treated as models) are compared:

- The low-fidelity surrogate model calibrated using experimental data (LF)
- The high-fidelity surrogate model calibrated using experimental data (HF)
- The low-fidelity surrogate model pre-calibrated with high-fidelity simulations then re-calibrated with the experimental data (LFcorr).

In order to compare the three models using the Bayes factor (described in Section 2.6), we calculate the likelihood of observing the experimental data (independent of the data used in the calibration process) for each model, then normalize them with respect to the likelihood of observing the data in the low-fidelity model. The results are displayed as

$$1 : \frac{L_{HF}}{L_{LF}} : \frac{L_{LFcorr}}{L_{LF}} \tag{16}$$

where L represents the likelihood, and the subscript denotes the model used.

3.3 Numerical Example

3.3.1 Problem Description

The example problem is a simplified representation of an aircraft fuselage panel located next to the engine, subjected to dynamic acoustic loading (P). The panel is curved, as shown in Fig. 5, and is modeled using the FEA software ANSYS. The objective is to calibrate the damping coefficient of the panel, using experimental strain data observed under applied acoustic loading. The strain is recorded at seven different locations of the panel. Three strain gages are placed on the top (SG1, SG2 and SG3), two on the bottom (SG4 and SG5) as shown in Fig. 5, with the center gage recording strain in three different directions. The experiments are performed in room temperature, at varying levels (decibels) of acoustic

excitation. In this chapter, the damping is calibrated under one level of excitation only (140 dB) for the sake of illustration.

No repeated measurements under the same input are assumed to be available. This hinders the ability to calculate any spatial correlation between the strain gages. However, repeated runs of the high-fidelity simulations allow the calculation of the spatial correlation between the outputs at those locations. The correlation coefficient was found to be equal to 0.85 among the model outputs at the three strain gage locations, and we used the same correlation coefficient among the observations, observation errors, and model discrepancies at the three locations.

The experimental strain measurement is saved for a duration of sixty seconds, at a frequency of 50,000 recordings per second, for a total of three million data points. In order to compare the experimental signal to the simulation outputs, the strain signal in the time domain is transformed into a power spectral density (PSD) in the frequency domain, and the energy under the PSD curve, i.e., the root mean square (RMS) value of the signal (the area under the curve) is calculated.

The PSD describes how the power of a signal or time series is distributed over different frequencies. For a signal $X(t)$, it is calculated as follows:

$$S_{xx}(\omega) = \lim_{T\to\infty}\left[\frac{E[\left|F_{X_T}(\omega)\right|^2]}{2T}\right] \tag{17}$$

where $E[]$ is the expected value, and $F_{X_T}(\omega) = \int_{-\infty}^{\infty} X_T(t)e^{-jwt}dt$ the Fourier transform of $X(t)$.

A microphone, located near the center of the panel, captures the acoustic load seen by the panel as it vibrates. This measurement is used as the input load on the simulated structure.

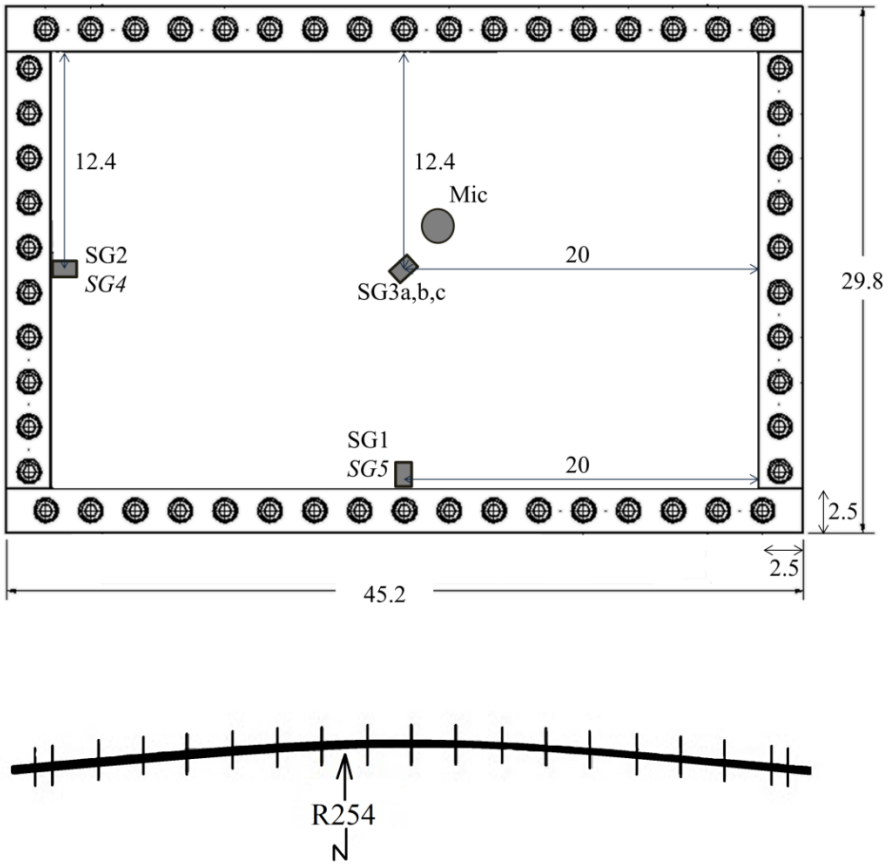

Fig. 5: Curved panel dimensions and strain gage locations (units: cm)

The material damping, in this study, is modeled as a viscous damping throughout the panel. In addition, and due to the panel attachment boundaries (the edge of the plate is sandwiched between two 1” wide metal strips, and bolted to the test frame, as shown in Fig. 5), when the acoustic load is applied on the plate, a constant mechanical damping is expressed in which energy is absorbed via sliding friction. This form of damping is defined as Coulomb damping [69], and we denote it as frictional damping for a width of 1” around the perimeter of the panel.

The boundary fixity is also a calibration variable, to account for the uncertainty in building the test

setup (loose bolts, for ex.), and is described by a fixity ratio *FR* = length of fixed plate boundary /total boundary length (see Fig. 6).

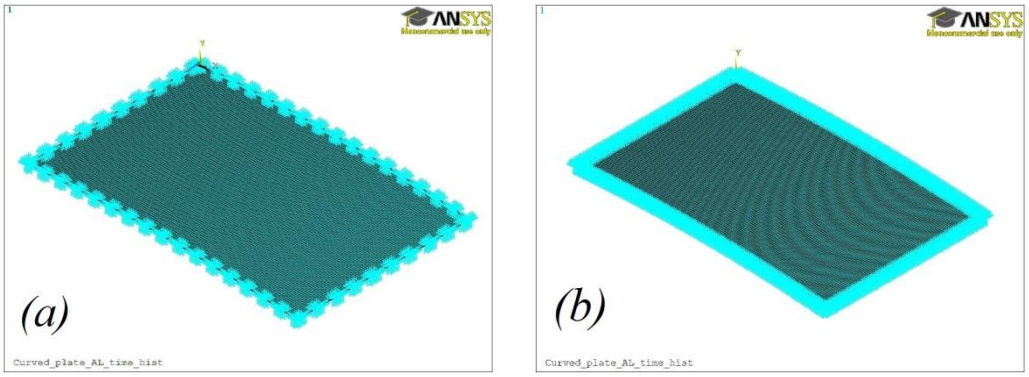

Fig. 6: Boundaries with different fixity ratios (FR): (a) FR = 0.5, (b) FR = 1

Two physics models of different fidelities were considered:

- Model 1: A power spectral density analysis, which consists of a linear combination of mode shape effects (referred to as low-fidelity model).
- Model 2: A full transient analysis where the acoustic loading is applied as a dynamic time history input (referred to as high-fidelity model).

Model 1 and Model 2 have the same finite element mesh. In addition, the materials, the boundary conditions and the mesh resolution are similar. The models differ in the application of loads, the analysis method, and the output type.

In Model 1, the input acoustic load applied is the Welch power spectral density (PSD) [70] of the experimental 140 dB acoustic load. The PSD is calculated with the entire 140 dB signal, for the full duration of sixty seconds. The output of Model 1 is a strain PSD curve. The strain RMS is calculated

and used for comparison with the experimental data. This simulation is considered a lower fidelity approximation of the experiment because the PSD input is not unique to the signal it is calculated from, since the phase component is discarded. Also, the spectrum analysis in ANSYS is a linear combination of the mode effects on the structure. Finally, even though Model 1 is inexpensive to run (one simulation takes about 9.5 minutes to complete on a personal computer), it does not allow the user to add initial conditions on the structure. Initial stress resulting from fixing the plate on the test-rig (a uniform load has a PSD of zero) will not contribute to the RMS strain output.

Model 2, in contrast, is a full transient dynamic analysis of the panel. The output is a strain signal also converted to a PSD curve, and the strain RMS is derived from it. The model run is quite time-consuming, allowing only 0.2 sec of the input signal (of the full 60 secs of data available) to be simulated with the available computational resources, and each simulation takes about 5.5 hours on a personal computer (35 times slower than Model 1). However, Model 2 does allow us to specify an initial stress on the panel, and preliminary test runs have shown that a uniform initial load on the panel is consistent with the experimental observation (See discussion in Section 3.3.3 and Fig. 16). In Fig. 16, the initial stress specification is referred to as IC (initial condition).

The hypothesis of this dissertation is that initial improvement of the low-fidelity surrogate with a few runs of the higher fidelity model allows the use of information from both models in the final calibration of the system parameters. In this numerical example, the fused information consists of the full length of the signal in the form of the PSD, and the transient behavior as well as the initial conditions incorporated in the full dynamic analysis. The two models capture two different types of information, and both are effectively used in the proposed calibration strategy. This strategy also amounts to developing physics-informed stronger priors for calibration, thus reducing the uncertainty about the system parameters.

3.3.2 Results

Three calibration results are being compared in this section: (1) calibration of the low-fidelity surrogate model with experimental data using correlated parameters and uncertainties, (2) calibration of the high-fidelity surrogate model with experimental data using correlated parameters and uncertainties, and (3) calibration of the improved low-fidelity surrogate model with the experimental data using correlated parameters and uncertainties.

Table 1 shows details of the surrogate model properties for each case.

Table 1: Surrogate model properties

	LF	*HF*	*LFcorr*
Surrogate Type	*PCE*	*PCE*	*PCE*
Order	*2*	*1*	*2*
Training points	*40*	*9*	*40*

The calibration parameters are: frictional damping (*FR_DC*), material damping (*MT_DC*), fixity ratio (*FR*), as well as the discrepancy term ($\boldsymbol{\varepsilon_d}$) and standard deviation of the observation error ($\boldsymbol{\sigma_{obs}}$). Since we are measuring three outputs, there are correspondingly three discrepancy terms and three observation errors. The priors for the calibration parameters are assumed the same for the low-fidelity, high-fidelity and corrected low-fidelity models. They are all uninformed priors (i.e. uniform distributions $U(a,b)$) for the model parameters, normal distributions ($N(\boldsymbol{\mu_d}, \boldsymbol{\sigma_d})$) for the discrepancy terms with uniform priors for $\boldsymbol{\mu_d}$ and $\boldsymbol{\sigma_d}$, and Jeffrey's priors [71] for the $\boldsymbol{\sigma}_{obs}$ terms which is the correct choice of an uninformed prior for standard deviation, $\pi(\boldsymbol{\sigma}_{obs}) \propto 1/\sigma$. The experimental error itself is assumed to follow a normal

distribution with zero mean (Table 2). The same prior parameter distributions are assumed at all three strain gage locations, so they are not repeated in Table 2.

Table 2: Prior distributions of calibration parameters

Calibration parameter	*Dist. type*	*Parameter 1*	*Parameter 2*
FR_DC	*Uniform*	$a = 10^{-5}$	$b = 10^{-2}$
MT_DC	*Uniform*	$a = 5.10^{-7}$	$b = 10^{-5}$
FR	*Uniform*	$a = 0.7$	$b = 1$
μ_d	*Uniform*	$a = -10^{-2}$	$b = 10^{-2}$
σ_d	*Uniform*	$a = 5.10^{-8}$	$b = 5.10^{-6}$
σ_{obs}	*Jeffreys'*	$\mu = 0$	$\sigma = 10^{-7}$

Only one set of experimental data is available (one observation at each strain gage location). Three strain gage outputs are used for calibration (i.e., $n = 3$ with respect to Eqs. (7) and (8)), and a fourth one is used to compute the Bayes factor (likelihood ratio) to compare the results of the different calibration options. The three remaining strain gages (out of the total seven placed on the plate) were discarded from this study because the values recorded were very low compared to the rest of the strain gages.

Fig. 7 shows the posteriors of one of the discrepancy terms (at strain gage location SG4) for illustration purposes. The posteriors of frictional damping, material damping, and fixity ratio are shown in Figs. 8 to 10. Note that the posterior densities are only meaningful within the ranges of the priors. The use of kernel density smoothing results in the posterior densities extending outside the priors in Figs. 8 to 10 (and also in Figs. 12 to 14).

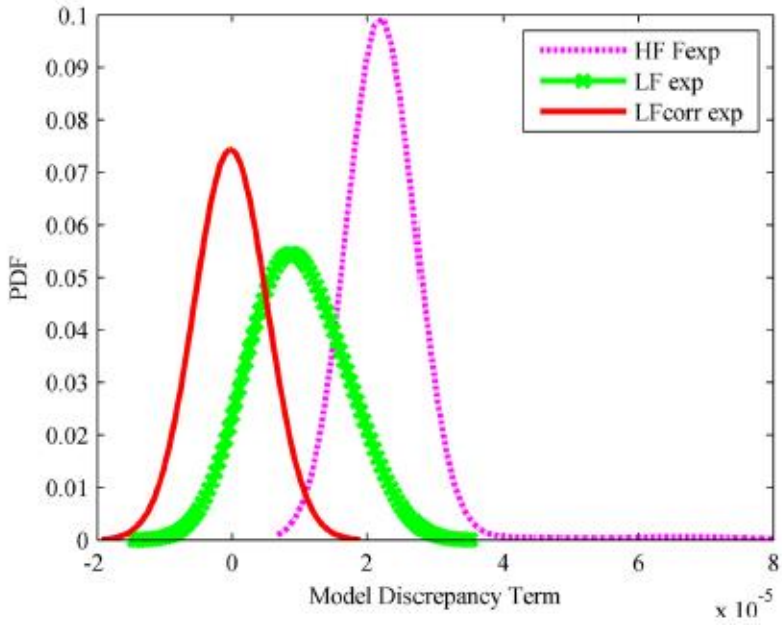

Fig. 7: Model discrepancy posteriors at strain gage location SG4

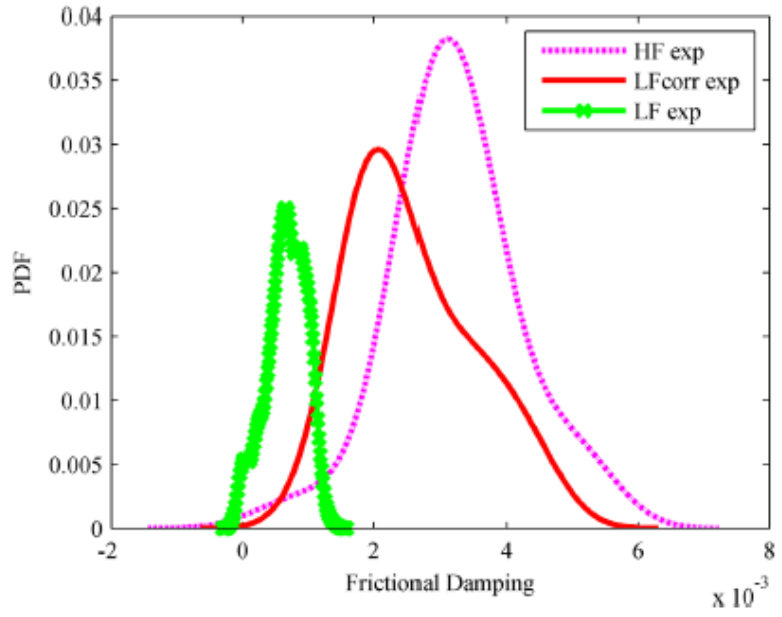

Fig. 8: Frictional damping posteriors. Prior ~ Uniform [-10^{-5}, 10^{-2}]

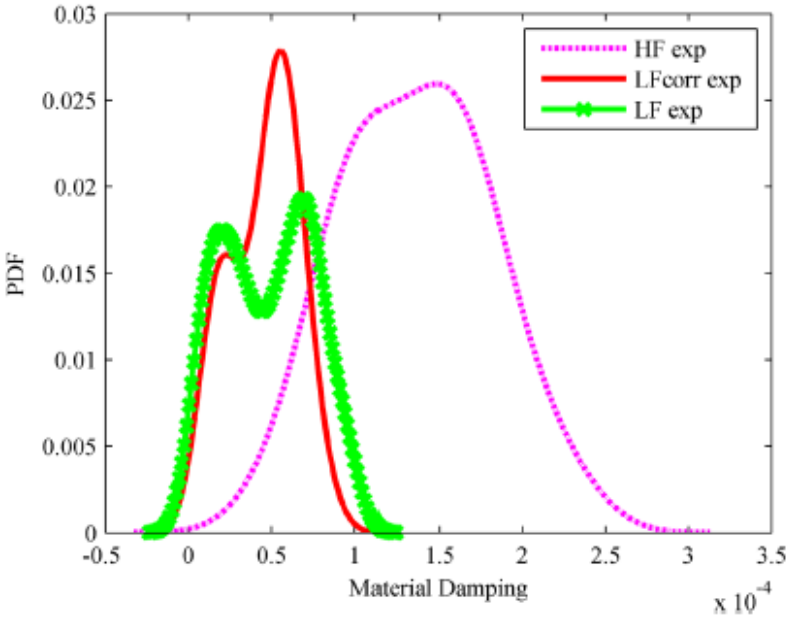

Fig. 9: Material damping posteriors. Prior ~ Uniform [5.10^{-7}, 10^{-2}]

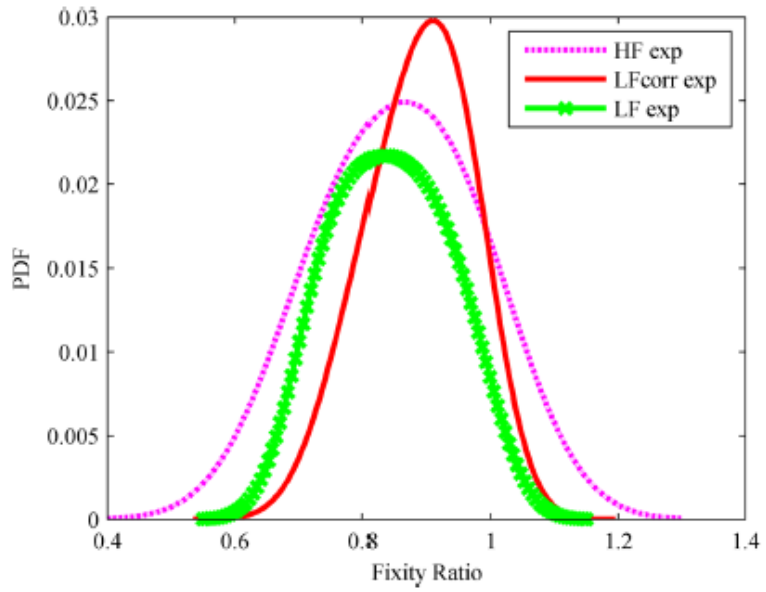

Fig. 10: Fixity ratio posteriors. Prior ~ Uniform [0.7, 1]

The calibrations were also done for the case of independent model outputs and observations, and the

associated errors for illustration purposes, and Figs. 11 to 14 compare the posteriors of the LFcorr calibrations for the independent and correlated cases. This shows that correlation has a pronounced effect on most of the unknown quantities' posteriors, and should be included in the calibration exercise.

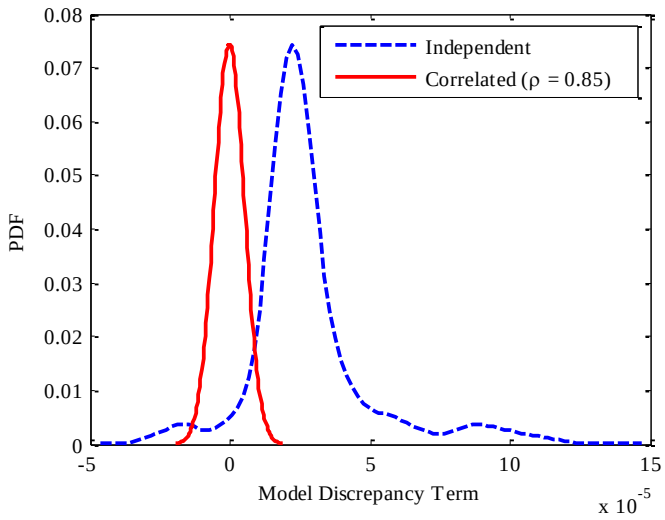

Fig. 11: Model discrepancy posteriors for independent and correlated parameters

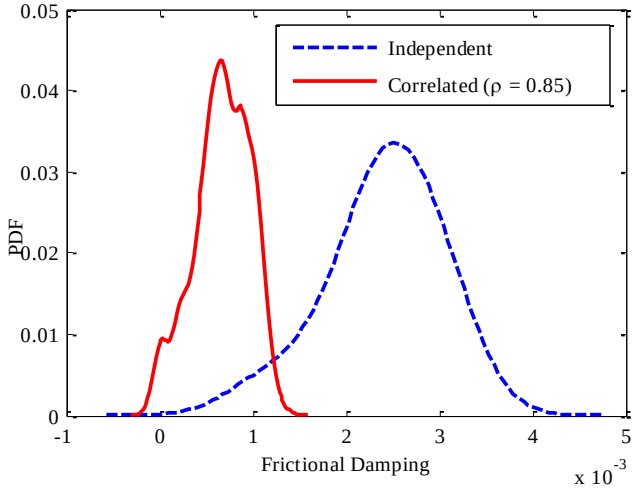

Fig. 12: Frictional damping posteriors for independent and correlated parameters

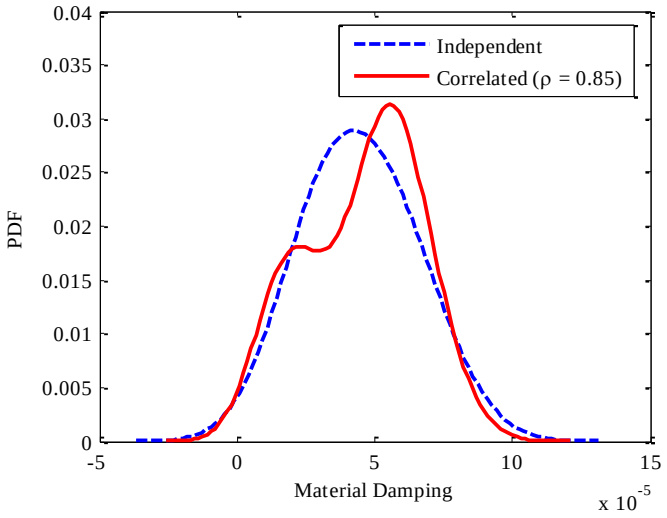

Fig. 13: Material damping posteriors for independent and correlated parameters

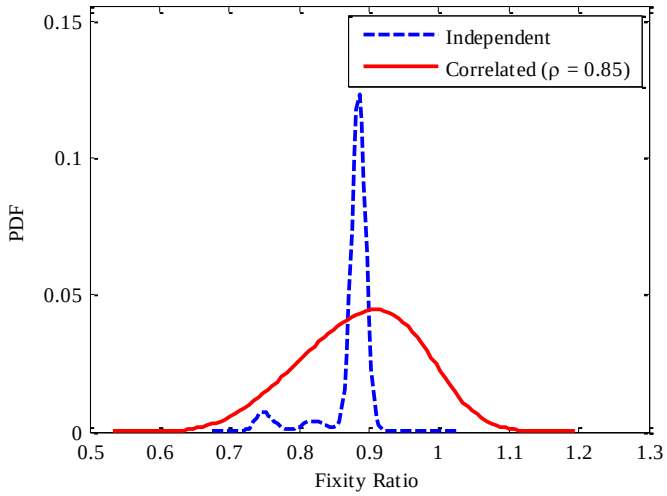

Fig. 14: Fixity ratio posteriors for independent and correlated parameters

Using the observation at the fourth strain gage, the likelihood ratios among the three calibration options were computed as

LF : HF : LFcorr = 1 : 2.52 : 3.97

This indicates superior performance of the multi-fidelity calibration method in predicting the response of the fourth strain gage compared to the individual low-fidelity and high-fidelity calibrations.

3.3.3 Checking the calibration results

A predictive check was performed with the calibration posteriors at the three sesor locations. The results for RMS strain at SG1 under two load combinations (columns 1 and 2) are shown in Fig. 15. The results for SG2 and SG4 show similar trends, and were ommitted for brevity. LFcorr denotes the strain predictions using the corrected low-fidelity model, $\mathbf{Y_{obs}}$ the measured strain at SG1, LF the strain predictions using the initial priors, and LF HF the strain predictions using the physics-informed priors. Row 1 of Fig. 14 includes the measurement error in the LFcorr strain prediction, and $\mathbf{Y_{obs}}$ is a deterministic value. Row 2 includes the measurement error in $\mathbf{Y_{obs}}$.

The predictive check shows that the sensor data lies within the posterior predictions in all cases. However, for high temperature (Comb. 2), the measruement uncertainty is so large that it accounts for almost all the uncertainty in the output. In addition, we can see that the predictions from LF HF and LFcorr are very close and narrow. This implies that the experimental output at SG1 for high temperatures did not significantly affect the calibration result because of the high uncertainty in the strain gage reading. The uncertainty in the prediction was already very small using physics-informed priors (LF HF), and the calibration with experimental data only shifted the prediction distribution a little, and did not contribute to any uncertainty reduction. In other words, when the measurement uncertainty is large, it does not provide significant information gain, i.e., it is mostly non-informative.

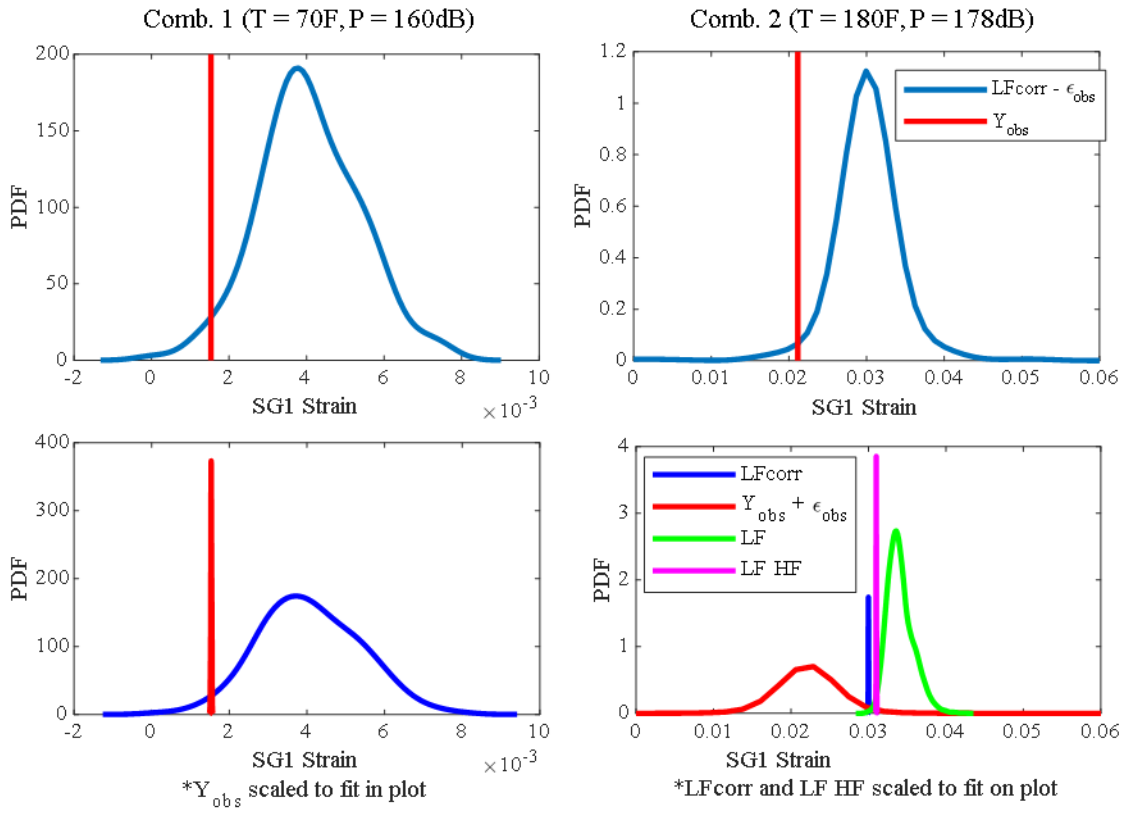

Fig. 15: Predictive check at SG1

3.3.4 Discussion

The main difference between Models 1 and 2, besides the analysis type, is the initial stress added in Model 2, in the form of a distributed uniform load of 8.5 10^{-3} lb/in^2. Preliminary testing of Model 2 with and without initial stress showed that, without adding a uniform load on the panel, the strain amplitude was much lower than the experimental output, as seen in Fig. 16 The initial stress is deforming the panel and allowing it to vibrate with a higher amplitude around a non-zero equilibrium.

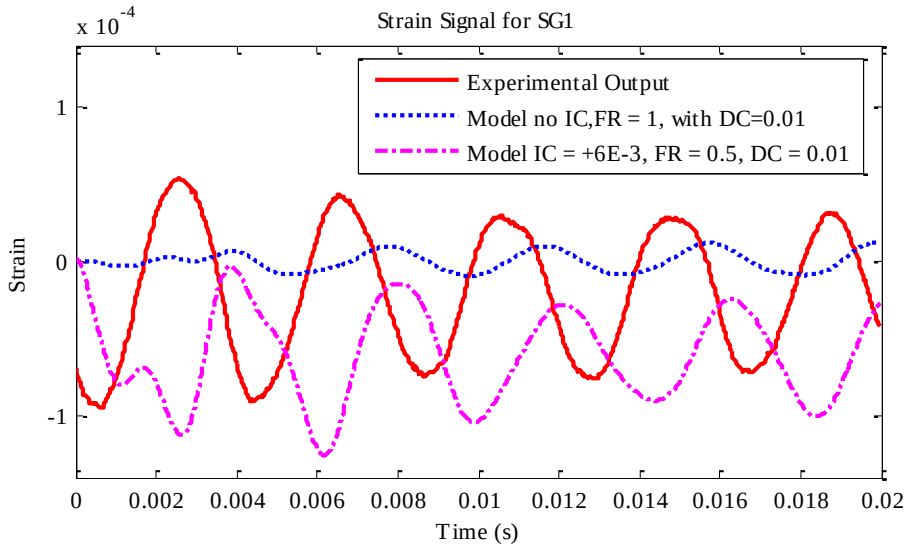

Fig. 16: Preliminary model testing

The calibration results show the effect of ignoring the initial stress. The strain RMS is directly proportional to the signal amplitude, and in order to maximize the strain RMS from the low-fidelity model, the posteriors from the calibration with Model 1 underestimate the frictional damping and the fixity ratio, in an attempt to recover the energy under the PSD curve. This loss of accuracy is also shown in the discrepancy term, which is much greater (in magnitude) than the rest of the models.

It is observed that the corrected low-fidelity posteriors are closer to the low-fidelity posteriors for material damping and are closer to the high-fidelity posteriors for frictional damping. Calibrating both model parameters and discrepancy of the low-fidelity model with high-fidelity simulations allowed the retention of information from both models with respect to the parameters.

Most importantly, the results show the fusion of information from the low and high-fidelity models in the proposed methodology, combining the different sensitivities of the high-fidelity and low-fidelity

models to the parameters. A simple sensitivity analysis shows that, when the material damping is increased by 20%, the strain PSD in SG1 increases by 8% in the low-fidelity model, and 5% in the high-fidelity model. On the other hand, a 20% increase in the frictional damping results in 2.5% increase of strain in the low-fidelity model, versus 15% in the high-fidelity model. This shows that the low-fidelity model is more sensitive to material damping, whereas the high-fidelity model is more sensitive to frictional damping.

Using the proposed calibration method, the final calibration results take advantage of the sensitivity of the low-fidelity and high-fidelity models to different parameters. When using the corrected low fidelity model, the parameters' posteriors converge towards the posteriors of the models that are most sensitive to them, i.e., in the calibration of corrected low-fidelity model, the material damping posterior converges towards the low-fidelity model posterior, and the frictional damping posterior converges towards the high-fidelity model posterior. This allows the fusion of information from both fidelity models in a manner that captures the sensitivities of different fidelity models to different parameters.

Not only were the results in favor of the use of the improved low-fidelity model in the calibration process, but its convergence was faster than both low-fidelity and high-fidelity calibrations with experimental data. This is due to multiple factors: the low-fidelity model by itself has very low accuracy, but its surrogate has high precision, due to the high number of training points available. This makes convergence hard, since the low-fidelity output is far from the experimental data. Conversely, the high-fidelity model is more accurate, but its surrogate is considerably less precise due to the number of training points, and thus a high surrogate model error, which slows down the convergence considerably. The pre-calibration method proposed results in two sequential smaller calibrations, where the first directs the second to the final converged answer. Effectively, the sampling space in the calibration with

experimental data is reduced, since the priors used in this step consist of the posteriors coming from the calibration of the low-fidelity surrogate with the high-fidelity simulations. In other words, we are using stronger priors in the calibration with corrected low-fidelity, which causes faster convergence. The times to convergence (on a personal desktop computer) of all three analyses are shown in Fig. 17.

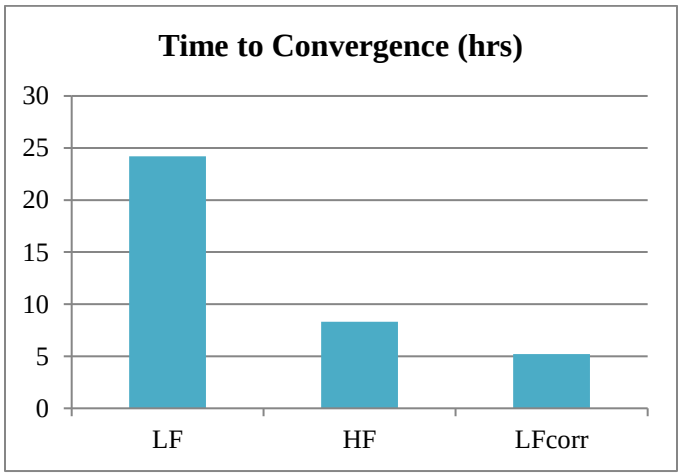

Fig. 17: Time to convergence of three calibration strategies

Furthermore, the likelihood ratio calculated in Section 3.3.2 shows that the calibration result of the pre-calibrated low-fidelity model is much higher than all other models. When this likelihood comparison is considered along with the computational efficiency of the two-step approach, it appears that the proposed methodology offers a promising strategy in the use of multiple models of different fidelities in the calibration of model parameters.

As with any parameter estimation problem, the calibration results are only valid within the range of the test data. The formulation of the calibration procedure is general and is able to include correlations among model outputs, model errors as well as observation errors, as illustrated in the numerical example. The model discrepancy terms were represented in the numerical example either as unknown constants

or normal random variables with unknown parameters. However, more elaborate representations of model discrepancy, such as input-dependent random field (following the Kennedy and O'Hagan approach) could also be included in the proposed formulation; such implementations are limited by the amount of data available. In the presence of limited data, the choice of priors also affects the calibration result.

3.4 Conclusion

This chapter investigated a multi-fidelity approach for the Bayesian calibration of model parameters. Surrogate models become necessary in the context of Bayesian calibration due to the large number of model evaluations required in Markov Chain Monte Carlo sampling. A few time-consuming high-fidelity simulations were used to improve the surrogate of the inexpensive low-fidelity model, and the improved low-fidelity surrogate was used for parameter calibration with experimental data. This two-step method allows the fusion of information from models of different fidelity and is particularly useful when only a small number of experimental data points are available, and calibration convergence is difficult with uninformed prior distributions of the parameters.

Future work needs to investigate the efficacy of this approach when more than two models are available (each with a different level of fidelity) and find a systematic quantitative way of using the available information, since multiple combinations are possible. Ranking of fidelity in a comprehensive way is also a challenge that needs to be addressed: some models might have higher fidelity compared to others in one aspect, and lower fidelity in another (if, for example, one detailed model only represents a partial structure, whereas a simpler model represents the full design).

The proposed fusion of information from models of different fidelity is an effective way to create

stronger physics-informed priors for calibration with sparse experimental data. This is a general approach that can be useful for a broad range of applications, not only the dynamic structure studied in this dissertation.

The calibration becomes more complicated when the model parameters are input-dependent (e.g., load-dependent damping), and Chapter 4 extends the proposed multi-fidelity approach to account for this dependence.

Chapter 4

Input-Dependence Effects in Dynamics Model Calibration

In this chapter, the multi-fidelity method is extended to calibration of input-dependent system parameters. High temperature loads are added in the curved panel application, and we assume the damping to be a function of the acoustic load and temperature amplitudes. We also study the effect of the input on the sensors (namely the effect of high temperature on the uncertainty in the strain gages).

4.1 Introduction

The focus in this chapter is on input-dependent parameter calibration within the multi-fidelity framework developed in Chapter 3. Complications in calibration arise in the presence of nonlinear behavior. Typical sources of nonlinearity in structural dynamics are geometric nonlinearity (due to large deformations), material nonlinearity (nonlinear stress/strain constitutive law, strain hardening), damping dissipation (dry friction – contact and sliding between bodies, and hysteretic damping [72] effects), boundary conditions (e.g., surface/fluid interactions), external nonlinear body forces (e.g., hydrodynamic forces, temperature), etc. [73]. Model parameters in such situations could be input-dependent. Calibration considering input-dependent system parameters has also been referred to as functional calibration. Pourhabib and Balasundaram [74] showed that calibration of parameters that are input-dependent is a curve-to-surface matching problem, and used a sum of splines to represent that relationship. Plumlee et al. [75] considered calibration parameters as analytical functions of inputs to replace previously used empirical definitions (data fitting by least squares) in the ion channel models of cardiac cells. Brown and Atamturktur [76] used a nonparametric approach to calibrate input-dependent

system parameters, in which a Gaussian Process (GP) model is used to represent the relationship between the parameters and the input.

In real application problems, many challenges arise in the experimental, modeling and calibration stages. In experiments, replicating the natural phenomena in laboratory settings while preserving the quality of the recorded data is difficult, especially in the presence of high temperature, which could negatively affect the recording devices such as strain gages. Modeling the experimental setting also brings high uncertainty in capturing all the present physical phenomena. The increased number of parameters makes effective calibration hard, especially when a low number of experimental data is available. Complex interactions can lead to having nonlinearity and input-dependence simultaneously active, thus there is a need to distinguish between these effects in the calibration process.

The aim of this chapter is to extend the approach of fusing information from models of different levels of fidelity to Bayesian calibration of input-dependent model parameters. We consider geometric nonlinearity (effect of large deformations) and material nonlinearity (nonlinear stress-strain relationships that can also be temperature dependent) in the modeling phase that are distinguished from the input-dependence of the parameters. We assume a functional dependence between the inputs and the parameters, organize them in a Bayesian network, and use a multi-fidelity calibration approach to update the coefficients of these functional relations (i.e., the hyper-parameters). We also include the effect of different types of inputs on the sensors (i.e., strain gages) and use realistic experimental data to illustrate the benefits of this approach.

The rest of this chapter is organized as follows: Section 4.2 proposes the extension of the multi-fidelity Bayesian calibration approach to input-dependent parameter calibration in the presence of

nonlinear and input-dependent sensor performance. Section 4.3 illustrates the methodology using experimental data obtained from a curved panel subjected to acoustic and thermal loading and investigates the calibration of the damping as a function of these inputs, including the effect of the input on the performance of the strain gages. Section 4.4 summarizes the contributions of this work and explores possible future extensions.

4.2 Multi-Fidelity Calibration Method for Input-dependent System Parameters

In this section, multi-fidelity calibration is extended for the calibration of input-dependent system parameters.

4.2.1 Model Calibration with Input-Dependent Parameters

When the parameters are input-dependent, the model calibration formulation in Eq. (5) can be written as:

$$\mathbf{Y}_{\mathbf{obs}} + \boldsymbol{\varepsilon}_{obs}(\boldsymbol{X}) = G(\boldsymbol{X} + \boldsymbol{\varepsilon}_{in}, \boldsymbol{\theta}(\boldsymbol{X})) + \boldsymbol{\varepsilon}_{surr} + \boldsymbol{\varepsilon}_{d}(\boldsymbol{X}) \tag{18}$$

where $\boldsymbol{\varepsilon}_{obs}(\boldsymbol{X}) \sim N(0, \boldsymbol{\sigma}_{obs}(\boldsymbol{X}))$ and $\boldsymbol{\varepsilon}_{d}(\boldsymbol{X})$ is a vector of model discrepancy terms function of input X, one for each output.

Eq. (18) considers the dependence of model parameters $\boldsymbol{\theta}$ on the input $\boldsymbol{X}$. If the data on $\boldsymbol{X}$ and corresponding $\boldsymbol{\theta}$ are readily available, then building the relationship between inputs and model parameters is simple. However, in general, model parameters are not directly measured but are inferred (calibrated) based on measurements of model inputs and outputs. In this dissertation, we assume an analytical relationship between inputs $\boldsymbol{X}$ and model parameters $\boldsymbol{\theta}$, and calibrate the coefficients of this

assumed relationship (i.e., the hyper-parameters $\boldsymbol{\lambda_\theta}$) along with the input errors $\boldsymbol{\varepsilon_{in}}$, the model discrepancy hyper-parameters $\boldsymbol{\lambda_{\varepsilon_d}}$ and the observed error standard deviation hyper-parameters $\boldsymbol{\lambda_{obs}}$ (refer to Bayesian network in Fig. 18). A simple example of this relationship can have a polynomial form:

$$\boldsymbol{\theta}(\boldsymbol{X}) = \sum_i \sum_j \lambda_{\theta ij} \boldsymbol{X}_i^j + \boldsymbol{\varepsilon_\theta} \tag{19}$$

where *i* refers to the different inputs, *j* is the order of the polynomial, and $\boldsymbol{\varepsilon_\theta} \sim N(0, k(\boldsymbol{X}, \boldsymbol{X}'; \boldsymbol{\varphi}))$ is the residual modeled as a Gaussian process (GP) with stationary covariance function $k(*)$ (and its set of coefficients φ). X and X' are the input vectors at two different locations.

The input-dependent error terms in Eq. (19) refer to model discrepancy (e.g. using a polynomial functional dependence similarly to $\boldsymbol{\theta}(\boldsymbol{X})$):

$$\boldsymbol{\varepsilon_d}(\boldsymbol{X}) = \sum_i \sum_j \lambda_{\varepsilon ij} \boldsymbol{X}_i^j + \boldsymbol{\varepsilon}_\varepsilon \tag{20}$$

as well as the observation error standard deviation

$$\boldsymbol{\sigma_{obs}}(\boldsymbol{X}) = \sum_i \sum_j \lambda_{\sigma ij} \boldsymbol{X}_i^j + \boldsymbol{\varepsilon}_\sigma \tag{21}$$

This is critical in problems where the input has a pronounced effect on these errors. For example, we know that model form error is dependent on location. In addition, a higher magnitude input (such as temperature) could result in larger observation error at one location compared to another (due to temperature effect on sensor performance when the temperature distribution is non-uniform). This effect is transferred to the calibration process, i.e., larger uncertainty in the observation leads to larger uncertainty in the calibration result. Therefore, we also consider input-dependence of the observation error in Eq. (18).

The dependence on the input variables of the parameters θ as well as the measurement standard deviation $\boldsymbol{\sigma_{obs}}$ and the discrepancy $\boldsymbol{\varepsilon_d}$ is represented by their hyper-parameters (respectively) $\boldsymbol{\lambda_\theta}, \boldsymbol{\lambda_{obs}}$ and $\boldsymbol{\lambda_{\varepsilon_d}}$. The hyper-parameters $\boldsymbol{\lambda}$ are calibrated using Bayes' theorem as:

$$\pi(\boldsymbol{\lambda_\theta}, \boldsymbol{\lambda_{obs}}, \boldsymbol{\lambda_{\varepsilon_d}} | \mathbf{y_D}) = \frac{L(\boldsymbol{\lambda_\theta}, \boldsymbol{\lambda_{obs}}, \boldsymbol{\lambda_{\varepsilon_d}})\ \pi(\boldsymbol{\lambda_\theta}, \boldsymbol{\lambda_{obs}}, \boldsymbol{\lambda_{\varepsilon_d}})}{\int L(\boldsymbol{\lambda_\theta}, \boldsymbol{\lambda_{obs}}, \boldsymbol{\lambda_{\varepsilon_d}})\ \pi(\boldsymbol{\lambda_\theta}, \boldsymbol{\lambda_{obs}}, \boldsymbol{\lambda_{\varepsilon_d}}) d\boldsymbol{\lambda_\theta} d\boldsymbol{\lambda_{obs}}\ d\boldsymbol{\lambda_{\varepsilon_d}}} \tag{22}$$

where

$$L(\boldsymbol{\lambda_\theta}, \boldsymbol{\lambda_{obs}}, \boldsymbol{\lambda_{\varepsilon_d}}) \propto \prod_{i=1}^{m} \pi\,(\mathbf{Y_{obs}}_i = \mathbf{y_D}_i \mid \boldsymbol{x_{Di}}, \boldsymbol{\lambda_\theta}, \boldsymbol{\lambda_{obs}}, \boldsymbol{\lambda_{\varepsilon_d}}) \tag{23}$$

Here, $\pi(\boldsymbol{\lambda_\theta}, \boldsymbol{\lambda_{obs}}, \boldsymbol{\lambda_{\varepsilon_d}})$ is the prior joint PDF of $\boldsymbol{\lambda_\theta}, \boldsymbol{\lambda_{obs}}$ and $\boldsymbol{\lambda_{\varepsilon_d}}$; $\pi(\boldsymbol{\lambda_\theta}, \boldsymbol{\lambda_{obs}}, \boldsymbol{\lambda_{\varepsilon_d}} | \mathbf{y_D})$ is the joint posterior PDF of $\boldsymbol{\lambda_\theta}, \boldsymbol{\lambda_{obs}}$ and $\boldsymbol{\lambda_{\varepsilon_d}}$ given $\mathbf{y_D}$; and $L(\boldsymbol{\lambda_\theta}, \boldsymbol{\lambda_{obs}}, \boldsymbol{\lambda_{\varepsilon_d}})$ is the joint likelihood function of $\boldsymbol{\lambda_\theta}, \boldsymbol{\lambda_{obs}}$ and $\boldsymbol{\lambda_{\varepsilon_d}}$. $\mathbf{y_{D_i}}$ is the vector of the n outputs $\mathbf{Y_{obs}}_i$ for each individual input setting $\boldsymbol{x_{Di}}$, and i = 1 to m, where m is the number of settings for which the outputs are observed. The likelihood function is based on the joint PDF of the observations $\mathbf{y_{D_i}}$, conditioned on $\boldsymbol{\lambda_\theta}, \boldsymbol{\lambda_{obs}}$ and $\boldsymbol{\lambda_{\varepsilon_d}}$.

If the observed outputs are independent, the likelihood in Eq. (23) is:

$$L(\boldsymbol{\lambda_\theta}, \boldsymbol{\lambda_{obs}}, \boldsymbol{\lambda_{\varepsilon_d}}) \propto \prod_{i=1}^{m} \prod_{\mathrm{j}=1}^{\mathrm{n}} \pi\,(\mathrm{y_{Dij}} \mid \boldsymbol{x_{Di}}, \boldsymbol{\lambda_\theta}, \boldsymbol{\lambda_{obs}}, \boldsymbol{\lambda_{\varepsilon_d}}) \tag{24}$$

In this dissertation, slice sampling (described in Section 2.2) is used to calculate the posteriors of the hyper-parameters.

All the variables discussed in the above calibration problem can be represented through a Bayesian network as shown in Fig. 18, where $\boldsymbol{\varepsilon_{in}^X} \sim N(0, \boldsymbol{\sigma_{in}^X})$ is the input error, one for each input; $\boldsymbol{\varepsilon_\theta}$ is the model

discrepancy for $\boldsymbol{\theta}$ and $\mathbf{Y}$ is the vector of model outputs.

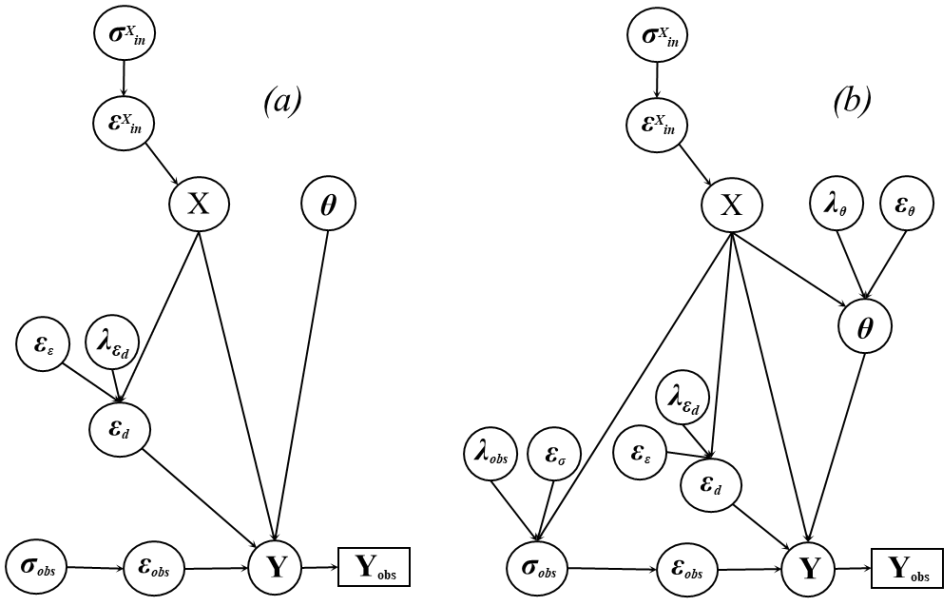

Fig. 18: Bayesian Network (a) without input-dependence, and (b) with input-dependence

This method of modeling the input-dependence of parameters using a Bayesian network combines the relationship between parameters and inputs with information from experimental data and prior knowledge in the calibration of system parameters. However, when including input effects on the parameters in this manner, the number of parameters to estimate could increase drastically. Often, either due to sparseness of data or to minimize the computational expense, the number of calibration parameters may need to be reduced by introducing approximations, such as assuming some parameters to have known deterministic values, known probability distributions, or known (or ignored) correlations.

4.2.2 Dynamics Model Calibration

Consider a structure subjected to vibratory loading as well as thermal loading where it is hypothesized

that frictional (Coulomb) damping is dominant at the joints and material (Rayleigh) damping is dominant away from the joints, and these two damping parameters are required to be calibrated using observed dynamic strain data $\mathbf{Y_{obs}}$. Suppose the initial stress condition (*IC*) and the boundary condition (*BC*) are also uncertain and need to be calibrated. The input dependence of the damping parameters needs to be considered, as well as the input effects on the sensor performance. If the frictional damping is modeled as a linear function of the vibratory load *P* and the differential thermal load $\Delta T = T - T_{room}$ (where T_{room} is the room temperature), it can be written as:

$$FD(P, \Delta T) = a_1 + a_2 \times P + a_3 \times \Delta T + \varepsilon_{FD} \tag{25}$$

where ε_{FD} is the corresponding discrepancy term, modeled as a Gaussian process, i.e., $\varepsilon_{FD}(\boldsymbol{X}) \sim N(0, k_{FD}([P, \Delta T], [P, \Delta T]', \boldsymbol{\varphi_{FD}})$ and $\boldsymbol{\varphi_{FD}}$ is the vector of hyper-parameters of the covariance function. If a squared exponential covariance function is assumed, $k_{FD} = {\varphi^{(1)}}_{FD} \exp(-\frac{(P-P')^2}{2({\varphi^{(2)}}_{FD})^2} - \frac{(T-T')^2}{2({\varphi^{(3)}}_{FD})^2})$ [77], then the size of $\boldsymbol{\varphi_{FD}}$ is (3x1). Similarly, the material damping can be written as:

$$MD(P, \Delta T) = b_1 + b_2 \times P + b_3 \times \Delta T + \varepsilon_{MD} \tag{26}$$

where $\varepsilon_{MD}(\boldsymbol{X}) \sim N(0, k_{MD}([P, \Delta T], [P, \Delta T]', \boldsymbol{\varphi_{MD}})$ is a Gaussian process representing the discrepancy term similar to *FD* above, with $\boldsymbol{\varphi_{MD}}$ a vector of size (3x1). The model discrepancy can also be modeled assuming a linear mean function with respect to the input as

$$\varepsilon_d(P, \Delta T) = c_1 + c_2 \times P + c_3 \times \Delta T + \varepsilon_\varepsilon \tag{27}$$

where $\varepsilon_\varepsilon(\boldsymbol{X}) \sim N(0, k_\varepsilon([P, \Delta T], [P, \Delta T]', \boldsymbol{\varphi_\varepsilon})$ is a Gaussian process representing the discrepancy term

similar to *FD* above, with $\boldsymbol{\varphi}_{\varepsilon}$ a vector of size (3x1).

Finally, the degrading temperature effect on sensors can be accounted for in the observed error standard deviation. Manufacturers typically use a fourth order correction of the observed error for the effect of temperature on the strain [78]. Testing of several trend functions to model the observed error showed that an exponential trend function mimics a fourth-order polynomial best, as shown in Fig. 19. Thus, the use of the exponential trend function instead of a fourth order function reduces the number of calibration parameters. The dependence of the observed error standard deviation on the temperature can be modeled as exponential, and written as

$$\boldsymbol{\sigma}_{\boldsymbol{obs}}(\Delta T) = \boldsymbol{d}_{\boldsymbol{1}} e^{\boldsymbol{d}_{\boldsymbol{2}} \times \Delta T} + \varepsilon_{\sigma} \tag{28}$$

where $\varepsilon_{\sigma}(\boldsymbol{X}) \sim N(0, k_{\sigma}([P, \Delta T], [P, \Delta T]', \boldsymbol{\varphi}_{\sigma}))$ is a Gaussian process representing the discrepancy term similar to *FD* above, with $\boldsymbol{\varphi}_{\sigma}$ a vector of size (3x1).

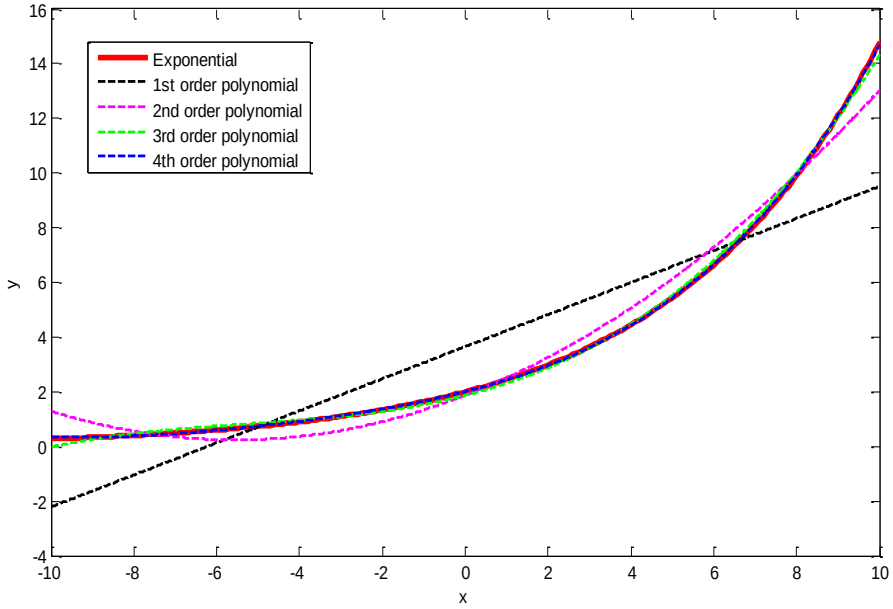

Fig. 19: Comparison of different trend functions

The full Bayesian network associated with this calibration is shown in Fig. 20. The strain output from the model used for the calibration is denoted $\mathbf{Y}$ and the corresponding observation is $\mathbf{Y_{obs}}$. If observations exist at 3 different locations, $\mathbf{Y}$ and $\mathbf{Y_{obs}}$ will be vectors of size (3x1). The parent nodes of *FD* are ε_{FD}, a_1, a_2, a_3, P and ΔT; similarly, the parent nodes of *MD* are ε_{MD}, b_1, b_2, b_3, P and ΔT; the parent nodes of $\boldsymbol{\varepsilon_d}$ are ε_ε, $\boldsymbol{c_1}$, $\boldsymbol{c_2}$, $\boldsymbol{c_3}$, P and ΔT; and the parent nodes of $\boldsymbol{\sigma_{obs}}$ are ε_σ, $\boldsymbol{d_1}$, $\boldsymbol{d_2}$ and ΔT ($\boldsymbol{c_i}$ and $\boldsymbol{d_i}$ nodes are (3x1) vectors each, due to the presence of 3 strain outputs at 3 different locations). The blue arrows reflect the temperature effect in the network. This gives a total of 37 calibration variables.

We can now consider introducing approximations to reduce the number of calibration variables. For example, we may choose to ignore the model discrepancy terms in the input-dependent relations in Eqns. (25)-(28). In that case, ε_{FD}, ε_{MD}, ε_ε, and ε_σ and their parent nodes will be dropped in Fig. 20. The number of calibration variables can therefore be reduced from 37 to 25. As a result, the variance will be increased in the posteriors of the remaining variables to accommodate the uncertainty that would have been explained by ε_{FD}, ε_{MD}, ε_ε and ε_σ. These terms and their parameters (φ_{FD}, φ_{MD}, φ_ε and φ_σ) are shown as red-colored nodes in the full Bayesian network.

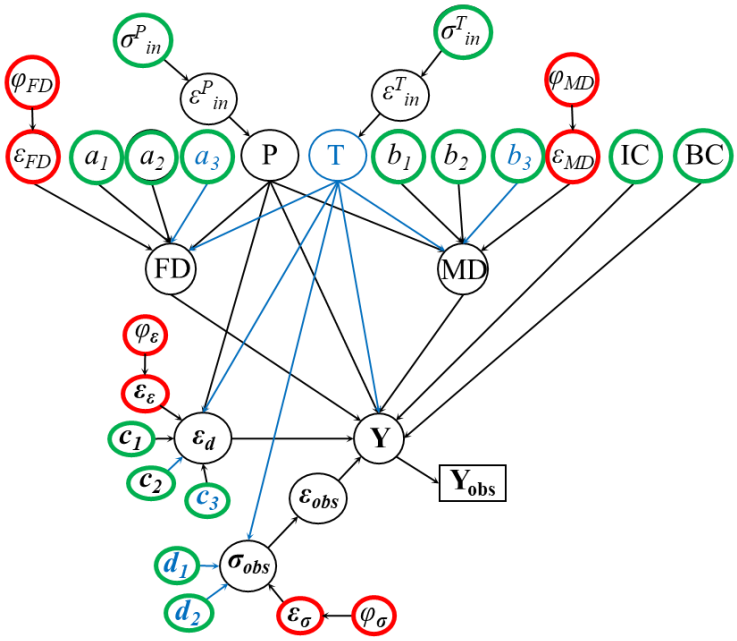

Fig. 20: Full Bayesian network used in calibration

In the absence of physical intuition, we could employ stochastic sensitivity analysis (e.g. using Sobol' indices [79]) to identify calibration parameters that are not significant, fix them at assumed nominal values, and drop them from the Bayesian network. Note that the sensitivity analysis result is affected by the assumption about the prior distributions of the calibration parameters.

4.2.3 Multi-Fidelity Calibration Method

Suppose the same two models are available to predict **Y**: the lower fidelity model $G_1(\boldsymbol{X},\theta_i(\boldsymbol{X}))$ and the higher fidelity model $G_2(\boldsymbol{X},\theta_i(\boldsymbol{X}))$. The multi-fidelity calibration of the previous chapter is extended to incorporate and input-dependence as follows:

i. Define the priors of the hyper-parameters of $\theta_i(\boldsymbol{X})$ and the discrepancy between the LF and HF models $\boldsymbol{D}_{2,1}(\boldsymbol{X})$, denoted $\boldsymbol{\lambda}_{\theta i}$ and $\boldsymbol{\lambda}_{D_{2,1}}$ respectively.

ii. Sample $\boldsymbol{X}$ and $\boldsymbol{\lambda}_{\theta i}$ then calculate $\theta_i(\boldsymbol{X})$.

iii. Run the low-fidelity ($G_1(\boldsymbol{X},\theta_i(\boldsymbol{X}))$) and high-fidelity ($G_2(\boldsymbol{X},\theta_i(\boldsymbol{X}))$) models to obtain N_1 and N_2 sets of outputs, respectively ($N_1 < N_2$ because of computational expense of the HF model).

iv. Build $S_1(\boldsymbol{X},\boldsymbol{\lambda}_{\theta i})$, the surrogate model replacing $G_1(\boldsymbol{X},\theta_i(\boldsymbol{X}))$. In this step, the variance of $\boldsymbol{\varepsilon}_{surr}$ of $S_1(\boldsymbol{X},\boldsymbol{\lambda}_{\theta i})$ is also calculated to account for the surrogate model prediction uncertainty.

v. Using the low-fidelity surrogate model, update the hyper-parameters of $\theta_i(\boldsymbol{X})$ as well as the hyper-parameters of the discrepancy term with the high-fidelity simulation results, i.e., use the relationship

$$\mathbf{Y}_{\mathbf{HF}} = S_1(\boldsymbol{X},\boldsymbol{\lambda}_{\theta i}) + \boldsymbol{\varepsilon}_{surr} + \boldsymbol{D}_{2,1}(\boldsymbol{X}) \tag{29}$$

to compute the posterior distributions of $\boldsymbol{\lambda}_{\theta i}$ and $\boldsymbol{\lambda}_{D_{2,1}}$, denoted as $\boldsymbol{\lambda}'_{\theta i}$ and $\boldsymbol{\lambda}'_{D_{2,1}}$ respectively.

vi. Define the corrected low-fidelity surrogate model with the updated hyper-parameters $\boldsymbol{\lambda}'_{\theta i}$ and $\boldsymbol{D}'_{2,1}(\boldsymbol{X})$ as

$$\text{LFcorr} = S_1(\boldsymbol{X},\boldsymbol{\lambda}'_{\theta i}) + \boldsymbol{\varepsilon}_{surr} + \boldsymbol{D}'_{2,1}(\boldsymbol{X}) \tag{30}$$

Note that $\boldsymbol{D}'_{2,1}(\boldsymbol{X})$ has the same formulation as $\boldsymbol{D}_{2,1}(\boldsymbol{X})$, but is sampled using the posterior

distributions of the hyper-parameters $\boldsymbol{\lambda}'_{D_{2,1}}$, whereas $\boldsymbol{D}_{2,1}(\boldsymbol{X})$ is sampled using the prior distributions $\boldsymbol{\lambda}_{D_{2,1}}$

.

vii. Assume a prior distribution for the model discrepancy term hyper-parameters $\boldsymbol{\lambda}_{\varepsilon_d}$ (i.e., the difference between model prediction and experimental observation) and for the hyper-parameters of the observed error standard deviation $\boldsymbol{\lambda}_{obs}$.

viii. Calibrate the dynamics model hyper-parameters along with the hyper-parameters of $\boldsymbol{\varepsilon}_{\boldsymbol{d}}(\boldsymbol{X})$ with the available experimental data, using the corrected low-fidelity model from step *vi* and the relationship below:

$$\mathbf{Y}_{\mathbf{obs}} + \boldsymbol{\varepsilon}_{obs}(\boldsymbol{X}) = S_1(\boldsymbol{X}, \boldsymbol{\lambda}'_{\theta i}) + \boldsymbol{\varepsilon}_{surr} + \boldsymbol{D}'_{2,1}(\boldsymbol{X}) + \boldsymbol{\varepsilon}_{d}(\boldsymbol{X}) \tag{31}$$

Note that the posteriors of the dynamics model hyper-parameters $\boldsymbol{\lambda}'_{\theta i}$ from step *v* are used as priors here, in order to compute updated hyper-parameters $\boldsymbol{\lambda}''_{\theta i}$, the updated model discrepancy hyper-parameters $\boldsymbol{\lambda}'_{\varepsilon_d}$ and the updated observed error hyper-parameters $\boldsymbol{\lambda}'_{obs}$. However, $\boldsymbol{\varepsilon}_{surr}$ and $\boldsymbol{\lambda}'_{D_{2,1}}$ are fixed in this step based on the results of step *iv* and step *v* respectively.

4.3 Numerical Example

4.3.1 Problem Description

The example problem is the simplified representation of an aircraft fuselage panel used in Chapter 3. In addition to the dynamic acoustic loading (*P*), high temperature loads (*T*) are added in this chapter. In the experiment, the temperature load is generated by a heat laser beam aimed at the center of the panel,

thus creating a non-uniform distribution of the load (as seen in Fig. 21 below).

The aim is to calibrate the damping properties of the panel as functions of temperature (70, 120 and 180 °F). An important concern in the calibration exercise is to account for the nonlinear behavior of the panel. Details about the experimental setup can be found in Section 3.3.1An infrared camera takes pictures of the heated panel during the experiment, and the pixelated data is transformed into a temperature load throughout the panel in the FEA model, as shown in Fig. 21.

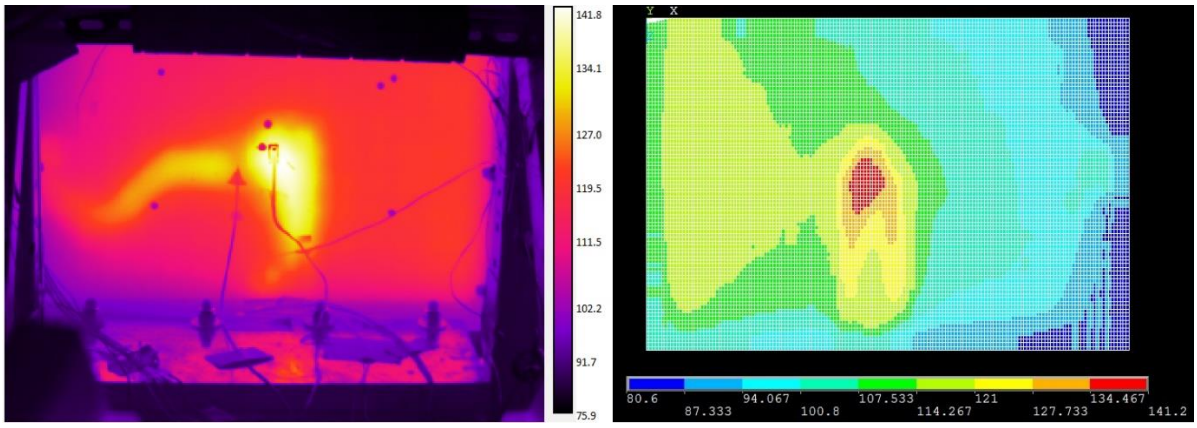

Fig. 21: Temperature distribution in experimental setup (left) and ANSYS model (right)

Two models of different fidelities are considered:

- Model 1 consists of a power spectral density analysis, which involves a linear combination of mode shape effects (referred to as low-fidelity model - LF). The acoustic load applied is the Welch power spectral density (PSD) [70] of the experimental 160, 166, 172 and 178 dB acoustic load. The temperature load is applied as a constant heat on the elements as shown in Fig. 21. The PSD is calculated with the entire signal, for the full duration of sixty seconds. The output of Model 1 is a strain PSD curve. The strain RMS is calculated and used for comparison with the

experimental data. This simulation is considered a lower-fidelity approximation of the experiment because the PSD input is not unique to the signal it is calculated from, since the phase component is ignored. In addition, the analysis being a linear modal combination, geometric non-linearity is not considered in the PSD analysis.

- Model 2 is a full transient analysis where the acoustic loading is applied as a dynamic time history input (referred to as high-fidelity model - HF). The temperature load is also applied as a constant heat on the elements as shown in Fig. 21. The output is a strain signal also converted to a PSD curve, and the strain RMS is derived from it. The model run is quite time-consuming, allowing only 0.2 seconds of the input signal (of the full 60 seconds of data available) to be simulated with the available computational resources. In this model, geometric non-linearity is considered by including the effect of large deflections and rotations in the strain calculations.

Both models have the same mesh size and consider a non-linear stress-strain relationship (material non-linearity), as shown in Fig. 22. No transient heat analysis is done since the acoustic loading was only applied after the heat image became steady. The inclusion of material and geometric non-linearity in the modeling phase allows us to investigate whether input-dependence of the calibration parameter should be considered in addition to non-linearity.

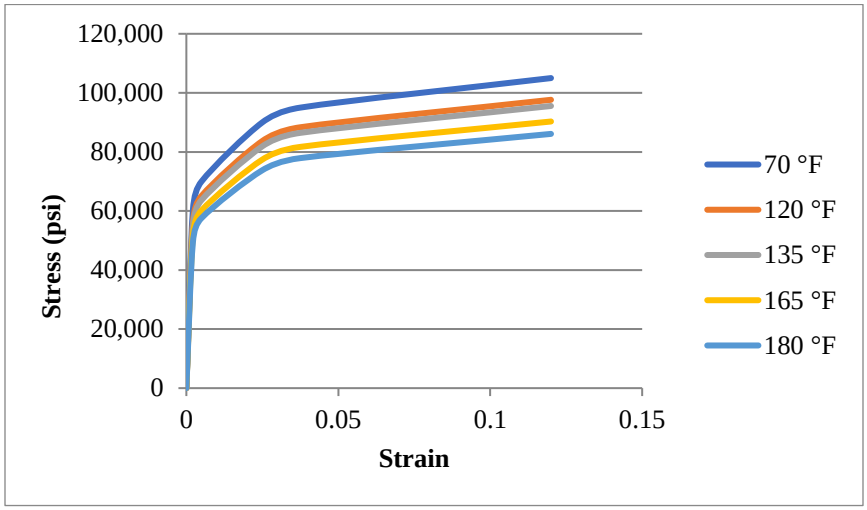

Fig. 22: Non-linear stress-strain relationship

Two types of damping are considered here, as discussed in Section 3.3.1, namely frictional damping (*FD*) at the bolts for a width of 1" around the perimeter of the panel (the edge of the plate is sandwiched between two 1" wide metal strips, and bolted to the test frame, as shown in Fig. 5) and material damping (*MD*) throughout the remainder of the panel. *FD* is modeled as a linear function of the acoustic loading *P* and the differential temperature $\Delta T = T - 70$ as defined in Eq. (25) (the room temperature is 70 °F and no thermal stress is incurred at that temperature). *MD* is also modeled as a linear function of the acoustic loading and the differential temperature ΔT as defined in Eq. (26).

The boundary condition and the initial conditions are also calibration variables, as defined in Chapter 3.

The model discrepancy is modeled here assuming a linear mean function with respect to the input as defined in Eq. (27). The discrepancy term is specific to the locations of the strain gages considered, thus $\boldsymbol{c}_1, \boldsymbol{c}_2$ and $\boldsymbol{c}_3$ are considered (3x1) vectors for the three strain gage locations used in the calibration.

Finally, it can be seen by superposing Fig. 5 and Fig. 21 that the strain gages see different temperatures under the same temperature loading, thus are affected differently by the same input. We account for the degrading temperature effect in the observed error standard deviation as defined in Eq. (28). $\boldsymbol{d_1}$ and $\boldsymbol{d_2}$ are considered (3x1) vectors for the three strain gage locations used in the calibration.

The full Bayesian network would contain 37 calibration variables ($\boldsymbol{\varphi_{FD}}$, $\boldsymbol{\varphi_{MD}}$, $\boldsymbol{\varphi_{\varepsilon}}$ and $\boldsymbol{\varphi_{\varepsilon}}$ are (3x1) vectors each as defined in Section 4.2.2). By simplifying the Bayesian network to ignore model discrepancy in the input-dependence relations (i.e., $\varepsilon_{FD} = \varepsilon_{MD} = \varepsilon_{\varepsilon} = \varepsilon_{\sigma} = 0$), the number of calibration variables is reduced to 25.

4.3.2 Results

The priors for the structural parameters and hyper-parameters are listed in Table 3. The priors of the errors' parameters and hyper-parameters are listed in Table 4. The same priors are assumed for the parameters at all strain gage locations. The low-fidelity surrogate model used in the calibration is a second-order polynomial chaos expansion model, built with 100 training points sampled using an Optimum Symmetric Latin Hypercube (OSLH) sampling technique [80]. 17 high-fidelity runs were done, also sampled using OSLH. These high-fidelity runs are used to correct the low-fidelity surrogate model in step *v.* of the methodology detailed in Section 4.2.1. For comparison purposes, a high-fidelity surrogate model for the high-fidelity calibration with experimental data is also built with these 17 training points, and is a first-order polynomial chaos expansion model (the low number of training points does not allow building a higher order PCE, as discussed in Section 2.4).

Table 3: Priors of structural calibration parameters (1/2)

Relationship	$FD = a_1 + a_2 \times P + a_3 \times \Delta T$			$MD = b_1 + b_2 \times P + b_3 \times \Delta T$				
Variable	a_1	a_2	a_3	b_1	b_2	b_3	*IC*	*FR*
Distribution type	*Uniform*	*Uniform*	*Uniform*	*Uniform*	*Uniform*	*Uniform*	*Uniform*	*Uniform*
Distribution parameters	$[10^{-8}, 6.10^{-5}]$	$[10^{-6}, 10^{-4}]$	$[0, 10^{-3}]$	$[5.10^{-10}, 6.10^{-7}]$	$[5.10^{-8}, 5.10^{-7}]$	$[0, 10^{-5}]$	$[10^{-6}, 10^{-4}]$	*[0.5,1]*

Table 4: Priors of error calibration parameters (2/2)

Relationship	$\varepsilon_d = c_1 \times P + c_2 \times \Delta T + c_3$					$\sigma_{obs} = d_1 e^{d_2 \times \Delta T}$	
Variable	c_1	c_2	c_3	ε_{in}	σ_{in}	d_1	d_2
Distribution type	*Uniform*	*Uniform*	*Uniform*	*Normal*	*Uniform*	*Uniform*	*Uniform*
Distribution parameters	$[-7.10^{-4}, 7.10^{-4}]$	$[-10^{-4}, 10^{-4}]$	$[-5.10^{-5}, 5.10^{-5}]$	$[0, \sigma_{in}]$	*[0, 1.5]*	$[10^{-8}, 10^{-2}]$	*[0,1]*

**Note: Distribution parameters refers to the lower and upper bounds for the uniform distribution, and mean and standard deviation for the normal distribution*

Only one set of experimental data is available per load setting (one observation at each strain gage location for each combination of acoustic loading *P* and temperature loading *T*). Since the three strain gage outputs (SG1, SG2 and SG4) are used for calibration (i.e., $n = 3$ per load combination, with respect to Eqns. (7) and (8)), the fourth one (SG5) is used to compute the Bayes factor (likelihood ratio) to compare the results of the different calibration options with experimental data. The three remaining strain gages (SG3a, SG3b, SG3c - out of the total seven placed on the plate) were discarded because the values recorded were very low compared to the rest of the strain gages, and failures were noted for the 180 °F temperature loading.

A sensitivity analysis of the low-fidelity and high-fidelity surrogate models using the first order Sobol' index [79] showed that the strain output is more sensitive to the frictional damping parameters (a_1, a_2, a_3) in the high-fidelity model compared to the low-fidelity model, whereas the strain output is more sensitive to the material damping parameters (b_1, b_2, b_3) in the low-fidelity model compared to the high-fidelity model. The ratios HF/LF first order Sobol' index are displayed in Table 5.

Table 5: HF/LF ratios of first-order Sobol' index from the corresponding surrogate models

	HF/LF	*SG1*	*SG2*	*SG4*
FD	a_1	*1.78*	*6.42*	*1.92*
	a_2	*2.47*	*8.90*	*1.33*
	a_3	*12.53*	*45.07*	*6.74*
MD	b_1	*0.55*	*0.98*	*0.29*
	b_2	*0.74*	*0.89*	*0.40*
	b_3	*0.15*	*0.54*	*0.08*

The posteriors for the calibration variables were obtained using slice sampling MCMC. The sampling uses a burn-in of 1,000 samples. After burn-in, 8,000 samples of the posteriors are retained. The posterior distributions were found to become stable after about 7,500 samples. The average acceptance rate (excluding the burin-in samples) was 61%. The posterior distributions for frictional damping (Fig. 23) and material damping (Fig. 24) are shown for the calibration using only the low-fidelity model, only the high-fidelity model, and the corrected low-fidelity model calibrated with experimental data. The intermediate step in the corrected low-fidelity model, where the low-fidelity model is corrected with high-fidelity simulations (LF_HF), is also shown to indicate the stronger priors. The priors in the LF, HF and LF_HF are all uniform, whereas the priors in LFcorr are the posteriors obtained in LF_HF. Fig. 25 shows the posterior distributions for the model discrepancy at SG1, for illustration. The model

discrepancy posteriors at SG2 and SG4 are similar; they are not shown for brevity. Lastly, the posteriors for the observed error standard deviation σ_{obs} at SG1 and SG2 are shown in Figs. 26 and 27 respectively. Note that SG2 is at a location that sees a higher temperature than SG1 for the same load input.

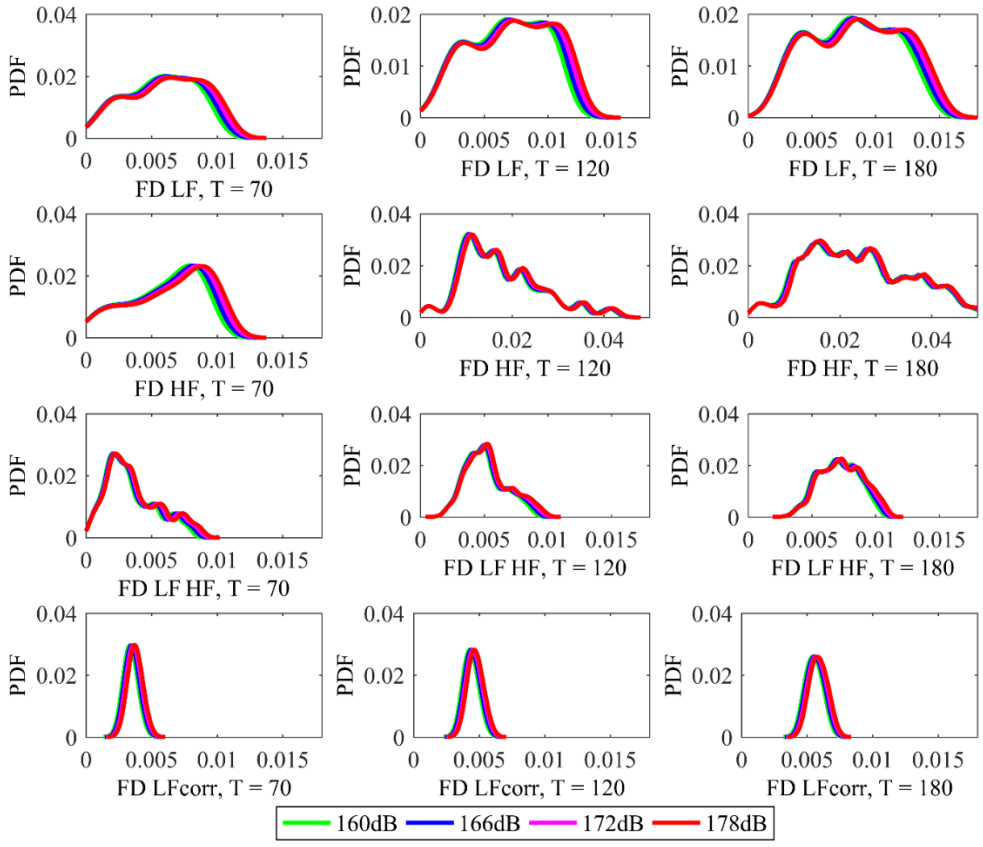

Fig. 23: Posteriors of frictional damping (FD) using LF, HF, LF_HF and LFcorr
**Note the difference in range of X axis between FD HF T=120℉, T=180℉ and the rest of the subplots. This is due to the large uncertainty in these subplots compared to the rest (see explanation in Section 4.3.3).*

Fig. 23 shows that the posterior of the frictional damping obtained using the model from the multi-fidelity calibration method has much lower uncertainty than the posteriors using all other models. The

posterior using the corrected low-fidelity model also converges near the maximum a posteriori (MAP) estimate of the posterior coming from the calibration using the high-fidelity model. This is expected, knowing that the strain output in the high-fidelity model is more sensitive to frictional damping than the strain coming from the low-fidelity model. Also, the influence of the acoustic load on the posterior distributions is much lower than the influence of the temperature.

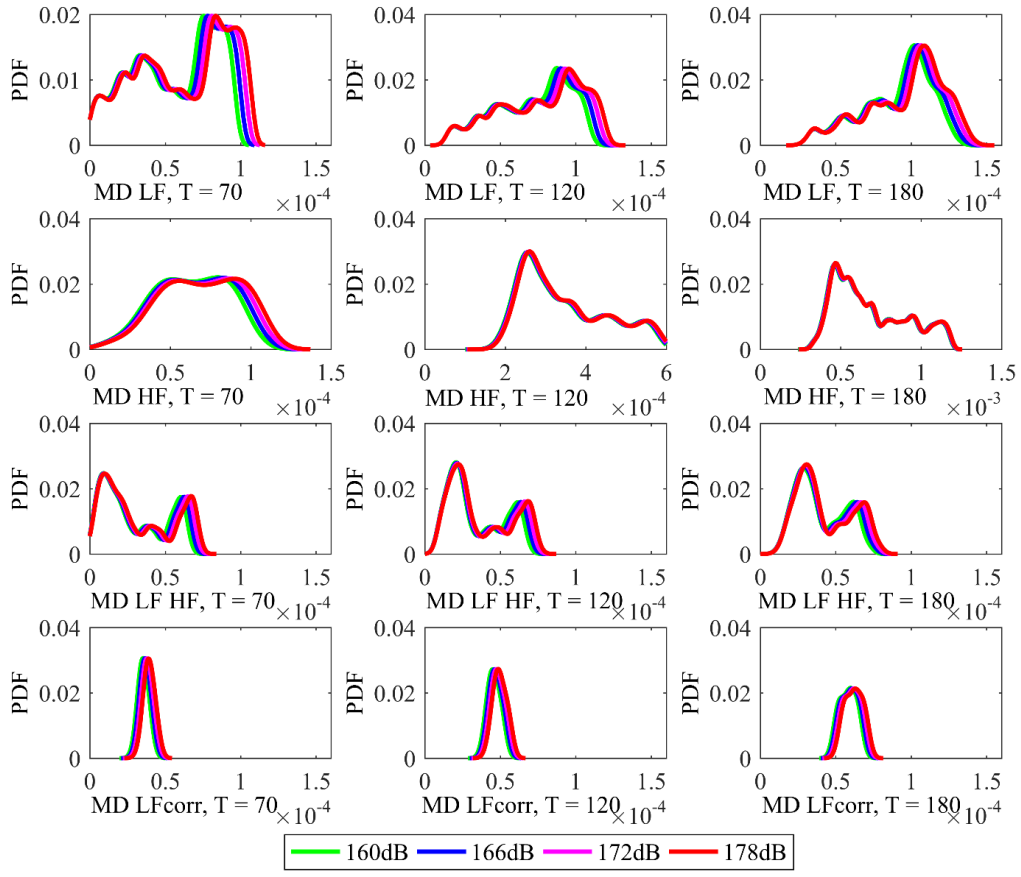

Fig. 24: Posteriors of material damping (MD) using LF, HF, LF_HF and LFcorr
** Note the difference in range of X axis between MD HF T=70 ℉, T = 120 ℉, T=180 ℉ and the rest of the subplots. This is due to the large uncertainty in these subplots compared to the rest (see explanation in Section 4.3.3).*

Fig. 24 shows that the posterior of the material damping obtained using the model from the multi-fidelity calibration method has much lower uncertainty than the posteriors using all other models. The posterior using the corrected low-fidelity model also converges near the MAP estimate of the posterior coming from the calibration using the low-fidelity model. This is expected, knowing that the strain output in the high-fidelity model is more sensitive to frictional damping than the strain coming from the low-fidelity model. Also, the influence of the acoustic load on the posterior distributions is much lower than the influence of the temperature.

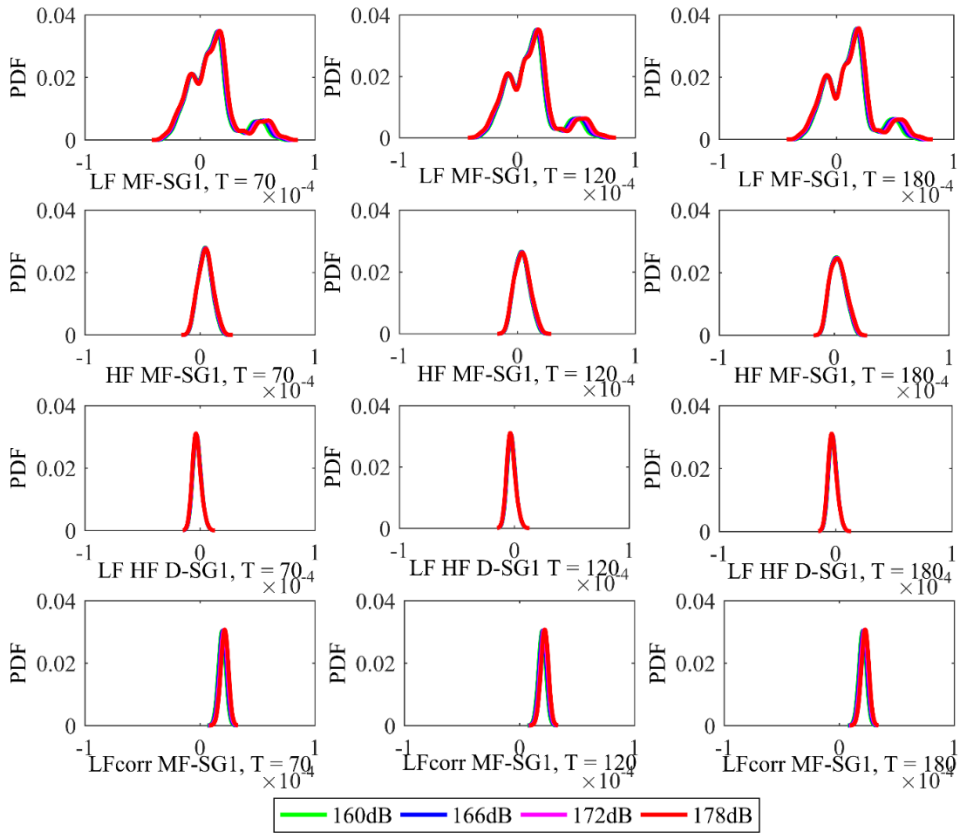

Fig. 25: Posteriors of model form error (MF) at SG1 (for illustration) using LF and HF, discrepancy (D) between LF and HF models (LF HF), and model form error (MF) using LFcorr

Fig. 25 shows the model form error posteriors as a function of acoustic load and temperature. We can see that the posterior distribution from the low-fidelity model shows high uncertainty with respect to posteriors from the other models. In these results, we also see that changes in the acoustic load and temperature inputs have low influence on the posterior distributions of model form error.

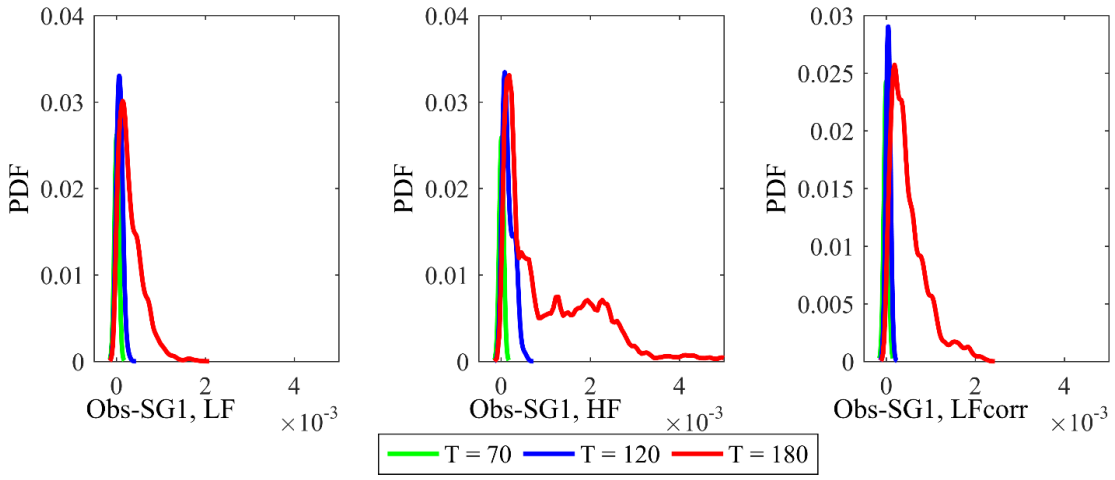

Fig. 26: Posteriors of observed error standard deviation σ_{obs} at SG1 using LF, HF and LFcorr
**There is no observed error in the correction of LF with HF simulations (LF_HF), no experimental data is used*

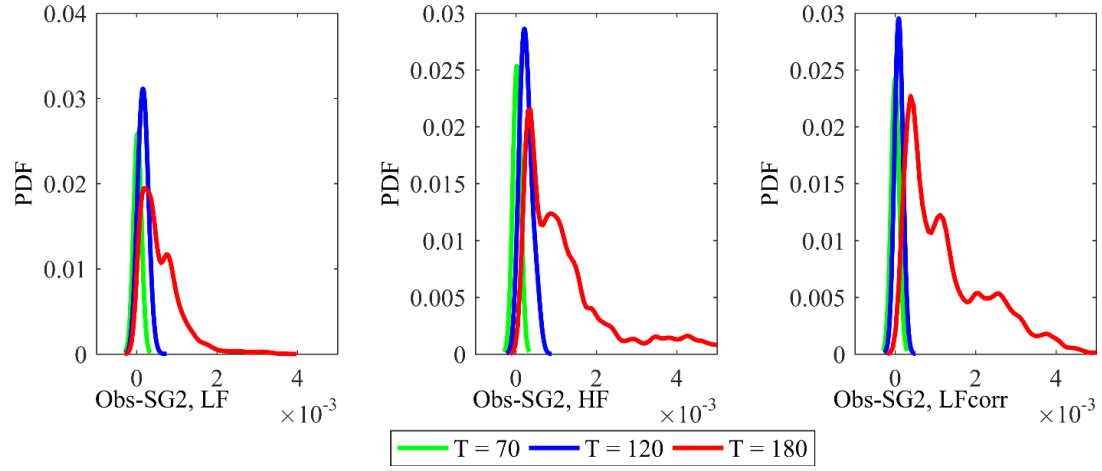

Fig. 27: Posteriors of observed error standard deviation σ_{obs} at SG2 using LF, HF, and LFcorr
**There is no observed error in the correction of LF with HF simulations (LF_HF), no experimental data is used*

Figs. 26 and 27 show the posteriors of the observation error standard deviation at 2 different locations of the strain gage: SG1 and SG2. We see comparable posteriors in the low-fidelity, high-fidelity and corrected low-fidelity models used, which is to be expected knowing that the model used does not influence the true value of the observed error. In addition, note that the posterior distributions at SG2 have higher MAP estimates and uncertainty compared to SG1 at higher temperatures. This is due to non-uniform temperature distribution on the panel, as shown in Fig. 21.

A predictive check was performed with posteriors at the three sensor locations SG1, SG2 and SG4. Fig. 28 shows the results for 2 load combinations for illustration: Comb. 1 (T = 70 °F, P = 160 dB) and Comb. 2 (T = 180 °F, P = 172 dB). The other load combinations show the same results, and are omitted for brevity. This demonstrates that the sensor data lies within the posterior predictions.

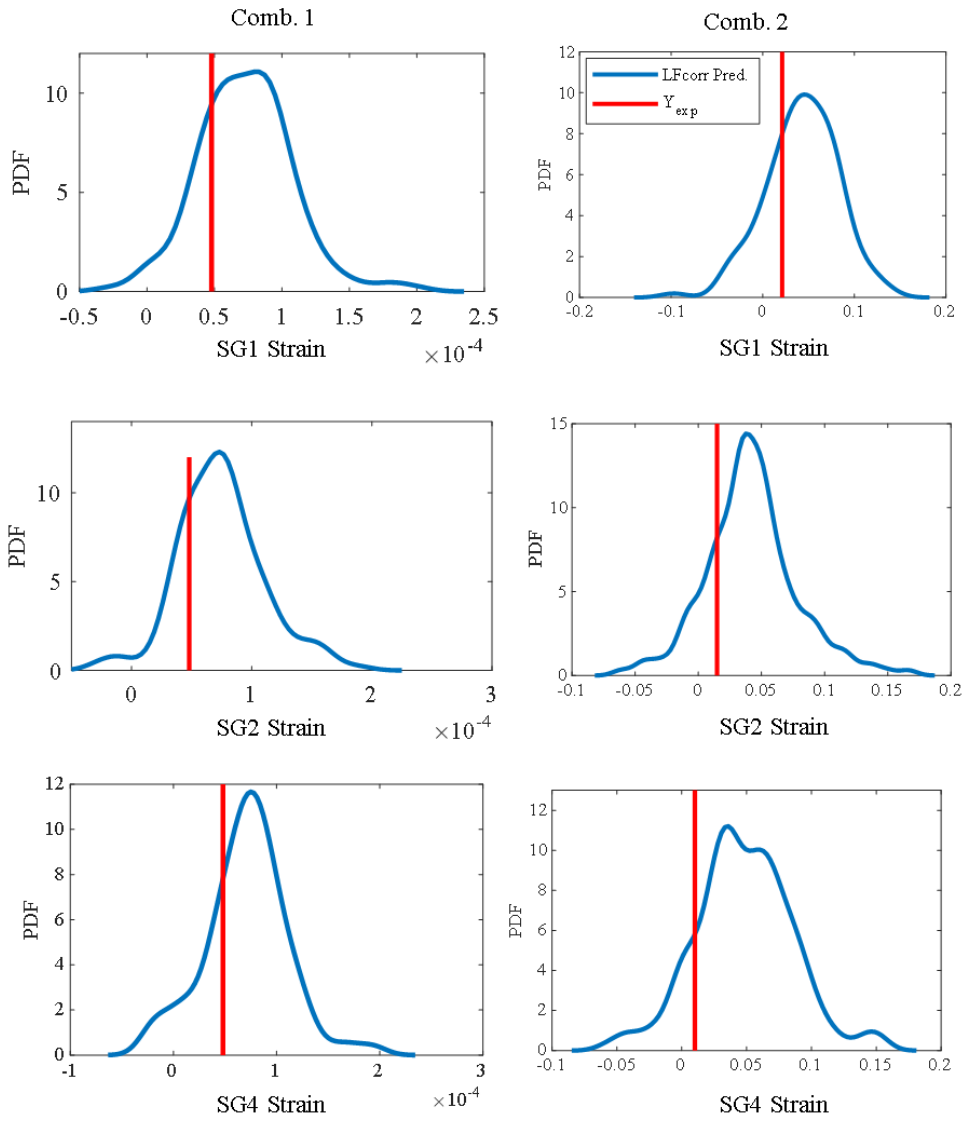

Fig. 28: Predictive check of corrected low-fidelity surrogate model

Using the observations at the fourth strain gage (SG5), the Bayes factors (described in Section 2.6) among the three calibration options (calibration with low-fidelity surrogate, calibration with high-fidelity surrogate and calibration with corrected low-fidelity surrogate) were computed as functions of the

temperature and acoustic loading as LF : HF : LFcorr, and displayed in Table 6.

Table 6: Bayes Factor

LF : HF : LFcorr	*160dB*	*166 dB*	*172 dB*	*178 dB*
70 °F	*1 : 0.85 : 1.13*	*1 : 0.86 : 1.53*	*1 : 0.85 : 1.45*	*1 : 0.91 : 1.51*
120 °F	*1 : 0.56 : 1.08*	*1 : 0.58 : 1.18*	*1 : 0.38 : 1.11*	*1 : 0.34 : 1.17*
180 °F	*1 : 0.04 : 1.00*	*1 : 0.085 : 1.00*	*1 : 0.23 : 1.34*	*1: 282.19 : 1167.61*

This indicates superior performance of the multi-fidelity calibration in predicting the response at the fourth strain gage compared to the individual low-fidelity and high-fidelity calibrations, especially at higher temperature and higher acoustic loading, when the behavior is highly nonlinear.

4.3.3 Discussion

The results displayed in Chapter 3 can be considered a subset of those in Chapter 4. If the input settings in Section 4.3.2 are set to T = 70°F (ambient temperature) and P = 140dB (lowest acoustic loading), the posteriors of the calibration quantities mirror the results in Section 3.3.2. This shows that, although the total number of calibration quantities increased in order to consider temperature effects on the damping and to include nonlinear effects of the temperature on the structure, the results are consistent with the simpler linear case studied in the previous chapter.

The results in Figs. 23 and 24 show that after accounting for geometric and material nonlinearity in the corrected low-fidelity model, the effect of the acoustic loading input on the calibration parameters is negligible. However, when temperature is added, the effect of the input gets pronounced; temperature affects the material properties, the presence of geometric and material nonlinearity, the model discrepancy, as well as the errors in the strain gages themselves. All these considerations are included in the calibration process, and the results in Figs. 23 - 27 clearly show the effect of temperature on the

calibration parameters.

More importantly, it is seen that the temperature effect on the material properties is larger than that of the acoustic loading. For example, looking at the posteriors in Fig. 23, there is an almost 50% increase in the maximum a posteriori (MAP estimate) of frictional damping from 4.10^{-3} at 70 °F to 6.10^{-3} at 180 °F in the final multi-fidelity calibration results. The same goes for the material damping in Fig. 24; increase of almost 20% from $4.5.10^{-5}$ at 70 °F to $5.5.10^{-5}$ at 180 °F. This result accentuates the need to use nonlinear analyses under high temperature loading. In the posteriors resulting from calibrations with low or high-fidelity models alone, although we see a general increasing trend of the damping with respect to temperature in Figs. 23 and 24, we also notice the high uncertainty present (wide posteriors). This hinders the ability to make definite conclusions in the effect of temperature on the damping using those models compared to the clear effect seen with LFcorr. This demonstrates the importance of fusing information from models of different fidelity in the calibration of system parameters, and the value of the proposed methodology.

The most significant temperature effect noticeable in the results is the effect of temperature on strain gage performance. Figs. 26 and 27 individually show an increase in the uncertainty of σ_{obs} for SG1 and SG2 at higher temperature inputs (120 °F and 180 °F). In addition, comparing Figs. 26 and 27, it is seen that the MAP estimate of σ_{obs} at SG2 is higher than at SG1. This is because SG2 is closer to the center of the heat laser compared to SG1 and sees higher temperatures under the same loading condition. The inclusion of the temperature effect on the strain gages in the calibration of damping provides an implicit "weighting" of specific strain gages in the calibration process; the higher the σ_{obs} at some location, the higher the uncertainty in the data and therefore the higher the uncertainty in the calibration result. This

implies that at higher temperatures, when the observed error is higher at SG2 than SG1, the strain measurement at SG1 is more useful for calibration, since it produces less uncertainty in the calibration result.

Most notably, this numerical example illustrates a systematic approach to Bayesian model calibration in the presence of geometric and material nonlinearity, which allows the investigation of the temperature and acoustic loading effects on frictional damping, material damping, discrepancy between low and high-fidelity models, model form error between the models and experiments, and the observed error.

4.4 Conclusion

This chapter investigated a multi-fidelity approach for the Bayesian calibration of model parameters, accounting for geometric and material nonlinearity effects, and input-dependence on model parameters and observations data.

The effect of the input on the analysis, model parameters and the measurement errors was considered. We differentiated between geometric nonlinearity, material nonlinearity and parameter nonlinearity in the calibration process. Functional relationships were assumed to account for the input-dependence (i.e. parameter nonlinearity), and the hyperparameters of these relationships were calibrated. The results showed a clear influence of the temperature on the damping-related parameters, as well as the strain gage measurement errors.

The next two chapters consider improvements in both the modeling and experimental directions. In the modeling direction, the training runs of the original physics model for building the surrogate model need to be selected optimally for two reasons: (1) to minimize the low-fidelity surrogate model error, and (2) to retain as much information as possible from all models, especially the higher fidelity

simulations, for which the number of simulations is small. In the experimental direction, since the strain gages are affected differently in the presence of non-uniform temperature loading, and the measurement errors in turn affect the posterior distributions, it is important to optimize the sensor locations in order to maximize the information gain in the calibration process.

Chapter 5

Simulation Resource Optimization for Multi-Fidelity Model Calibration

In this chapter, the low-fidelity surrogate model correction within the multi-fidelity approach developed is optimized to maximize information gain while reducing the computational expense. The high-fidelity simulation points are sequentially selected to maximize the KL divergence (thus information gain) between the joint priors and joint posteriors of the calibration parameters.

5.1 Introduction

In the previous two chapters, we have proposed fusing information from models of different fidelity to calibrate system parameters. We used high fidelity simulations to correct a lower fidelity surrogate model used in the multi-fidelity Bayesian calibration. The high-fidelity model runs were sampled using a general optimum symmetric Latin hypercube (OSLH) method. Although using an OSLH sampling technique spreads high-fidelity simulation points to optimally cover the sampling space, it does not guarantee the maximization of information retention in the multi-fidelity calibration method. In this chapter, we propose a novel method for sequentially picking high-fidelity simulation points that maximize information gain in the calibration of system parameters.

Many methods exist for selecting the inputs of the original model runs to train the surrogate model, and historically, space-filling methods have been used, including simple random sampling, full factorial design [81], Latin hypercube [80, 82], etc. When the underlying function of the model has a constant variance throughout the domain, it is necessary and efficient to use a space-filling sampling algorithm. These methods include, among others, Halton sequence sampling [83], Hammersley sequence sampling

[84] and Sobol sequence sampling [85]. However, when the variation of the function is localized, space-filling sampling is then inefficient, especially when resources are scarce. Since the location of the optimum high-fidelity points cannot be known a priori, a sequential sample selection can be used. Some local approximation methods were developed by Myers and Montgomery [86] for polynomial response surfaces where the optimization starts in a sub-region of the full space and proceeds using a trust region strategy. Although these methods have guaranteed convergence, they can get stuck at local minima. In contrast, global approximation methods aim to capture the global trends of the model over the full design space. Typically, studies have focused on minimizing the variance of the outputs as the optimization objective. MacKay [87] and Tong [88] used a Bayesian learning framework in an entropy-based sample selection to minimize uncertainty in the prediction. Bichon et al [89] built a Gaussian process surrogate model using a small number of samples, then adaptively added subsequent samples minimizing the model error to correctly approximate the reliability limit state. In contrast to minimizing variance, Hombal and Mahadevan [90] proposed selecting training points that focus on minimizing the bias in the prediction. Most studies on the selection of training points for building surrogate models have focused on prediction rather than calibration and consider the case when a single model is available and is expensive.

When models of different fidelity are available, training points selection for both low and high-fidelity models is typically done with the purpose of filling the variables' space. Goh [91] uses Latin hypercube sampling for all models. Le Gratier & Garnier [92] use a nested space-filling design to pick simulation points where low-fidelity and high-fidelity points are generated independently and the low-fidelity training points nearest to the high-fidelity points are discarded. Balabanov et al. [93] start by generating low-fidelity training points, then select a subset of these for high-fidelity runs using D-optimality

criterion. It is possible to also start with the high-fidelity training points and pick the low-fidelity superset using some optimization criterion.

The methods mentioned above are developed for the purpose of building and/or combining multi-fidelity surrogate models for prediction. The focus of this chapter is on selecting training points to build a surrogate model that can be used in calibration. Since the low-fidelity model is very fast, we can use a space filling sampling technique to build a low-fidelity surrogate model. However, it is unaffordable to select many high-fidelity training points. We propose starting with a small number of high-fidelity simulation runs that correct the low-fidelity surrogate, then select the additional high-fidelity runs that maximize the information gain in the corrected low-fidelity surrogate. For this purpose, we use synthetic high-fidelity data to further correct the low-fidelity surrogate model, and choose the high-fidelity input that maximizes the KL divergence between the joint prior and joint posterior parameter distributions. We measure the information gain in the correction by comparing the joint posterior distribution to the joint prior distribution and computing expected value of the KL divergence. We pick the subsequent high-fidelity runs that maximize the KL divergence between the joint prior and posterior until convergence. The methodology is applied to the curved panel problem considered in the previous chapters.

5.2 Optimization formulation

The optimized selection of high-fidelity inputs within multi-fidelity calibration can be introduced in step *vi* of the multi-fidelity calibration algorithm in Section 4.2.3. The optimization objective is to select the high-fidelity runs at the input values that maximize the KL divergence between the joint prior and the joint posterior distributions of quantities involved in the correction of the low-fidelity surrogate using

high-fidelity physics simulations. Because there is no prior information regarding the optimal location of the high-fidelity simulations, we start with a small number of high-fidelity simulations to correct the low-fidelity surrogate in step *v*. We consider the corrected joint distributions from this step as a prior joint distribution before the optimization. Because the high-fidelity simulations are expensive, we generate synthetic high-fidelity data ($\mathbf{Y}_{HF^S}$) using the corrected low-fidelity model from step *vi* with noise added to it. $\mathbf{Y}_{HF^S}$ is used to "correct" the low-fidelity surrogate model and the joint posterior is compared to the joint prior from the initial step using the KL divergence. The input to the synthetic high-fidelity model that yields the highest expected value of the KL divergence is selected to be run in the original high-fidelity physics model. The output from the selected run is then added to the initial high-fidelity data. The joint posterior distribution from the new set of high-fidelity simulations is now the prior joint distribution to the new optimization set. Step *vi* of the multi-fidelity calibration method becomes as follows:

vi. Define the corrected low-fidelity surrogate with the updated hyper-parameters $\boldsymbol{\lambda}_{\theta i}^{'}$ and $\boldsymbol{D}_{2,1}^{'}(\boldsymbol{X})$ as

$$\text{LFcorr} = S_1(\boldsymbol{X}, \boldsymbol{\lambda}_{\theta i}^{'}) + \boldsymbol{\varepsilon}_{surr} + \boldsymbol{D}_{2,1}^{'}(\boldsymbol{X}) \tag{32}$$

Note that $\boldsymbol{D}_{2,1}^{'}(\boldsymbol{X})$ has the same functional form as $\boldsymbol{D}_{2,1}(\boldsymbol{X})$, but is sampled using the posteriors of the hyper-parameters $\boldsymbol{\lambda}_{D_{2,1}}^{'}$. $\boldsymbol{D}_{2,1}(\boldsymbol{X})$ is sampled using the priors $\boldsymbol{\lambda}_{D_{2,1}}$.

a. Define a synthetic high-fidelity model HF^S as:

$$\text{HF}^S = \text{LFcorr} + noise = S_1(\boldsymbol{X}, \boldsymbol{\lambda}_{\theta i}^{'}) + \boldsymbol{\varepsilon}_{surr} + \boldsymbol{D}_{2,1}^{'}(\boldsymbol{X}) + N(0, \boldsymbol{\sigma}_{noise}) \tag{33}$$

b. Correct LFcorr using $\mathbf{Y}_{HF^S}$:

$$[\mathbf{Y}_{HF}, \mathbf{Y}_{HF^S}] = S_1(\boldsymbol{X}, \boldsymbol{\lambda}_{\theta i}) + \boldsymbol{\varepsilon}_{surr} + \boldsymbol{D}_{2,1}(\boldsymbol{X}) \tag{34}$$

to compute $\pi(\boldsymbol{\lambda}_{\theta i}, \boldsymbol{D}_{2,1}|\mathbf{Y}_{HF^S})$

c. Calculate the KL divergence $KLD(\pi(\boldsymbol{\lambda}_{\theta i}, \boldsymbol{D}_{2,1}|\mathbf{Y}_{HF}) \,||\, \pi(\boldsymbol{\lambda}_{\theta i}, \boldsymbol{D}_{2,1}|\mathbf{Y}_{HF^S}))$

d. Repeat steps a through c to find $\boldsymbol{\lambda}_{\theta i}^{opt}$ that maximizes the expected KL divergence.

e. Run the high-fidelity model at $\boldsymbol{\lambda}_{\theta i}^{opt}$ and update $\mathbf{Y}_{HF}$ accordingly.

f. Repeat steps *a* through *e* until convergence.

Step *vi* can be formulated as an optimization problem in the following manner:

$$\begin{aligned} &\max_{\lambda_{\theta i}, \lambda_{D_{2,1}}} KLD(\pi(\boldsymbol{\lambda}_{\theta i}, \boldsymbol{\lambda}_{D_{2,1}} | \mathbf{Y}_{HF}) \,||\, \pi(\boldsymbol{\lambda}_{\theta i}, \boldsymbol{\lambda}_{D_{2,1}} | \mathbf{Y}_{HF^S})) \\ &s.t.\ \boldsymbol{\lambda}_{\theta i} \in \pi(\boldsymbol{\lambda}_{\theta i}) \\ &\quad \boldsymbol{\lambda}_{D_{2,1}} \in \pi(\boldsymbol{\lambda}_{D_{2,1}}) \end{aligned} \tag{35}$$

In this section, we used MATLAB's [94] built-in *fmincon* function to solve the optimization. *fmincon* finds the minimum of a constrained non-linear multivariate function using the interior-point algorithm method [95], which aims to solves a sequence of approximate minimization problems. There are several user-determined values in this proposed method that influence the outcome. The first is the amount of noise added in step *a*. A small noise level might force some local minima to be picked in every iteration. A large noise will slow down the calibration substantially and could result in a synthetic high-fidelity model that might not agree with the high-fidelity physics simulations. Care is needed in determining a reasonable amount of noise to allow the optimization to run smoothly. Another user-determined value is

the convergence criterion in step *f*. For illustration of the methodology in the numerical example, convergence was assumed to be reached when the KL divergence in two consecutive optimization iterations between the optimized posterior and the posterior using the initial high-fidelity points is negligible (i.e. no more additional information is incorporated in the calibration).

5.3 Numerical Example

5.3.1 Problem Description

The example problem is the same as the one used in Chapter 4, and is a simplified representation of an aircraft fuselage panel subjected to dynamic acoustic loading (*P*) and high temperature loads (*T*). The same assumptions on the high and low-fidelity models are used, and the same calibration variables as in Chapter 4 are considered. The low-fidelity surrogate model is a second-order polynomial chaos expansion model, built with 100 training points sampled using an OSLH sampling technique.

Previously, the low-fidelity surrogate model was corrected using 20 high-fidelity simulations, obtained by running an OSLH on the full design space. In this chapter, we start with 4 high-fidelity points sampled using OSLH and add subsequent high-fidelity simulations resulting from the optimization until the posteriors from two subsequent optimizations are similar. The minimum number of high-fidelity simulations for our problem is three, one at each temperature setting (70, 120 and 180 °F), since the calibration parameters are functions of temperature.

5.3.2 Results

In Figs. 29-32, Post.20 denotes the posterior obtained from the correction with 20 high-fidelity simulations, sampled using the space-filling OSLH sampling technique. Post.4 denotes the initial

posterior of the parameters using outputs from 4 OSLH high-fidelity in the correction. The synthetic high-fidelity model at the following step consists of the corrected low-fidelity model using Post.4, in addition to a noise term. This synthetic high-fidelity model is used in the optimization framework to pick the new high-fidelity point that maximizes the KL divergence. At each subsequent iteration, Post.i denotes the posterior obtained using the initial 4 OSLH high-fidelity points plus the (i-4) subsequent high-fidelity outputs from the optimized inputs.

As a benchmark, we also correct the low-fidelity surrogate in one step using all the high-fidelity outputs available (the high-fidelity simulation outputs from the optimization, 20 high-fidelity runs sampled using OSLH for comparison and previous high-fidelity outputs from the same model used in other exercises, a total of 46 simulations – denoted as Post. 46).

The KL divergence is calculated using the joint distributions of all the correction variables: structural parameters/hyper-parameters and error hyper-parameters. Optimization convergence is reached when the difference between two consecutive joint posteriors is negligible, i.e. the difference between two consecutive expected values of the KL divergence is very small (no more information gain from adding high-fidelity simulations). After each optimization run, we calculate the KL divergence between the posterior at the optimum and the initial posterior using 4 high-fidelity outputs. It is seen in Fig. 29 that there is no noticeable increase in the KL divergence between iterations 10 and 11, meaning that the addition of the 11^{th} high-fidelity output to the low-fidelity surrogate correction did not provide additional information to vary the KL divergence value. This shows convergence of the optimization.

We also compare the optimized solution posterior with the posteriors from the low-fidelity surrogate correction with the 20 high-fidelity outputs (input sampled using OSLH) and the 46 high-fidelity outputs.

It is seen that *KLD*(Post. 20 || Post. 11) = 29.06, whereas the *KLD*(Post. 46 || Post. 11) = 0.02, which means that the joint posterior from the optimization using 11 high-fidelity outputs is very close to the joint posterior from the correction using 46 high-fidelity outputs but different from the joint posterior resulting from correction with 20 OSLH high-fidelity outputs. Assuming that calibration with 46 data points is more accurate than calibration with 20 points (unless erroneous or conflicting data is introduced, which is not the case here), using the multi-fidelity simulation optimization yielded much better results with 11 optimally selected input values compared to the 20 input values selected using OSLH.

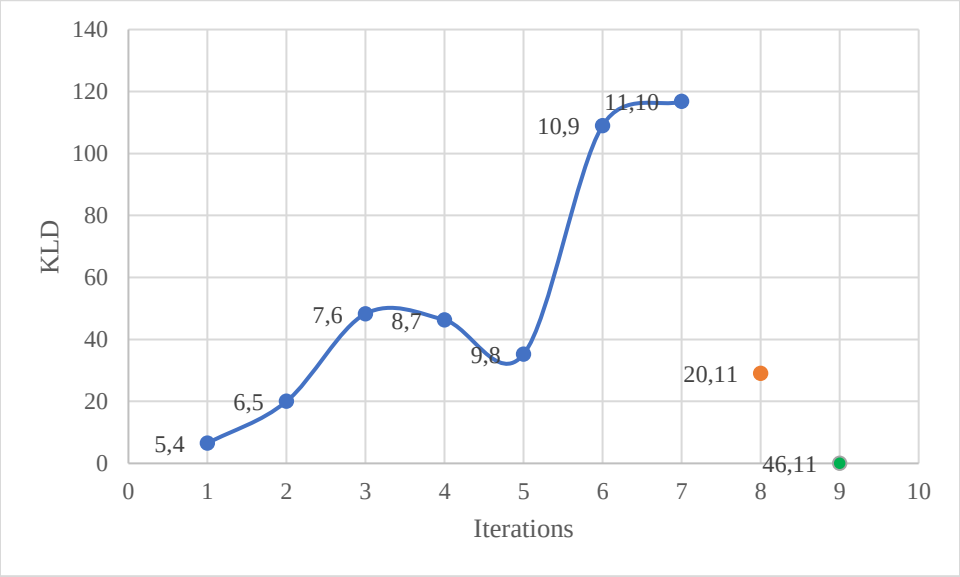

Fig. 29: KL divergence values between subsequent optimization iterations for the joint posteriors of the calibration parameters

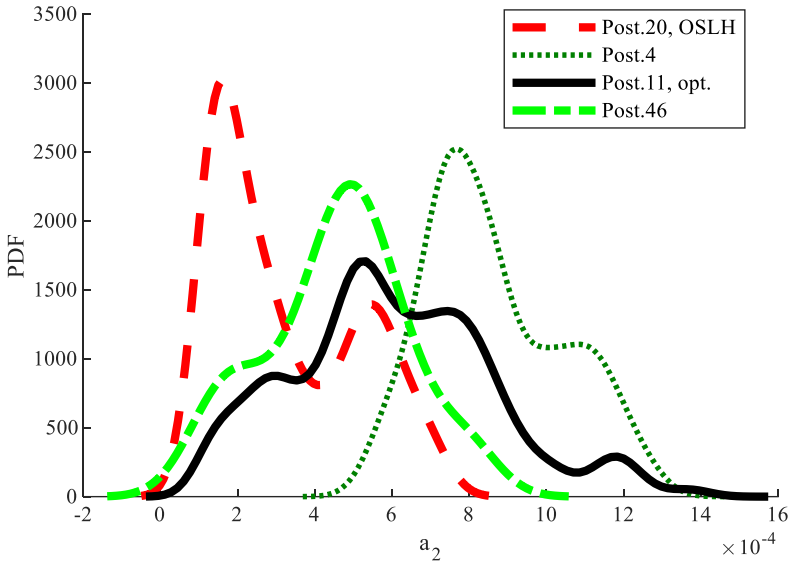

Fig. 30: Marginal posterior distributions for a_2

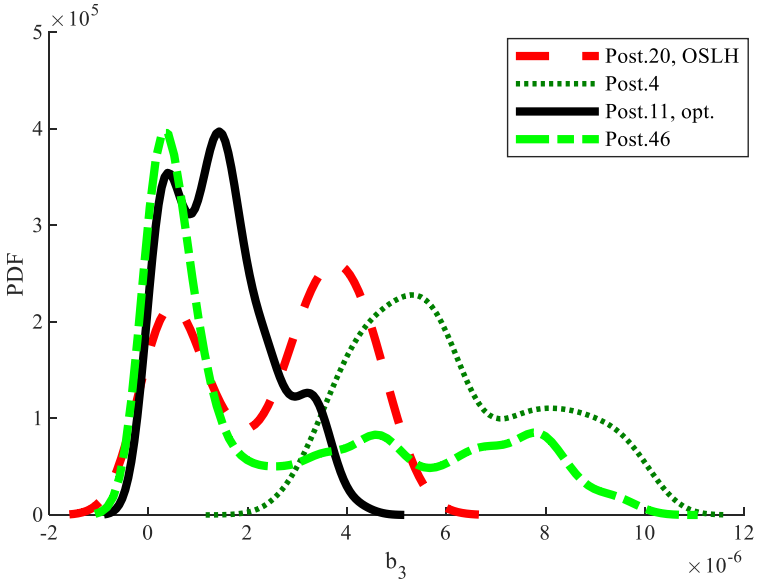

Fig. 31: Marginal posterior distributions for b_2

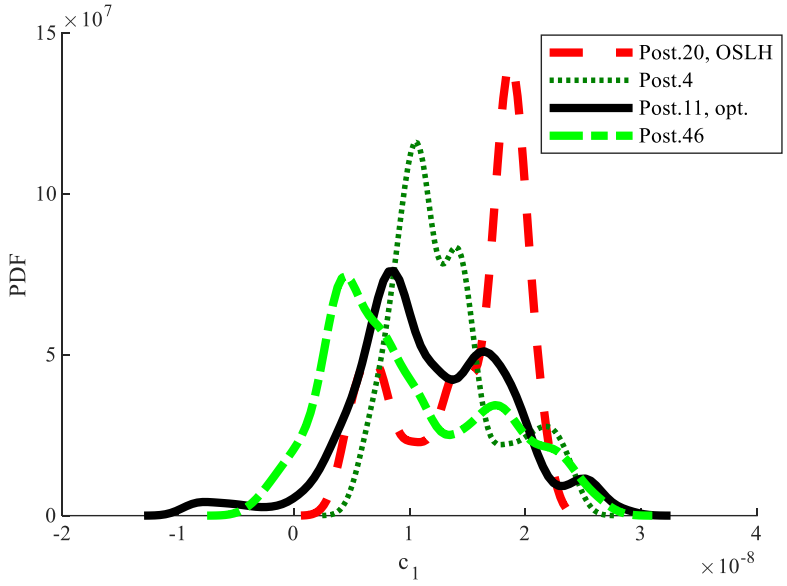

Fig. 32: Marginal posterior distributions for c_1

Figs. 30-32 show the marginal distributions for a_1 (material damping hyperparameter), b_2 (frictional damping hyperparameter) and c_1 (model form error hyperparameter) in the optimization process. The marginals for the remainder of the calibration parameters show a similar trend. We can see that Post.11 converges to the posterior calculated using all the high-fidelity simulations available (46). Although Post.20 used more points than the optimization method, it failed to converge to the benchmark Post.46.

5.3.3 Discussion

This chapter proposes a novel design of experiments method to pick high-fidelity run inputs in aiding the *calibration* of system parameters. As a result, the proposed multi-fidelity simulation optimization is able to converge to better results than a space filling sampling algorithm using almost half of the high-fidelity resources.

From the results, we can see in Fig. 29 that the optimized multi-fidelity simulation with 11 points is better than a calibration with 20 high-fidelity chosen using a space filling OSLH sampling procedure, and equivalent to a calibration of a low-fidelity surrogate model using 46 high-fidelity points. This large improvement is due to the fact that the proposed method is optimized based on the "need" of the model. Optimized high-fidelity points are picked at the locations where the maximum information gain is estimated, which speeds up the calibration process. Noting that an optimization iteration takes less time than a high-fidelity run, the proposed method allows savings in time resources in addition to high-fidelity simulation cost.

5.4 Conclusion

This chapter developed a multi-fidelity simulation optimization method that maximizes the information gain for the calibration of system parameters. We show that in highly non-linear problems such as the structural dynamics curved panel example studied, an optimized sequential method of picking high-fidelity simulation points that maximize information gain in the joint posterior distribution of calibration variables provides faster and more accurate results than a general space-filling algorithm. The proposed method yields better convergence results that are tailored for inference problems specifically.

Chapter 6

Sensor Configuration Optimization

This chapter optimizes the sensor configuration in multi-fidelity dynamics calibration. It uses synthetic observation data to find the best number and locations of sensors to maximize the information gain in the calibration of unknown system parameters.

6.1 Introduction

Calibration exercises are only as good as the collected data. Simulation models cannot be valuable unless the data they are trying to replicate is in itself useful. The success of a calibration exercise depends on the quality of the information extracted from an experimental setup and is directly related to the sensor configuration.

Several different metrics for information gain in experiments have been investigated in the literature. Some studies have used the Fisher information matrix to design calibration experiments and/or optimize the sensor locations. Shah and Udwadia [96] define a method of finding the optimal location for a single sensor in a building structure to calibrate the shear stiffness. Kammer [97] maximizes the trace of the Fisher information matrix to find a sensor configuration set from a larger candidate set that maintains independence of the finite element model target modes partitions. Kirkegaard and Brincker [98] investigate the influence of the increasing number of sensors on the noise-to-signal ratio at the optimal sensor locations. Heredia-Zavoni et al. [99] [100] have focused on minimizing the Bayesian loss function in the trace of the inverse Fisher information matrix to find the optimal sensor location to calibrate lateral stiffness and base flexibility in multiple degrees of freedom shear systems.

In the presence of large data sets, the determinant of the Fisher information influences the information entropy [101]. Studies have used different entropy measures to quantify information gain. Papadimitriou et al. [102] minimize the uncertainty in the model parameter estimates by minimizing the information entropy measure, also known as Shannon's entropy. Papadopoulou et al. [103] use the joint entropy measure to select optimal sensor locations for the purpose of improving predictions of wind flow around buildings. Hu et al. [104] use the relative entropy measure, i.e., the Kullback Leibler divergence, in optimizing experimental input settings in order to maximize information gain for calibration of thermal conductivity and volumetric heat capacity in heated concrete slabs.

Work in structural health monitoring (SHM) has also focused on strain gage location optimization. Abdullah et al. [105] studied the optimization of sensors (or controllers) in discrete locations for control of civil engineering structures. Raich and Liszkai [106] optimize the location and number of sensors to maximize the quality of the information collected in addition to the location of the excitation in a multi-objective optimization approach. Guratzsch and Mahadevan [107] optimize sensor location to detect damage in structures under transient mechanical and thermal loading.

When model parameters are constant and/or deterministic, it has been shown that optimizing the location of one sensor may be enough for calibration [108]. However, when the system parameters and/or the model errors are spatially variant, optimization becomes more challenging, and Nath et al [109] developed an approach for sensor placement optimization to calibrate spatially varying model parameters.

This chapter aims to optimize the number and location of sensors to enhance the multi-fidelity approach to the calibration of unknown model parameters by maximizing the information gain in the

parameters' joint posteriors. We optimize the number and location of sensors in the calibration of unknown system parameters by maximizing the information gain in the parameters' joint posteriors. We consider the effect of the input on both the model parameters and the sensor behavior. The proposed methodology is illustrated for a curved panel subjected to acoustic and non-uniform thermal loading.

6.2 Multi-Fidelity Sensor Location Optimization

The optimized selection of sensor configuration (i.e., number, location and direction of the strain gages) in the experiments is related to step viii of the multi-fidelity calibration algorithm in Section 4.2.3. We consider a grid of candidate sensor locations in the experimental setup and find the optimal number and locations of the sensors to retain the most information in the calibration of the dynamics model parameters. (Note that we are considering strain gage sensors; strain gage readings can be aligned with the *x* or *z* axes of the plane or diagonal. We consider the sensor reading in each direction, even at the same location, as a separate information source). The optimization objective is to select the sensor configuration that maximizes the KL divergence between the joint prior distribution of the calibration quantities and the model errors and their joint posterior distribution.

Since sensor optimization is to be performed before running the actual physical experiments, it has to be done using synthetic observation data. In this paper, the synthetic experimental data $\mathbf{Y}_{obs}^{S}$ is sampled by adding noise to the multi-fidelity model (i.e., a low-fidelity surrogate corrected with high-fidelity simulation outputs at all possible candidate sensor locations).

We start by selecting a small number of sensors among the candidate locations. We then calibrate the system parameters for different location combinations of the sensors and calculate the KL divergence of the posterior distributions with regards to the priors for each location combination. Eq. (31) becomes:

$$\mathbf{Y}^{S}_{\boldsymbol{obs}} + \boldsymbol{\varepsilon}_{\boldsymbol{obs}}(\boldsymbol{X}) = S_1(\boldsymbol{X} + \boldsymbol{\varepsilon}_{\boldsymbol{in}}, \boldsymbol{\lambda}'_{\boldsymbol{\theta i}}) + \boldsymbol{\varepsilon}_{\boldsymbol{surr}} + \boldsymbol{D}'_{\boldsymbol{2,1}}(\boldsymbol{X}) + \boldsymbol{\varepsilon}_{\boldsymbol{d}}(\boldsymbol{X}) \tag{36}$$

where Y^{S}_{obs} is the synthetic observed output at the selected locations, and $S_1(\boldsymbol{X} + \boldsymbol{\varepsilon}_{\boldsymbol{in}}, \boldsymbol{\lambda}'_{\boldsymbol{\theta i}})$ is the corrected low-fidelity surrogate model at the selected locations.

The optimization objective is to select the sensor configuration that maximizes the KL divergence between the joint posterior distribution $\pi(\boldsymbol{\lambda}_{\boldsymbol{\theta i}}, \boldsymbol{\lambda}_{\boldsymbol{D}_{2,1}} | \mathbf{Y}_{\boldsymbol{HF}})$ from step *vi* and the final joint posterior distribution $\pi(\boldsymbol{\lambda}_{\boldsymbol{\theta i}}, \boldsymbol{\lambda}_{\boldsymbol{D}_{2,1}} | \mathbf{Y}_{\boldsymbol{HF}}, \mathbf{Y}_{\boldsymbol{obs}^{\mathrm{s}}})$ from step *viii*.

In formulating the optimization problem, two possibilities can be considered with respect to the test input setting $\boldsymbol{X}$: we can calculate the KL divergence at all test input conditions or calculate the KL divergence for each test input condition separately. Each possibility answers a different question: Does the user want to maximize the information gain considering multiple input settings or at specific input settings? In other words, are the tests to be conducted over multiple input settings or a single input setting?

The optimization formulation for the first case (considering multiple test input settings) can be written as follows:

$$\begin{aligned} &\max_{\boldsymbol{L}} \left[\max_{\boldsymbol{X}} \left(KLD(\pi(\boldsymbol{\lambda}_{\boldsymbol{\theta i}}, \boldsymbol{\lambda}_{\boldsymbol{D}_{2,1}} | \mathbf{Y}_{\boldsymbol{HF}}, \boldsymbol{X}) \,||\, \pi(\boldsymbol{\lambda}_{\boldsymbol{\theta i}}, \boldsymbol{\lambda}_{\boldsymbol{D}_{2,1}} | \mathbf{Y}_{\boldsymbol{HF}}, \boldsymbol{X}, \mathbf{Y}^{S}_{obs})) \right) \right] \\ &s.t.\ L(j) \le L_{\boldsymbol{max}} \\ &\quad L(j) \ge L_{min} \\ &\quad L(j) \ne L(j+1)\ \forall j \in [0, size(\boldsymbol{L})] \end{aligned} \tag{37}$$

where $\boldsymbol{L}$ is the vector of sensor locations, L_{min} and L_{max} are the first and last location of sensors respectively. This means that, at each optimization iteration, we start by calculating the posterior distribution at each input setting, then we compute the KL divergence at each of these input settings.

Finally, we select the maximum KL divergence across all input settings.

In the second case, we assume a single test input setting. In this case, Eq. (37) becomes:

$$\begin{aligned} &\max_L KLD\left(\pi(\boldsymbol{\lambda}_{\theta i}, \boldsymbol{\lambda}_{D_{2,1}} \mid \mathbf{Y}_{HF}, \boldsymbol{X}) \,\|\, \pi(\boldsymbol{\lambda}_{\theta i}, \boldsymbol{\lambda}_{D_{2,1}} \mid \mathbf{Y}_{HF}, \boldsymbol{X}, \mathbf{Y}^{S}{}_{obs})\right) \\ &s.t.\ L(j) \le L_{max} \\ &\quad L(j) \ge L_{min} \\ &\quad L(j) \ne L(j+1)\ \forall j \in [0, size(\boldsymbol{L})] \end{aligned} \tag{38}$$

Since the candidate locations are discrete, we employ simulated annealing [110] to find the optimal solution. Simulated annealing models the physical process of heating a material and then slowly lowering the temperature to decrease defects and minimize the system energy (thus its name). It allows solving bound-constrained optimization problems and is typically used in discrete optimization.

We repeat the optimization framework for an increasing number of sensors and select the optimum sensor configuration for each case. Convergence is reached when adding more sensors does not yield significant improvement in KL divergence values.

6.3 Numerical Example

6.3.1 Problem Description

The example problem is the same as the one used in Chapter 4. The same assumptions on the high and low-fidelity models are used, and the same calibration variables as in Chapter 4 are considered.

Because we are now considering a large candidate set of sensor locations, the model form error is not considered as a linear function of the input as previously assumed. It is modeled as a Gaussian process (GP) following the relationship:

$$\boldsymbol{\varepsilon_d}(P,\Delta T) \sim N(c_1 + c_2 \times P + c_3 \times \Delta T, k_\varepsilon([x,z],[x,z]', \boldsymbol{\varphi}_\varepsilon)) \quad (39)$$

where $c_1 + c_2 \times P + c_3 \times \Delta T$ is the mean function of the GP, *x* and *z* are the directions along the long and short sides of the panel respectively, and $k_\varepsilon = \varphi^{(1)}{}_\varepsilon \exp(-\frac{(x-x')^2}{2(\varphi^{(2)}{}_\varepsilon)^2} - \frac{(z-z')^2}{2(\varphi^{(3)}{}_\varepsilon)^2})\,[111]$ is the GP covariance function between locations [*x*,*z*] and [*x*,*z*]'. When the number of strain gage locations is low (less than three), we have too many parameters and too little data; in that case, we may approximate the model discrepancy by its mean function only (i.e., ignoring the GP term), and simplify Eq. (39) as is done in Chapter 4 to:

$$\boldsymbol{\varepsilon_d}(P,\Delta T) = \boldsymbol{c_1} + \boldsymbol{c_2} \times P + \boldsymbol{c_3} \times \Delta T \quad (40)$$

We also assume that the observed error standard deviation is the same at all sensor locations because of the large number of sensors. It still considers the temperature effect, and Eq. (28)becomes:

$$\sigma_{obs}(\Delta T) = d_1 e^{d_2 \times \Delta T} \quad (41)$$

with d_1 and d_2 single variables instead of being vectors.

The aim is to optimize the number and layout of sensors to maximize information gain in the calibration parameters' posteriors. We consider a candidate set of sensors (that include the pre-determined experimental sensor locations from Section 5.3) shown in Fig. 33 below:

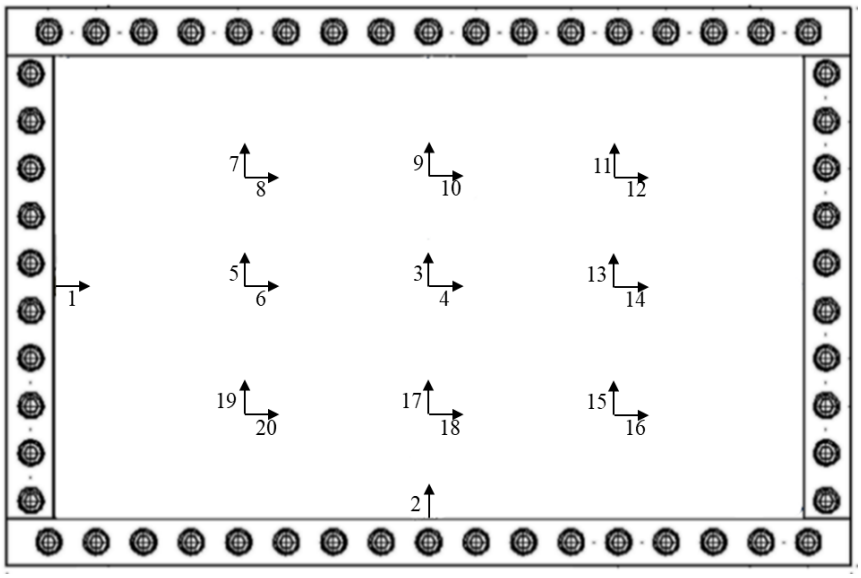

Fig. 33: Candidate set of strain gage locations

6.3.2 Results

The aim in this subsection is to optimize the number and layout of sensors to maximize information gain in the calibration parameters' posteriors. In the following, at each optimization iteration, we select the configuration with the highest KL divergence over the three temperature settings (70 °F, 120 °F and 180 °F as represented by Eq.(37). The optimization was run for a maximum number of iterations of 100.

The first sensor configuration optimization was done for 3 sensors. The optimum was found to be at sensor location [5, 10, 15] in Fig. 33, with a KLD = 164.95. One of the optimization iterations included the configuration [1, 2, 3], which resembles the experimental configuration in Section 5.3 That iteration resulted in a KLD = 89.59. This result shows that a sensor configuration at the optimum location can yield much more information gain that the pre-determined experimental configuration.

The number of sensors was then increased to 5, 7, 8 and 9 sensors. The results are shown in the table below:

Table 7: Sensor optimization results over multiple temperature setting

Number of sensors	***3***	***5***	***7***	***8***	***9***
Optimal point	*[5,10,15]*	*[4,8,11,17,19]*	*[5,9,10,16,17, 18,19]*	*[3,10,11,14,15, 18,19,20]*	*[1,4,6,9,12, 13,15,19,20]*
KLD value	*164.95*	*171.11*	*190.23*	*195.85*	*197.85*

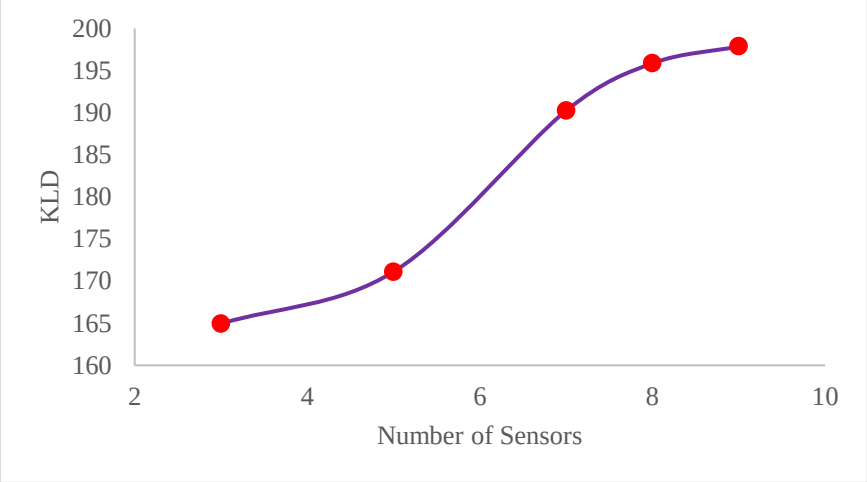

Fig. 34: KL divergence values for different sensor configurations

We notice that the increase in KL divergence does not significantly increase between 8 and 9 sensors. Also, sensor 19 is the most selected by the optimizers (present in all optimal points, except for the 3-sensor case).

In comparison, we ran the optimizer for three sensors at the set temperatures of 70 °F, 120 °F and 180

°F separately as in Eq. (38) This allows the optimizer to select the optimal configuration at each temperature setting, instead of all temperatures combined. The results are shown in Table 8. These results are only useful if the experiment is to be conducted at only one of the three temperature settings.

Table 8: 3-Sensor optimization results at individual temperature settings

Temperature (°F)	***70***	***120***	***180***
Optimal point	*[3,14,19]*	*[4,10,11]*	*[6,8,13]*
KLD value	*129.1*	*159.64*	*167.81*

6.4 Discussion

The proposed approach to optimizing sensor configuration in experiments is very useful in calibration exercises. Instead of relying solely on expert opinions for picking sensor number and location, it allows the incorporation of the physics within the simulation model into the decision-making process. In fact, for the case of three sensors, the optimized location yielded much more information gain in the posterior distributions than the pre-determined sensor configuration in Chapter 4. However, even though the optimization framework proposed saves resources compared to traditional methods of calibration, it is still computationally draining. The optimizer needs to be improved to the point of giving faster convergence allowing more timely decision making.

Note that the multi-variate KL divergence calculation used within the optimization is based on a multi-variate kernel density (KS) density approximation. This estimation relies on the bandwidth value specified by the user. Varying the bandwidth matrix changes the shape of the final density function, and affects the KL divergence value.

In this chapter, the candidate locations of the sensors were discrete and predefined for simplification

purposes. Still, this methodology can be applied in the case of a continuous candidate set by finding the coordinates of the optimum location. The errors are defined as location dependent, and can easily be applied in the case of continuous sensor locations.

6.5 Conclusion

This chapter developed a sensor configuration optimization method that selects the number and location of the sensors to maximize the information gain in the calibration of system parameters. The sensor layout optimization selects the optimal number and locations of the strain gages that maximizes the information gain in calibration while taking into consideration the strain gage uncertainty as an increasing function of the temperature. The proposed method yields convergence results that are tailored specifically for the inverse problem of model calibration.

This work considered a limited number of candidate sensor locations; future work needs to address the computational challenges associated with a large number of possible candidate sensor locations, and also incorporate physical constraints imposed by experimental conditions.

Chapter 7

Conclusion

7.1 Summary of Accomplishments

This dissertation developed a novel optimized method of multi-fidelity information fusion in the Bayesian calibration of unknown system parameters. It used a small number of high-fidelity runs to correct a low fidelity surrogate model, creating stronger physics-informed priors for calibration with experimental data. This method was also optimized to maximize information gain from the high-fidelity model and the experimental data, while minimizing the overall cost. It was applied to a real-world problem of a simplified representation of an aircraft fuselage panel subjected to dynamic acoustic loading and high temperature load, with the goal of calibrating the unknown damping coefficients among other parameters.

Extensive research has been done in using models of different fidelity in prediction, but very few studies looked at the benefits of fusing models of different fidelity in the calibration of unknown system parameters. This work developed efficient and robust approaches of information fusion and information gain in inverse problems.

The multi-fidelity information fusion approach allowed the extraction of information from high-fidelity models into a low-fidelity surrogate model while it avoided building a bad high-fidelity surrogate when high-fidelity simulations are scarce. It was compared to calibrations using surrogates for low and high-fidelity physics models and showed clear advantages in uncertainty reduction in the posterior distributions of the calibration variables.

The proposed approach was extended to calibration of input-dependent system parameters, model parameters and measurement error uncertainty by considering functional relationships between the input and the unknown calibration variables. It accounted for geometric and material nonlinearity effects on the models. The results showed a clear influence of the temperature on the damping-related parameters, as well as the strain gage measurement errors.

The multi-fidelity information fusion approach was then optimized to maximize the information retention in the calibration exercise. The results showed that by judicially picking high-fidelity simulations to maximize the KL divergence between the posterior and prior distributions, calibration is faster and more accurate than by using a general space-filling sampling algorithm. The proposed method produced better convergence results that are tailored for inference problems specifically.

The model calibration is further enhanced by the selection of sensor number and sensor locations to maximize the information gain in the calibration. For an increasing number of sensors, an optimal sensor configuration was selected that maximizes the information gain. The results of the application of the proposed method to the curved panel problem showed promising results, though additional computational resources would be needed to attain a robust convergence.

The contributions optimize both the computational and experimental resources while reducing uncertainty in posterior distributions of unknown calibration quantities. Although illustrated for a structural dynamics problem, the proposed approach is applicable to problems in any discipline where models of multiple fidelity are available.

7.2 Future Work

The proposed method works well for nonlinear problems, and was demonstrated in the case of two

models with an assumed fidelity rank. An approach to assess cost vs. fidelity needs to be developed for cases where comparable models are available (in terms of fidelity and cost) and also in the case where more than two models need to be used.

It would be beneficial if the multi-fidelity information fusion method could also use information regimes of applicability of the different models. Hombal and Mahadevan [112] developed an approach to model selection by considering regimes of applicability, and this information could be used to weight the different models in different regimes.

In the application problem, the low and high-fidelity models shared the same calibration parameters. Applying this methodology where models of different fidelity have different parameters would be interesting. Would this method work, or would the uncertainty be spread from the shared parameters to the model-specific parameters? How do you incorporate additional high-fidelity parameters in the low-fidelity surrogate? DeCarlo et al. [29] addressed this issue with respect to models in multiple disciplines with local and shared parameters; it is worth exploring how such an approach could be adapted to multi-fidelity calibration.

It would also be desirable to perform actual physical experiments at the optimized sensor locations in Chapter 6 to validate the proposed sensor optimization method. Although it was shown that, for three sensors, the optimal sensor configuration yielded a higher KL divergence than the configuration used in the experiments, having additional experimental data would be helpful in validating the proposed method.

Models of different fidelity capture different properties of a system of interest, and the joint data from these models provide more information about the system than when these models are used individually.

Multi-fidelity optimization can currently deal with models that share the same parameters and can improve low-fidelity models to better mimic higher-fidelity simulations. However, can it fuse information coming from independent experiments on the same specimen that, for example, share the same parameters but measure different outputs? Would it be able to incorporate different formats of information in the form of expert opinion, image data, and even text data? The above questions offer fertile opportunities for future research in the use of multi-fidelity modeling in inverse problems.

Bibliography

[1] S. Sankararaman, Y. Ling, S. Mahadevan, Uncertainty quantification and model validation of fatigue crack growth prediction, Engineering Fracture Mechanics, 78 (2011) 1487-1504.
[2] B. Caesar, Updating System Matrices Using Modal Test Data, 5th International Modal Analysis Conference, IMAC, London, England, 1987, pp. 453-459.
[3] S. Adhikari, Damping Models for Structural Vibration, Trinity College, University of Cambridge, Cambridge, England, 2000.
[4] R.W. Clough, J. Penzien, Dynamics of Structures, McGraw Hill, New York City, New York, 1975.
[5] M.C. Kennedy, A. O'Hagan, Bayesian calibration of computer models, Journal of the Royal Statistical Society: Series B (Statistical Methodology), 63 (2001) 425-464.
[6] J. Brynjarsdóttir, A. O'Hagan, Learning about physical parameters: the importance of model discrepancy, Inverse Problems, 30 (2014) 114007.
[7] E. Simoen, G. De Roeck, G. Lombaert, Dealing with uncertainty in model updating for damage assessment: A review, Mechanical Systems and Signal Processing, 56–57 (2015) 123-149.
[8] J.-A. Goulet, I.F.C. Smith, Structural identification with systematic errors and unknown uncertainty dependencies, Computers & Structures, 128 (2013) 251-258.
[9] J. McFarland, S. Mahadevan, Multivariate significance testing and model calibration under uncertainty, Computer Methods in Applied Mechanics and Engineering, 197 (2008) 2467-2479.
[10] M. Ns, A.W. Rosenbluth, M.N. Rosenbluth, A.H. Teller, E. J. Teller, Equation of State Calculations by Fast Computing Machines, 1953.
[11] W.K. Hastings, Monte Carlo sampling methods using Markov chains and their applications, Biometrika, 57 (1970) 97-109.
[12] G. Casella, E.I. George, Explaining the Gibbs Sampler, The American Statistician, 46 (1992) 167-174.
[13] R.M. Neal, Slice sampling, (2003) 705-767.
[14] Z. Zhang, C. Jiang, X. Han, D. Hu, S. Yu, A response surface approach for structural reliability analysis using evidence theory, Advances in Engineering Software, 69 (2014) 37-45.
[15] J.E. Hurtado, D.A. Alvarez, Neural-network-based reliability analysis: a comparative study, Computer Methods in Applied Mechanics and Engineering, 191 (2001) 113-132.

[16] C.M. Rocco, J.A. Moreno, Fast Monte Carlo reliability evaluation using support vector machine, Reliability Engineering & System Safety, 76 (2002) 237-243.
[17] R.G. Ghanem, P. Spanos, Stochastic Finite Elements: A Spectral Approach, Springer, Berlin, Germany, 1991.
[18] V.J. Romero, L.P. Swiler, A.A. Giunta, Construction of response surfaces based on progressive-lattice-sampling experimental designs with application to uncertainty propagation, Structural Safety, 26 (2004) 201-219.
[19] S.S. Isukapalli, Uncertainty Analysis of Transport-Transformation, Rutgers, the State University of New Jersey, New Brunswick, New Jersey, 1999.
[20] S. Huang, S. Mahadevan, R. Rebba, Collocation-based stochastic finite element analysis for random field problems, Probabilistic Engineering Mechanics, 22 (2007) 194-205.
[21] G.A.F. Seber, C.J. Wild, Nonlinear Regression, John Wiley & Sons, Inc., New York City, New York, 1989.
[22] J.E. Mottershead, M.I. Friswell, Model Updating In Structural Dynamics: A Survey, Journal of Sound and Vibration, 167 (1993) 347-375.
[23] S. Mahadevan, B. Liang, Error and Uncertainty Quantification and Sensitivity Analysis in Mechanics Computational Models, 1 (2011) 147-161.
[24] K. Christodoulou, C. Papadimitriou, Structural identification based on optimally weighted modal residuals, Mechanical Systems and Signal Processing, 21 (2007) 4-23.
[25] E.L. Zhang, P. Feissel, J. Antoni, A comprehensive Bayesian approach for model updating and quantification of modeling errors, Probabilistic Engineering Mechanics, 26 (2011) 550-560.
[26] E. Simoen, C. Papadimitriou, G. Lombaert, On prediction error correlation in Bayesian model updating, Journal of Sound and Vibration, 332 (2013) 4136-4152.
[27] Y. Ling, J. Mullins, S. Mahadevan, Selection of model discrepancy priors in Bayesian calibration, Journal of Computational Physics, 276 (2014) 665-680.
[28] G.B. Arhonditsis, D. Papantou, W. Zhang, G. Perhar, E. Massos, M. Shi, Bayesian calibration of mechanistic aquatic biogeochemical models and benefits for environmental management, Journal of Marine Systems, 73 (2008) 8-30.
[29] E.C. DeCarlo, B.P. Smarslok, S. Mahadevan, Segmented Bayesian Calibration of Multidisciplinary Models, AIAA Journal, 54 (2016) 3727-3741.
[30] S. Sankararaman, Y. Ling, C. Shantz, S. Mahadevan, Inference of equivalent initial flaw size under multiple sources of uncertainty, International Journal of Fatigue, 33 (2011) 75-89.

[31] R.G. Bower, I. Vernon, M. Goldstein, A.J. Benson, C.G. Lacey, C.M. Baugh, S. Cole, C.S. Frenk, The parameter space of galaxy formation, Monthly Notices of the Royal Astronomical Society, 407 (2010) 2017-2045.
[32] S. Kullback, R.A. Leibler, On Information and Sufficiency, Ann. Math. Statist., 22 (1951) 79-86.
[33] J.O. Berger, L.R. Pericchi, The Intrinsic Bayes Factor for Model Selection and Prediction, Journal of the American Statistical Association, 91 (1996) 109-122.
[34] X. Jiang, S. Mahadevan, Bayesian risk-based decision method for model validation under uncertainty, Reliability Engineering & System Safety, 92 (2007) 707-718.
[35] T. Leonard, J.S.J. Hsu, Bayesian Methods: An Analysis for Statisticians and Interdisciplinary Researchers, Cambridge University Press, Cambridge, UK, 1999.
[36] H. Jeffreys, Theory of Probability, Oxford University Press Inc., Oxford, New York, 1961.
[37] R. Rebba, S. Mahadevan, Validation of models with multivariate output, Reliability Engineering & System Safety, 91 (2006) 861-871.
[38] D. Zhou, Benefits of High-Fidelity Dynamic Simulation, ISA Automation Week, Mobile, Alabama, 2011.
[39] G.V. Candler, D.M. Peterson, T.W. Drayna, Detached Eddy Simulation of a Generic Scramjet Inlet and Combustor, 47th AIAA Aerospace Sciences Meeting Including The New Horizons Forum and Aerospace Exposition, Orlando, Florida, 2009.
[40] G.V. Candler, T. W., D. T.W., Design and Optimization of the ASET Inward-Turning Scramjet Inlet, JANNAF 30th Airbreathing Propulsion Subcommittee Meeting, Boston, Massachusetts, 2008.
[41] K. Higgins, S. Schmidt, Simulation of a Sonic Jet Injected into a Supersonic Cross-Flow, 16th Australasian Fluid Mechanics Conference, Gold Coast, Australia, 2007.
[42] M.W. Oppenheimer, T. Skujins, M.A. Bolender, D.B. Doman, A Flexible Hypersonic Vehicle Model Developed with Piston Theory, Atmospheric Flight Mechanics Conference and Exhibit, AIAA Paper No. 2007-6396, Hilton Head, South Carolina, 2007.
[43] M.A. Bolender, D.B. Doman, Nonlinear Longitudinal Dynamical Model of an Air-Breathing Hypersonic Vehicle, Journal of Spacecraft and Rockets, 44 (2007) 374-387.
[44] F.R. Chavez, D.K. Schmidt, Analytical aeropropulsive-aeroelastic hypersonic-vehicle model with dynamic analysis, Journal of Guidance, Control, and Dynamics, 17 (1994) 1308-1319.
[45] M. McEwan, W. J.R., C. J.E., L. Y.T., A Finite Element / Modal Technique for Nonlinear Plate and Stiffened Panel Response Prediction, 42nd

AIAA/ASME/ASCE/AHS/ASC Structures, Structural Dynamics, and Materials Conference ad Exhibit, AIAA-2001-1595, Seattle, Washington, 2001.
[46] M. McEwan, A Combined Modal / Finite Element Technique for the Non-Linear Dynamic Simulation of Aerospace Structures, University of Manchester, England, 2001.
[47] A.A. Muravyov, S.A. Rizzi, Determination of nonlinear stiffness with application to random vibration of geometrically nonlinear structures, Computers & Structures, 81 (2003) 1513-1523.
[48] S.A. Rizzi, A. Przekop, System identification-guided basis selection for reduced-order nonlinear response analysis, Journal of Sound and Vibration, 315 (2008) 467-485.
[49] M. Mignolet, A. Radu, Validation of reduced order modeling for the prediction of the response and fatigue life of panels subjected to thermo-acoustic effects, Structural Dynamics: Recent Advances, 8th International Conference, University of Southampton, UK, 2003.
[50] K. Kim, X.Q. Wang, M.P. Mignolet, Nonlinear Reduced Order Modeling of Functionally Graded Plates, 49th AIAA/ASME/ASCE/AHS/ASC Structures, Structural Dynamics, and Materials Conference, AIAA-2008-1873, Schaumburg, Illinois, 2003.
[51] R. Oliva, Model calibration as a testing strategy for system dynamics models, European Journal of Operational Research, 151 (2003) 552-568.
[52] H. F., D. S., W. A., Discussion of Model Calibration and Validation for Transient Dynamic Simulation, 20th International Modal Analysis Conference, IMAC, Los Angeles, California, 2002, pp. 1362-1369.
[53] R.T. Haftka, Combining global and local approximations, AIAA Journal, 29 (1991) 1523-1525.
[54] M.G. Hutchison, E.R. Unger, W.H. Mason, B. Grossman, R.T. Haftka, Variable-complexity aerodynamic optimization of a high-speed civil transport wing, Journal of Aircraft, 31 (1994) 110-116.
[55] M. Kennedy, A. O'Hagan, Predicting the output from a complex computer code when fast approximations are available, Biometrika, 87 (2000) 1-13.
[56] S. Leary, A. Bhaskar, A. Keane, A Knowledge-Based Approach To Response Surface Modelling in Multifidelity Optimization, Journal of Global Optimization, 26 (2003) 297-319.
[57] A.I.J. Forrester, N.W. Bressloff, A.J. Keane, Optimization using surrogate models and partially converged computational fluid dynamics simulations, 2006.
[58] M. Baruch, I.Y. Bar Itzhack, Optimal weighted orthogonalization of measured modes, AIAA Journal, 17 (1979) 927-928.
[59] A. Berman, E.J. Nagy, Improvement of a Large Analytical Model Using Test Data, AIAA Journal, 21 (1983) 1168-1173.

[60] M. Link, Updating of analytical models-Review of numerical procedures and application aspects, Structural Dynamics Forum SD2000, Los Alamos, New Mexico, 1999.
[61] B.N. Datta, S. Deng, V.O. Sokolov, D.R. Sarkissian, An optimization technique for damped model updating with measured data satisfying quadratic orthogonality constraint, Mechanical Systems and Signal Processing, 23 (2009) 1759-1772.
[62] Z.X. Yuan, K.P. Yu, Finite element model updating of damped structures using vibration test data under base excitation, Journal of Sound and Vibration, 340 (2015) 303-316.
[63] V. Arora, S.P. Singh, T.K. Kundra, Finite element model updating with damping identification, Journal of Sound and Vibration, 324 (2009) 1111-1123.
[64] J.L. Beck, L.S. Katafygiotis, Updating Models and Their Uncertainties. I: Bayesian Statistical Framework, Journal of Engineering Mechanics, 124 (1998) 455-461.
[65] K.-V. Yuen, L.S. Katafygiotis, Bayesian Modal Updating using Complete Input and Incomplete Response Noisy Measurements, Journal of Engineering Mechanics, 128 (2002) 340-350.
[66] K.-V. Yuen, L. Katafygiotis, Bayesian Fast Fourier Transform Approach for Modal Updating Using Ambient Data, Advances in Structural Engineering, 6 (2003) 81-95.
[67] S.-K. Au, Fast Bayesian FFT Method for Ambient Modal Identification with Separated Modes, Journal of Engineering Mechanics, 137 (2011) 214-226.
[68] S.-K. Au, Fast Bayesian ambient modal identification in the frequency domain, Part I: Posterior most probable value, Mechanical Systems and Signal Processing, 26 (2012) 60-75.
[69] A.G. Walshaw, Mechanical Vibration with applications, Ellis Horwood Ltd, New York, 1984.
[70] P.D. Welch, The use of fast Fourier transform for the estimation of power spectra: A method based on time averaging over short, modified periodograms, Audio and Electroacoustics, IEEE Transactions on, 15 (1967) 70-73.
[71] R.E. Kass, L. Wasserman, The Selection of Prior Distributions by Formal Rules, Journal of the American Statistical Association, 91 (1996) 1343-1370.
[72] T.K. Caughey, A. Vijayaraghavan, Free and forced oscillations of a dynamic system with “linear hysteretic damping” (non-linear theory), International Journal of Non-Linear Mechanics, 5 (1970) 533-555.
[73] G. Kerschen, K. Worden, A.F. Vakakis, J.-C. Golinval, Past, present and future of nonlinear system identification in structural dynamics, Mechanical Systems and Signal Processing, 20 (2006) 505-592.

[74] A. Pourhabib, B. Balasundaram, Non-isometric Curve to Surface Matching with Incomplete Data for Functional Calibration, arXiv preprint arXiv:1508.01240, (2015).
[75] M. Plumlee, V.R. Joseph, H. Yang, Calibrating Functional Parameters in the Ion Channel Models of Cardiac Cells, Journal of the American Statistical Association, 111 (2016) 500-509.
[76] D.A. Brown, S. Atamturktur, Nonparametric Functional Calibration of Computer Models, arXiv preprint arXiv:1602.06202, (2016).
[77] C.E. Rasmussen, Gaussian processes for machine learning, (2006).
[78] National Instruments, How Is Temperature Affecting Your Strain Measurement Accuracy?, http://www.ni.com/white-paper/3432/en/, 2016.
[79] C. Li, S. Mahadevan, An efficient modularized sample-based method to estimate the first-order Sobol′ index, Reliability Engineering & System Safety, 153 (2016) 110-121.
[80] J.-S. Park, Optimal Latin-hypercube designs for computer experiments, Journal of Statistical Planning and Inference, 39 (1994) 95-111.
[81] G.E.P. Box, N.R. Draper, Empirical model-building and response surfaces, John Wiley & Sons, Oxford, England, 1987.
[82] M.D. McKay, R.J. Beckman, W.J. Conover, A Comparison of Three Methods for Selecting Values of Input Variables in the Analysis of Output from a Computer Code, Technometrics, 42 (2000) 55-61.
[83] J.H. Halton, On the efficiency of certain quasi-random sequences of points in evaluating multi-dimensional integrals., Numerische Mathematik, 2 (1960) 84-90.
[84] J.M. Hammersley, Monte Carlo Methods for Solving Multi-variable Problems, Annals of the New York Academy of Sciences, 86 (1960) 844-874.
[85] I.M. Sobol, On the distribution of points in a cube and the approximate evaluation of integrals, USSR Computational Mathematics and Mathematical Physics, 7 (1967) 86-112.
[86] R.H. Myers, D.C. Montgomery, Response Surface Methodology: Process and Product in Optimization Using Designed Experiments, John Wiley \& Sons, Inc., 1995.
[87] D.J.C. MacKay, Information-Based Objective Functions for Active Data Selection, Neural Computation, 4 (1992) 590-604.
[88] S. Tong, Active learning: Theory and applications, Stanford University, 2001.
[89] B.J. Bichon, M.S. Eldred, L.P. Swiler, S. Mahadevan, J.M. McFarland, Efficient Global Reliability Analysis for Nonlinear Implicit Performance Functions, AIAA Journal, 46 (2008) 2459-2468.

[90] V. Hombal, S. Mahadevan, Bias Minimization in Gaussian Process Surrogate Modeling for Uncertainty Quantification, 1 (2011) 321-349.
[91] J. Goh, Prediction and Calibration using Outputs from Multiple Computer Simulations, Department of Statistics and Actuarial Science, Simon Frasier University, 2014.
[92] L. Le Gratiet, J. Garnier, Recursive Co-Kriging Model for Design of Computer Experiments with Multiple Levels of Fidelity, 4 (2014) 365-386.
[93] V. Balabanov, R. Haftka, B. Grossman, W. Mason, L. T. Watson, Multifidelity Response Surface Model For HSCT Wing Bending Material Weight, 1998.
[94] T.M. MATLAB and Statistics Toolbox Release 2018a, Inc., Natick, Massachusetts, United States.
[95] R.H. Byrd, J.C. Gilbert, J. Nocedal, A trust region method based on interior point techniques for nonlinear programming, Mathematical Programming, 89 (2000) 149-185.
[96] P.C. Shah, Udwadia, F., Methodology for Optimum Sensor Locations for Parameter Identification in Dynamic Systems, Journal of Engineering Mechanics, 120 (2) (1994).
[97] D.C. Kammer, Sensor placement for on-orbit modal identification and correlation of large space structures, Journal of Guidance, Control, and Dynamics, 14 (1991) 251-259.
[98] P.H. Kirkegaard, R. Brincker, On the optimal location of sensors for parametric identification of linear structural systems, Mechanical Systems and Signal Processing, 8 (1994) 639-647.
[99] E. Heredia-Zavoni, L. Esteva, Optimal instrumentation of uncertain structural systems subject to earthquake ground motions, Earthquake Engineering & Structural Dynamics, 27 (1998) 343-362.
[100] E. Heredia-Zavoni, R. Montes-Iturrizaga, L. Esteva, Optimal instrumentation of structures on flexible base for system identification, Earthquake Engineering & Structural Dynamics, 28 (1999) 1471-1482.
[101] C. Papadimitriou, Pareto optimal sensor locations for structural identification, Computer Methods in Applied Mechanics and Engineering, 194 (2005) 1655-1673.
[102] C. Papadimitriou, J.L. Beck, S.-K. Au, Entropy-Based Optimal Sensor Location for Structural Model Updating, Journal of Vibration and Control, 6 (2000) 781-800.
[103] M. Papadopoulou, B. Raphael, I. Smith, C. Sekhar, Hierarchical Sensor Placement Using Joint Entropy and the Effect of Modeling Error, Entropy, 16 (2014) 5078.
[104] Z. Hu, D. Ao, S. Mahadevan, Calibration experimental design considering field response and model uncertainty, Computer Methods in Applied Mechanics and Engineering, 318 (2017) 92-119.

[105] M.M. Abdullah, A. Richardson, J. Hanif, Placement of sensors/actuators on civil structures using genetic algorithms, Earthquake Engineering & Structural Dynamics, 30 (2001) 1167-1184.
[106] A.M. Raich, T.R. Liszkai, Multi-objective Optimization of Sensor and Excitation Layouts for Frequency Response Function-Based Structural Damage Identification, Computer-Aided Civil and Infrastructure Engineering, 27 (2012) 95-117.
[107] R.F. Guratzsch, S. Mahadevan, Structural Health Monitoring Sensor Placement Optimization Under Uncertainty, AIAA Journal, 48 (2010) 1281-1289.
[108] X. Huan, Y. Marzouk, Gradient-Based Stochastic Optimization Methods in Bayesian Experimental Design, 4 (2014) 479-510.
[109] P. Nath, Z. Hu, S. Mahadevan, Sensor placement for calibration of spatially varying model parameters, Journal of Computational Physics, 343 (2017) 150-169.
[110] S. Kirkpatrick, C.D. Gelatt, M.P. Vecchi, Optimization by Simulated Annealing, Science, 220 (1983) 671-680.
[111] C.E. Rasmussen, Gaussian processes for machine learning, 2006.
[112] V.K. Hombal, S. Mahadevan, Model Selection Among Physics-Based Models, Journal of Mechanical Design, 135 (2013) 021003-021003-021015.